POLITECNICO DI MILANO
FACOLTA' DI INGEGNERIA INDUSTRIALE
CORSO DI LAUREA IN INGEGNERIA SPAZIALE

Design and Characterization of Shape Memory Alloys for Optomechanical Mounting

Academic Year 2010/2011

Advisor : Prof. Luca Di Landro
Tutor : Dott.ssa Elena Villa
Tutor : Ing. Marco Riva

Rigamonti Daniela matr. 712287
Zanetti Francesco matr. 712288

Table of Contents

Sommario

Il settore in cui si inserisce questa attività di tesi è l'ambito specificatamente aerospaziale del montaggio di ottiche con materiali innovativi. In particolare si sono valutate le prospettive e le possibilità offerte dai materiali SMA, che notoriamente presentano caratteristiche uniche nel campo dei materiali metallici in quanto a proprietà funzionali, elastiche e di smorzamento.

L'attività si è sviluppata con una prima fase preparatoria di caratterizzazione attraverso test sperimentali di diversi campioni in lega NiTi, strettamente legata all'ottenimento dei parametri caratteristici di questi materiali, necessari alla modellazione numerica degli stessi. In questa fase si è cercato anche di capire la sensitività del modello numerico rispetto alla variazione di tali parametri e alle prove sperimentali usate per ottenerli. Infine si è verificato la validità del modello nel rappresentare materiali metallici così particolari.

Il passo successivo è stato la progettazione numerica, seguita dalla realizzazione pratica, di un dimostratore per il segmento di applicazione a terra, che è costituito da un semplice sistema di montaggio, nel quale il NiTi verrà utilizzato per quattro lamine di supporto dell'ottica. Lo scopo di questa progetto è poter aver un primo riscontro effettivo del percorso di sviluppo, scelta e lavorazione dei supporti in NiTi e per verificare le prestazioni del sistema globale rispetto a quelle di un materiale di confronto quale l'acciaio.

Abstract

The subject of this work is related to aerospace applications and in particular is focused on the employment of innovative material for optical support systems. In this particular case the use of Shape Memory Alloys (SMAs) is investigated in order to evaluate perspectives and possibilities offered by this class of metals, extremely interesting as functional materials for their elastic and damping properties.

The activity is developed in two main phases: the first related to the study of materials properties and the second focused on the development of a small prototype.

During the first phase, some NiTi alloy samples was characterized using different experimental techniques. This preliminary study was focused on obtaining the specific values for materials parameters, necessary to create and verify numerical models simulating the materials behavior. At this step the sensitivity of the computational model to the variation of the parameters for the materials was investigated. The comparison of the results to experimental data was used to evaluate the capability of numerical models to reproduce the behavior of such class of materials.

The second phase of this project was related to the practical realization of a small device, thought for ground-based applications, made up of four small NiTi flexures used as a support for an optical component. The device was designed and modeled in order to be able to evaluate the effects of the use of different materials. The results of modeling was compared to the data obtained from the prototype device. The aim of this work is to obtain a first evaluation on the properties, development and employment of NiTi-based supports for optomechanical applications and to verify the performances of a complete system as a respect to an analogous system made up using traditional materials like steels.

Keywords

Shape Memory Alloys, Lagoudas numerical model, Optomechanical Mounting, Aerospace applications.

1 Shape Memory Alloys (SMAs)

1.1 Why using SMAs

The expression *Shape Memory* refers to the ability of certain materials to "remember" a shape, even after severe deformations. A large deformation induced in the SMAs can recover perfectly by two possible paths: the first is that deformed at a certain temperature these materials retain the deformed shape, then spontaneously return to their original, pre-deformation appearance when heated (*shape memory effect*, SME), the second is that deformed at constant temperature, recovery is achieved by simply removing the load (*pseudoelasticity* or *superelasticity*, PE). The discriminating factor between the two behaviors is the interaction stress-temperature concept which will be extended in the following paragraphs.

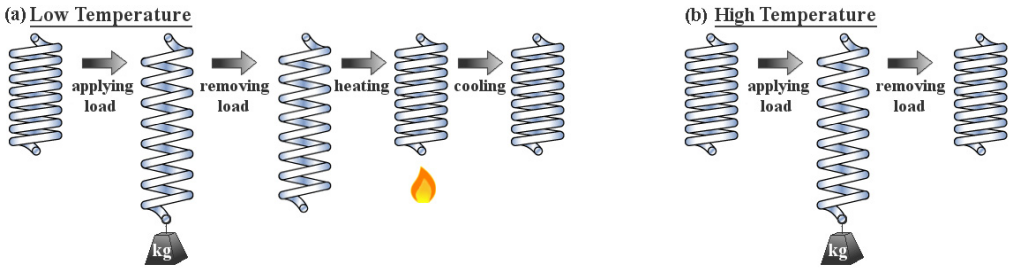

Figure 1.1 - Shape Memory Effect (a) and Pseudo Elasticity Effect (b)

The basis of the special properties of SMAs is their particular reversible crystallographic transformation, called *thermoelastic martensitic transformation*. Its detailed description can be very complex and is beyond the scope of this thesis, though one cannot obtain an understanding of the engineering aspects of SMAs without becoming familiar with the basic principles of thermoelastic martensite and its transformation.

Therefore this chapter describes the microscopic and macroscopic fundamental aspects of SMAs, i.e. the crystal structures, the crystallography of martensitic transformations, the origin of shape memory mechanism and so on.

1.2 Microscopic behavior

1.2.1 Crystal lattice structures

The martensitic transformation act between two solid phases: a parent phase called *austenite* and a product phase called *martensite*.

The austenite is the stable state at high temperature and has a body-centered cubic crystal structure (usually B2 for Ni-Ti alloys; some other alloys has BCC or DO3) with high body-centered symmetry to which correspond a high elastic modulus.

The martensite is the stable state at low temperature and has for the NiTi system a monoclinic distorted structure (denoted by B19') of the crystal lattice to which corresponds a lower elastic modulus. Since the crystal structure of martensite has a lower symmetry, can coexist several orientations called variants; the martensitic variants are twenty-four and in a state without load are all present.

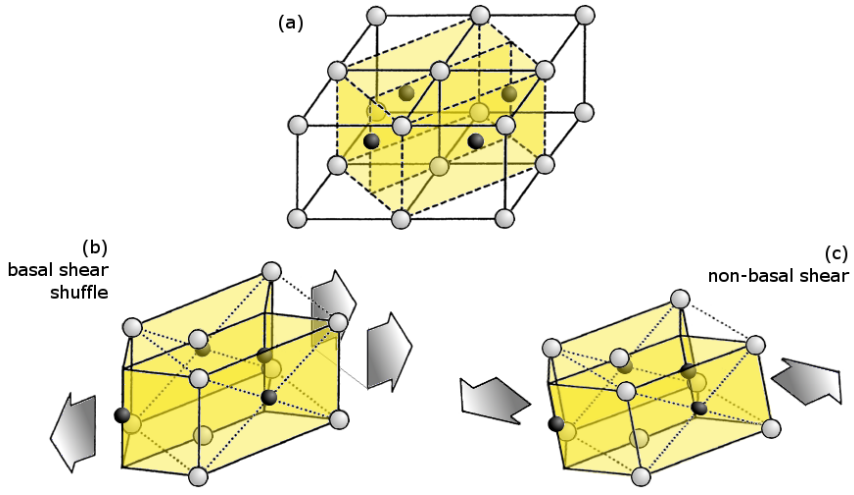

Figure 1.2 - Structures of (a) the parent phase B2, (b) orthorhombic phase B19, and (c) the product monoclinic martensite phase B19'

Figure 1.2 shows the two different structures: the parent phase structure B2 (a) and the product phase structure B19' (c). Considering a face centered tetragonal cell within the B2 structure (FCT, defined by dashed lines in Figure 1.2a) and applying a sliding, it

forms orthorhombic B19 structure (Figure 1.2b). If additional transverse shear is applied to B19, this orthorhombic structure deforms into monoclinic B19' structure (Figure 1.2c). For the NiTi system, the structure does not pass by the intermediate step and transforms from B2 to B19' directly.

Under some conditions or heat treatment, may also appear a third phase called R-phase, characterized by a rhombohedral crystal structure of type R, which is a rhombohedral distortion of the lattice B2 of austenite. It is therefore a further phase that precedes the martensite during transformation.

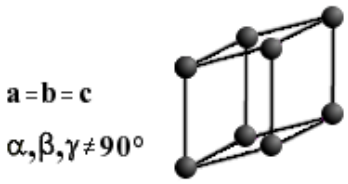

Figure 1.3 - Primitive crystal lattice of rhombohedral phase

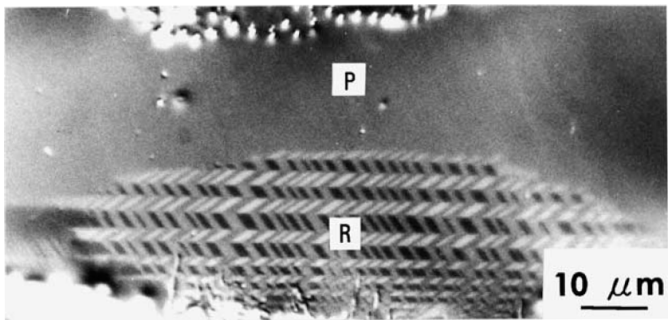

Figure 1.4 - Optical micrograph of the transformation from B2 (P-phase) to R in a NiTi system

1.2.2 Mechanism of transformation

Crystallographically, the transformation from austenite to martensite is often thought in two parts: the *Bain strain* and the *lattice-invariant shear*.

The Bain strain consists of all the atomic movements needed to produce the new structure. In order to illustrate this process can be useful a qualitative two-dimensional approach shown in Figure 1.5.

Note that as the interface between the two phases advances, each atom is required to move by only a very small amount. The new martensitic structure results of all these small coordinated movements without any atomic diffusion.

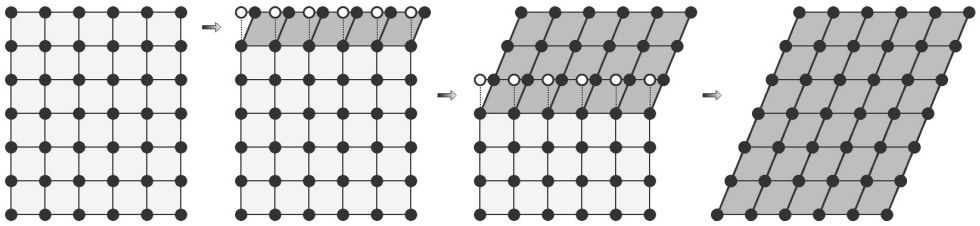

Figure 1.5 - Two dimensional scheme of Bain Strain movement

The second part of a martensitic transformation, the lattice invariant shear, is an accommodation step: the martensitic structure produced by the previous step is of a different shape than the surrounding austenite and therefore must be somehow adapted to the surrounding structure that is not yet transformed. There are two general mechanisms by which this can happen: slip and twinning. In both cases each individual cell has the new martensitic structure, but the overall shape is that of the original austenite. Slip is a permanent process, while twinning is a reversible one. Then, for shape memory to occur, is required that twinning is the dominant accommodation process.

Figure 1.6 - The two mechanism of accommodation: (a) slip, (b) twinning

The two dimensional model can be useful again to show how, in a state without external load the similar variants are coupled in a configuration called twinned, in which the boundary between the twin variants is a mirror plane. The twin boundaries are of a very low energy and quite mobile, so, if a stress is applied to the structure, the twin boundaries will easily move, producing a shape which better accommodates the applied stress. The condensation of many twin variants into a single favored one is called *detwinning*.

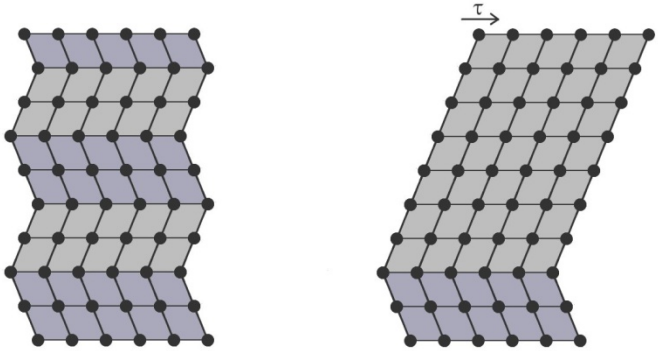

Figure 1.7 - Detwinning process

The inverse transformation is possible because the crystals tend to reorient themselves to the original configuration trying to reach the lower total energy state, thanks to a property called *crystallographic reversibility*.

1.2.3 Characteristics of transformation

Solid-Solid
Is a transformation between two solid phases, changing the internal arrangement of the material, hence its physical properties.

First Order
Martensitic transformations are first order, meaning that the heat is liberated when martensite is formed, there is a hysteresis associated with the transformation and there is a temperature range over which austenite and martensite coexist.

Diffusionless (or Displacive)
Transformations do not requires long range atomic migration: atoms are cooperatively rearranged into a new, more stable crystal structure, but without changing the chemical nature of the matrix. Because of this the transformation generally progress in a time-independent manner, with the motion of the interface between the two phases being limited only by the speed of sound (i.e. instantaneous for our purpose).

Athermal
At transformation concluded, the amount of the new phase present is usually dependent only upon temperature, and not upon how long is the isothermal time.

Reversible
Due to the twinning-detwinning process, which does not break the atomic bonds into the crystals, but only re-orient them, the martensitic transformation is reversible.

1.3 Macroscopic behavior

1.3.1 Gibbs Free Energy

The driving force of the martensitic transformation is the energetic gap to overcome for the transition from parent phase to product phase.

Like for all phase transformations, martensitic transformation and its reverse are thermodynamically possible if they result in an overall reduction of the Gibbs Free Energy of the system. Plotting the progress of Gibbs Free Energy of austenite (G^A) and martensite (G^M) versus temperature, it results in two subtended curves represented in Figure 1.8.

The phase which shows a lower Gibbs Energy at a given temperature is the thermodynamic more stable phase, then the one to which the system will tend spontaneously.

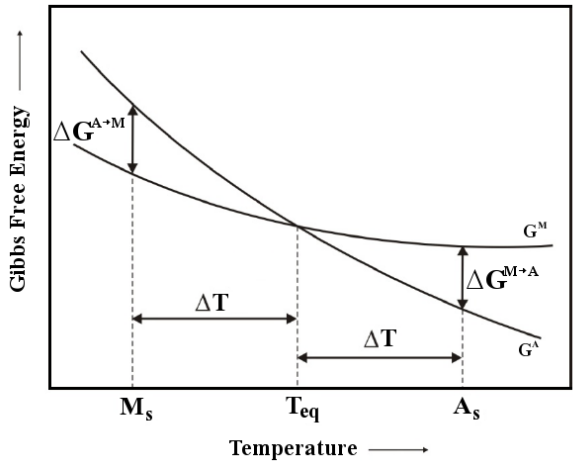

Figure 1.8 - Curves of Gibbs Free Energy versus Temperature for austenite and martensite phases

$$G = H - TS \quad (where: H = enthalpy, S = entropy, T = temperature)$$

At the intersection, martensite and austenite are in a thermodynamic equilibrium.

Decreasing the temperature, the transition from austenite to martensite would start, though the formation of a martensite nucleus in the parent phase creates interfacial and elastic internal energies, therefore the temperature should be further reduced. Thus the transformation does not occur at T_{eq} but at a certain undercooling ΔT, which allows to identify the *martensitic transformation start* $M_s = T_{eq} - \Delta T$, and requires a specific amount of energy $\Delta G^{A \to M}$, that is therefore the critical driving force, composed of the chemical Gibbs energy G_C and the strain energy E_e. The dual effect goes for the reverse transformation, which occurs not with a nucleation of parent phase (as is instead for the steel martensite), but by a shrinking of martensite. It occurs at a superheating ΔT, that defines the *austenitic transformation start* $A_s = T_{eq} + \Delta T$ and the driving force $\Delta G^{M \to A}$.

Because of this gap between the beginning temperatures of the transformations, the martensitic transformation shows a thermal hysteresis. The undercooling and superheating necessary to overcome the chemical driving force varies for different alloys and even compositions.

In addition to the start temperatures, the finish temperatures of the transformations are also to define. Together they are one set of the macroscopic variables that characterize the behavior of SMA.

To obtain the equilibrium temperature, the following equation can be used:

$$T_{eq} = \frac{(A_S + A_F)/2 + (M_S + M_F)/2}{2}$$

1.3.2 Relation between Stress and Temperature

From the above, it is clear that temperature and stress are macroscopic variables that can both drive the transformation and have to be considered together, here is why the definition *thermoelastic* martensite. Normally, on cooling under no stress, the martensite forms at M_S. But in the same material, martensite can form above M_S if a stress is applied, and the martensite so-formed is termed stress-induced martensite (SIM). The driving force for the transformation is now mechanical, as opposed to thermal.

Above M_S, the stress required to produce SIM increases with increasing temperature, as shown in Figure 1.9.

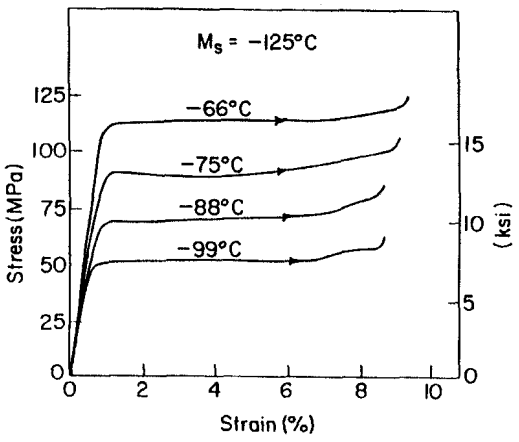

Figure 1.9 - Stress-strain curves for a Cu-Zn single crystal loaded in tension above Ms.

The variation in the stress to induce martensite as a function of temperature is linear and obeys the Clausius-Clapeyron equation, usually written as:

$$\frac{dP}{dT} = \frac{\Delta H}{T\Delta V}$$

where P is the pressure, T is the temperature, ΔH is the transformation latent heat and ΔV is the transformation volume change. This equation has been traditionally used by chemists, but metallurgists, on the other hand, use the Clausius-Clapeyron equation in the form:

$$\frac{d\sigma}{dM_S} = \frac{\Delta H}{T\varepsilon_0}$$

where ΔH and T have the same meanings as before, and σ, M_S, and ε_0 are, respectively, the applied stress, the shifted M_S temperature and the transformational strain resolved along the direction of the applied stress.

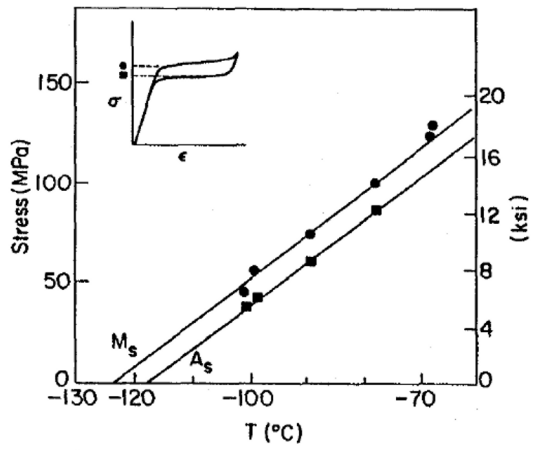

Figure 1.10 - Plotting plateau stresses, as a function of temperature gives a linear plot which obeys the Clausius-Clapeyron relationship

The increase in difficulty to stress induce martensite continues to increase with temperature until M_D, above which the critical stress for inducing martensite is greater than that needed to move dislocations and hence the parent phase undergoes ordinary plastic deformation. This makes M_D the highest temperature at which it is possible to induce martensite. Thus the temperature range for SIM Is from M_S to M_D.

The Clausius-Clapeyron equation works equally well for the non-isothermal case: in the above scenario, temperature was held constant while the stress needed to form martensite was measured, but one can equally well apply a constant load and measure M_S. If one goes through such an exercise one finds that the same Clausius-Clapeyron relation is valid, and the two slopes ($d\sigma/dM_S$) are equal.

Moreover, all the transformation temperatures are affected by stress in the same way, thus generalizing the parameter $d\sigma/dT$ as a fundamental descriptor of shape memory alloys called *stress rate*.

This also allow to define an *experimentally derived phase diagram* (Figure 1.11), in which are evident four main regions (in gray) where the material is stable in a proper phase, while the white regions identify the phase transition.

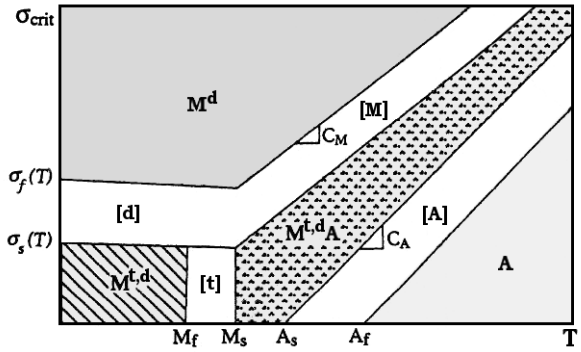

Figure 1.11 - Phase Diagram of transformations depending on stress and temperature

1.3.3 Macroscopic mechanical effects

Having discussed the martensitic transformation, we shall now proceed to study its macroscopic mechanical effects, going into the details of the effects: *Shape Memory, Pseudo-Elasticity* and *Damping*.

Shape Memory Effect

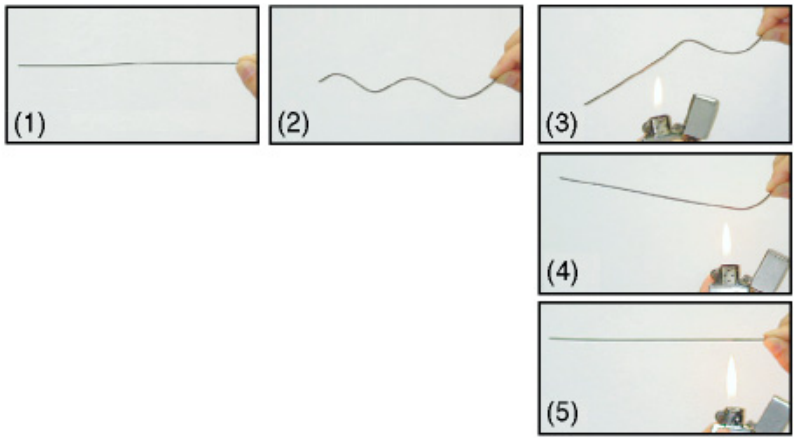

Figure 1.12 - A series of photographs showing the shape-memory effect

The Shape Memory Effect is clearly shown in the photographs in Figure 1.12 for a NiTi wire. Suppose that the wire is martensitic at ambient temperature. Therefore the wire in the martensitic state (1), whose shape is the same as in the parent phase (5), is deformed at constant temperature (2). However, it will revert to its original shape by means of the reverse transformation, if it is heated to a temperature above A_F (3-5).

The mechanism of this fascinating phenomenon is explained with the solid line path in Figure 1.13 in a simplified manner. When the parent phase (austenite) is cooled below M_F, martensite variants are formed side by side (martensite^t) as a result of self-accommodation described earlier. If an external stress is applied, deformation develops by twin boundary movement (martensite^d). If no further action is taken, the deformation is maintained. Only if the sample is heated to a temperature above *A*f, the martensite variants rearranged under stress revert to their original orientation in the parent phase.

The mechanical behavior followed during the process is displayed with σ–ε–T progress at the extreme rear of Figure 1.14 (below M_F). Initially the sample passes through an elastic range, than undergoes a pseudo-plastic transformation, corresponding to the phase of detwinning, where the slope of the curve is reduced. After the applied load is removed, remains a residual strain. It recovers heating the specimen between A_S and A_F at zero stress, as seen in the ε-T plane.

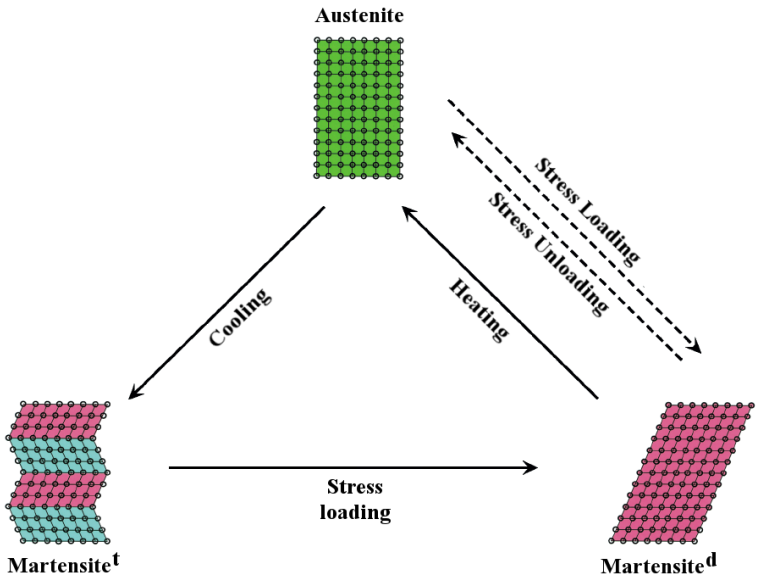

Figure 1.13 - Schematic illustration of shape-memory (solid lines) and superelasticity (dotted lines)

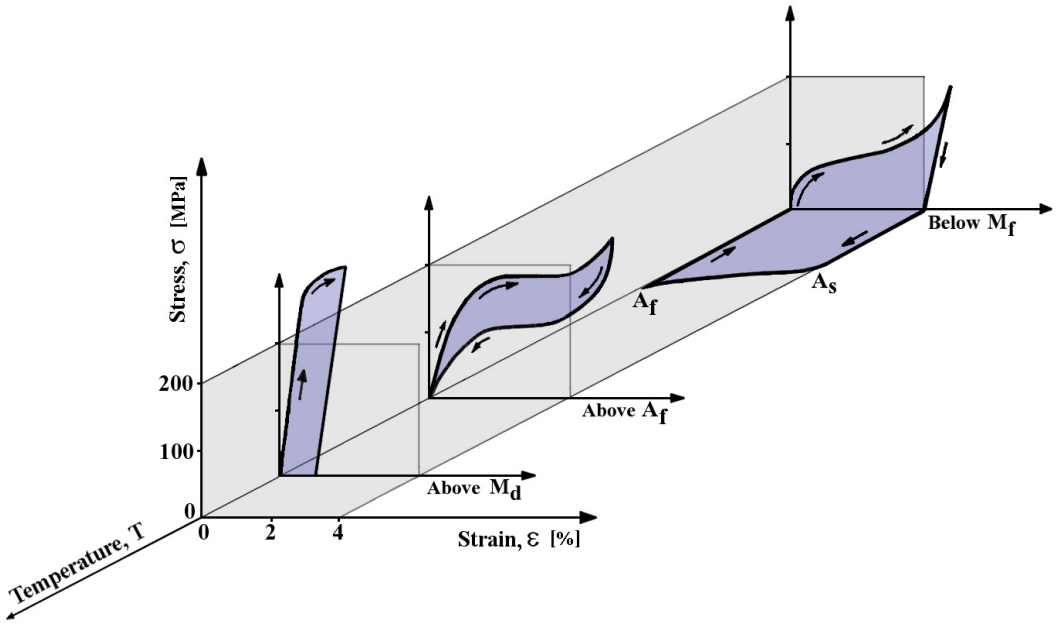

Figure 1.14 - Three dimensional Stress-Strain-Temperature diagram, showing the behavior of a Ti-Ni alloy deformed below MF, above AF, and above MD

In the SME described, only the shape of the parent phase is "remembered" by the alloy. This is sometimes called the *one-way SME*. If the sample is subjected to a training treatment, being cyclically heated in a restrained condition, it is possible for the alloy to remember both its parent shape and martensite shape simultaneously. This is called the *two-way SME,* although the strength to recover the martensite shape is weaker. The origin of this effect essentially derives from the character of the martensitic transformation. Thus, if lattice defects or precipitates are introduced by

thermo-mechanical heat treatment, only specific martensite variants are formed in the martensitic transformation, thus giving a peculiar shape to the sample also in cooling phase.

Pseudoelasticity

Now, let us see what happens if the sample is stressed at a temperature above A_F (dotted line path in Figure 1.13). As already mentioned, it is possible to induce the martensitic transformation even above M_S if we apply stress. However, the martensite is completely unstable in absence of stress at a temperature above A_F, thus the reverse transformation simply occurs during unloading in this case, and the strain completely recovers in the thermoelastic transformation.

The mechanical behavior followed during the process is displayed with σ–ε progress at the center of Figure 1.14 (above A_F). Here again the first range is the elastic one. Note that the martensitic structure can deform by moving twin boundaries, which are quite mobile, thus the yield strength of the martensite is extremely low compared to that of the austenite, which must deform only by elastic deformation of the crystal structure. After the elastic field SIM is formed, leading to the usual pseudoelastic loop with an upper and lower plateau, related to thermal hysteresis and showing an increasing strain at constant stress, related to thermal hysteresis. The upper plateau corresponds to the formation of martensite under stress, while the lower one represents the reversion of the SIM when the stress is released.

Finally, in the front σ–ε plane of Figure 1.14 (above M_D) is represented the situation at a still higher temperature. In this case no SIM is formed. Instead, the parent phase undergoes ordinary plastic deformation.

Damping

It is also well known that NiTi alloys can exhibit high mechanical damping.

For high-damping metals, the major mechanisms are the stress-induced movement of dislocations or planar defects. It is well known that there are abundant twin boundaries both in the martensite and rhombohedral phases of NiTi alloys and that these twin boundaries can be easily moved by the external stress to accommodate the strain. Than can be postulated that the high damping capacity of NiTi alloys is closely related to the well-known phenomenon of twin boundaries reorientation.

In the transformation regions there is also a good amount of the damping capacity which are attributed to two contributions. One arises from the plastic strain and twin-interface movement during the thermal transformation. The other originates from the stress-induced transformation formed by the applied external stress.

No twin boundaries exist in the austenite phase of NiTi alloys, and the dislocation density in the matrix is quite low. Hence, the damping capacity is suggested simply to come from the dynamic hysteresis of pseudoelastic loop and is therefore related to large strain: the area enclosed by the hysteresis loop is proportional to the energy absorbed and thus to the damping capacity during this type of transformation. Because

this dynamic hysteresis loop generally dissipates a smaller quantity of energy, the damping capacity in the B2 phase of NiTi alloys is smaller if little strain levels are maintained.

1.4 Aerospace Applications of SMAs

Perhaps two of the most well-known fixed-wing projects of the past are the *Smart Wing* program and the *Smart Aircraft and Marine Propulsion System Demonstration* (SAMPSON).

The Smart Wing program was intended to develop and demonstrate the use of active materials, including SMAs, to optimize performance of lifting bodies. Here, SMA wire tendons were used to actuate hingeless ailerons while an SMA torque tube was used to initiate spanwise wing twisting of a scaled-down F-18.

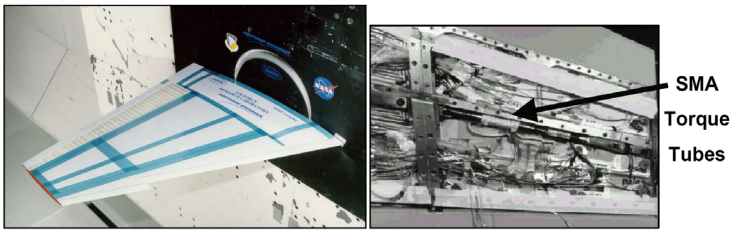

Figure 1.15 - Total and cut-away view of the SMA torque tube as installed in the model wing during Phase I of the SMART Wing project

The SAMPSON program was designed to demonstrate the usefulness of active materials in tailoring the inlet geometry and orientation of various propulsion systems. Here the SMAs employing the shape memory effect were used to rotate the inlet cowl in order to change its cross-sectional area. Two opposing SMA bundles were used to actuate in two directions, with an alternate heating.

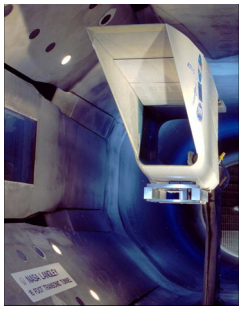

Figure 1.16 - The SAMPSON F-15 inlet cowl as installed in the NASA Langley Transonic Wind Tunnel

Portions of the SAMPSON project also studied the use of SMA "cables" wrapped circumferentially around the aft portion of the fan cowling of a jet engine in order to increase or decrease fan nozzle area in different regions of the flight regime.

Another research was concentrated into a similar principle utilizing bending actuation of SMAs instead of cables. In this case the goal is to optimize the trade-off between

noise mitigation at takeoff/landing and performance at altitude. Such engine noise levels are often highly regulated by various civil agencies. Often, flow mixing devices known as “chevrons” are statically installed along the trailing edges of the exhaust nozzles. Here the composite chevrons were designed to be reconfigurable with SMA beam components embedded inside. The SMA elements are formed such that they force the chevron inward and mix the flow of gases (reducing noise) at low altitudes and low speeds where the engine temperature is high. They then relax and straighten at high altitude and high speeds, increasing engine performance. These chevron research efforts demonstrate the capability of SMAs to be fabricated in the form required and then to be completely embedded within a structure, providing truly integrated actuation. Figure 1.17 illustrates the current Boeing design for the variable geometry chevron.

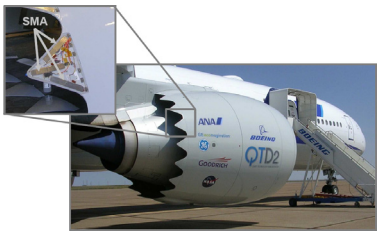

Figure 1.17 - Boeing variable geometry chevron, flight testing
(composite layer has been removed from the chevron for exposition of the active SMA elements)

In addition to propulsion system applications, shape memory effect actuation is also commonly applied to the problem of adaptable lifting bodies, including the morphing of the wing structure.

Space applications are those which seek to address the unique problems of release, actuation and vibration mitigation during either the launch of a spacecraft or its subsequent operation in a micro-gravity and zero-atmosphere environment.

Perhaps the most prolific use of shape memory alloys in space is in solving the problem of low-shock release. It has been estimated that, up to 1984, 14% of space missions experienced some type of shock failures, half of these causing the mission to be aborted. Pyrotechnic release mechanisms were often found to be the root cause. Because they can be actuated slowly by gradual heating, SMA components are suited for use in low-shock release mechanisms. Investigation into this unique problem has led to devices which are currently available, including the popular Qwknut or the Micro Sep-Nut. In both of these devices, the simple shape memory effect is used.

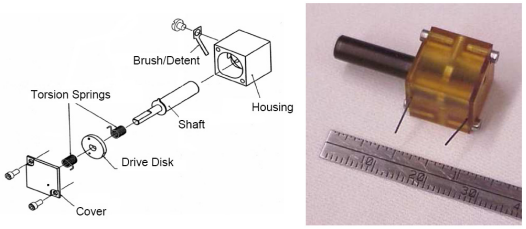

Figure 1.18 - The Rotary Latch as design and tested at the Applied Physics Laboratory

The active component is deformed and detwinned before installation. In orbit, the element is then heated, shape is recovered, and release occurs. Repeated use mechanisms such as the Rotary Latch have also been introduced, and this example can been seen in Figure 1.18.

Another SMA application is the of various spacecraft components via SME. One early example includes an SMA-actuated solar collector utilizing torsional elements which can modify its shape to optimize performance. For a similar purpose, the Lightweight Flexible Solar Array (LFSA) was developed: it incorporated a thin SMA strip at the hinge location which, when heated and actuated, opened a previously folded solar array. An illustration of this design is shown in Figure 1.19.

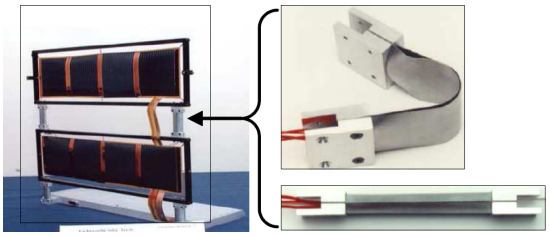

Figure 1.19 - LFSA and detail of hinges, folded and deployed configurations

Another example of morphing application is the Shape Memory Alloy Thermal Tailoring Experiment (SMATTE). It is a proof-of-concept experiment showing that a panel could be deformed from one stable shape to another via actuation of an SMA foil attached to only one surface of the panel. Such a design could be used to tailor the shape of spacecraft antennae.

A different and well-known SMA space actuation application of SMAs is the Mars Pathfinder mission in 1997. The mission included an SMA actuator which served to rotate a dust cover from a specific region of a solar cell so that the power output of this protected and clean region could be compared to the power output of non-protected regions, thereby quantifying the negative effects of dust settling on the solar panels

SMAs have also been used as sensors. In the case of sensing, SMAs are used to acquire information from a thermomechanical system. This is possible due to the material property changes which occur during the phase transformation induced during heating or loading.

Finally, the large hysteresis and strong nonlinearity exhibited during the pseudoelastic effect make shape memory alloys suitable for use as vibration dampers and isolators. Such properties may prove to be useful in mitigating the high vibration loads placed on payloads during launch. Research is also being performed which takes into account the tunable nature of SMA vibration isolators.

2 Mounting Optics

2.1 Brief Historical Overview

Astronomy is probably the oldest natural science. Since the dawn of humanity the sky was source of admiration and curiosity. Animated from the wish of knowledge, men were stimulated to astronomical studies for religious reasons and necessities of life: a rude esteem of time, day and night, and succession of season.

Figure 2.1 - The first Telescope was built by HancLippershey in 1609 and the following year Galileo Galilei perfected his design

All astronomical data have been collected by simply looking at the sky, at first using only own view and understanding of some celestial mechanism, contributed to the creation of calendars important for agriculture and the survival of man. Until the 16th century astronomy was confused with astrology, and only with the advent of the scientific method has come to a clear separation between these two disciplines. The modern astronomy was born with Copernicus and it has evolved to the present day.

The invention of telescope has been a milestone of astronomy research, already from the first rudimentary forms it allowed man to have more precise observations, revolutionizing some ancient belief sand making great steps forward in science. The technical development and launch of space exploration allows furthering expanding the scope of investigation and knowledge of the cosmos. The telescope is a device that, together with discoveries in the fields of optical and physical, has undergone a long evolutionary process and, over the centuries, the transformation of this instrument has made a significant contribution to the development of astronomy. The telescope becomes the eye for astronomers which allows them to capture multiple types of data and try to better understand the universe.

The goodness of the telescope depends on many different factors such as the choice of the lenses, and all the mechanisms for proper placement and maintenance of the instrument: optomechanics.

2.2 Optomechanics

Optomechanics could be defined as the science, engineering, and/or art of maintaining the proper shapes and positions of the functional elements of an optical system so that the system performance requirements are satisfied. The importance of proper optomechanic design can be understood with follow example: the eyeglasses that many of us wear. The frame must hold the lenses such that their principal points and astigmatic correction are in the right position and orientation with respect to the user's eyes to within appropriate tolerances. The frame must also interface to the user’s head in a comfortable and reliable way, and the whole system must perform and survive in an appropriate variety of environments. The optical design of an optical instrument is often less than half of the design work. The mechanical design of the elements and their support and positioning also are at least as critical. If we look at the typical astronomical telescope consisting of two or three mirrors, there are many more parts in the mechanical structure that position the mirrors and attempt to do so without distorting the functional surfaces. It can be seen that the mechanical design or the optomechanics plays a major role in any optical instrument development, particularly where the optics and mechanics interface. It can be seen from the above example of eyeglasses that optomechanics is significant to our lives over the whole range from the mundane to the scientific world. An out-of-tolerance condition in our glasses can cause us headaches and other pains. Similar conditions in space telescope cause errors in the data collected and the scientific conclusions. On the other hand, proper eyeglasses enhance our individual abilities and comfort, and a proper space telescope can expand our knowledge of the universe.

2.3 Environment and material

The effective engineering design of optical instruments requires knowledge of the adverse environments under which the product is expected to operate and the selection of materials is vital for maximizing environmental resistance and ensuring the proper operation. The most important conditions to be considerate are temperature, pressure, vibration and shock. In fact these influences exert static and dynamic force that may cause deflection and dimensional changes, as misalignment, buildup of internal stress or even breakage of components. Other critical conditions include humidity, corrosion, abrasion, and erosion, radiation which can affect performance or lead to progressive deterioration of the instrument.

Temperature

The thermal gradients are due to distortions and misalignments of optical surfaces caused by differential expansion of components. Furthermore, any rate of temperature acting on optical assembly must be such as not to produce thermal shock and damage and, at worst, breaking of the optical.

Pressure

The decrease in ambient pressure may lead to the extraction of air or other gases from various sectors, such as space between the lenses, between the support mechanisms, etc. Pressure differences may be such as to distort the optical and mechanical surfaces.

In the space depressurization is an inevitable consequence and cause outgassing or desaturation even in materials, especially at high temperatures. Some materials also absorb water from moist environments on Earth and release it into the void. The gases emitted from these materials can be harmful to the coatings or may be deposited on optical surfaces.

Vibration and shock

The forces cause the entire instrument or portion of it to be displaced from their equilibrium positions, properly designed system will be able to respond to perturbations in order to return to the equilibrium condition, under the action of restoring force that may include internal elastic forces, or gravitational forces. It is important to recognize that changes in dimension can occur in an optical component, these changes may be temporary under low loading or permanent under high loading the exceeds the breaking point for brittle materials or elastic limits of mechanical materials.

Environment	Normal	Severe	Extreme
Low Temperature	293 K	222 K	2.4 K
High Temperature	300 K	344 K	373 K
Low Pressure	88 kPa	57 kPa	0 kPa
Vibration	0.2 mm/s	0.04 g^2/Hz	0.13 g^2/Hz
	RMS f > 8Hz	20<f<100 Hz	30<f<1500 Hz

Table 2.1 - Summary of environment limits

The materials typically used for the mechanical components of optical instruments, such as instrument housing, lens barrels, cells, spacers, retainers, and prism and mirror mounts, are metals. Composites may be used in some structural applications.

- **Aluminum** alloys have different properties, low, medium or high strength, good dimensional stability and machinability. It is easily welded and brazed, but CTE match to glasses and most crystal is not close.
- **Beryllium** is light in weight with high stiffness, resists corrosion and radiation effects, and is fairly stable dimensionally. It is expensive to purchase and to process, so it is used primary in optical instruments intended for sophisticated applications(cryogenic temperatures)
- **Invar** is used for high performance instruments for space and cryogenic applications to take advantage of its mighty low CTE.
- **Stainless steels** are used in optical mounts primary for their strength and their fairy close CTE match to some glasses, but a weight penalty must be paid to achieve these advantages.
- **Titanium** is the material of choice in many high performance system where a close CTE match to glass and it has high yield strength but is somewhat expensive to machine.
- **Carbon** fibers have higher ultimate tensile strength and lower Young's moduli, i.e. less stiff than other materials. They are lightweight and have different CTE for axial and transverse directions. The axial CTE is close to the glass value, while the transverse CTE is close to metal values.

Other materials for the optical system are optical glasses, plastics crystals, and mirror substrate materials.

- **Optical glasses** are available from manufacturers worldwide in several hundred varieties depending on the required optical and mechanical performance.
- **Optical plastics** are softer than glasses and are hard to polish to a precise surface figure. Their CTEs are larger than those of glasses. The advantage of using plastic components is their low density and ease of manufacture in large quantities.
- **Optical crystals** are used in optics when transmission in the infrared or ultraviolet spectral regions is required.
- **Mirrors** consist of a reflecting surface attached to or integrate with a supporting structure.

2.4 Optomechanical mounting

The main purpose of the mount is to ensure that the position and orientation of the various components is maintained properly. It must be able to constrain the various elements in order to respect tolerances for decentering, tilt, roll and axial spacing, induced stresses and surface deformations. The ideal mount should be kinematic so all six degrees of freedom are independently constrained without redundancy. In a true kinematic interface the forces are applied at infinitesimal areas and no moments are transferred to the optic, but in such case the stress can be large. Semi-kinematics mount

has the same six constraints but each of these acts over a small area to distribute the force and reduce the stress.

A kinematics interface can be obtained with design of accurate system that is able to concentrate reaction force of mount on optical surface, for example applying spherical bearings. Semi-kinematics support is usually used where there is an optical relatively rigid, such as when to have that the smallest dimensions at least one fifth of the largest one, and if the stress may be too high. A rigid body with more than six constraints is called overconstrained and it is nonkinematics, in this case there may be concentration of stress.

2.5 Positioning

An optical system generally consists of an optical surface (lens or mirror) placed in a metal cell. This cell is metallic glass support, which used to fix the lens closely with support. The mounting cell interfaces must be toleranced to be compatible with the glass tolerances. Rotational symmetry of most optical system apertures leads to corresponding symmetry in most lenses and window mounts and in many mirror mounts and this usually simplifies the design of the mechanical housings.

The radial positioning is obtained from the contact between the lens rim and the cylindrical inside diameter of the mount: rim contact. Constraint can also come from the radial components of axial force, as a preload, exerted against curved lens surfaces; radial preload produced by such means as radially directed clamps, or setscrews; radial force imposed by induced mechanical interferences or differential contraction of lens and mountings material as a result of temperature changes. Axial constraint is provided by clamping the lens near its rim between a mounting feature such as shoulder or spacer and some retaining means.

If the interface in the mount are not well located, the lens can be decentered or tilted, with respect the overall optical system axis, also the decentering of the optical axis of the lens with respect to the outside diameter of the lens is an error, due to the optical shop.

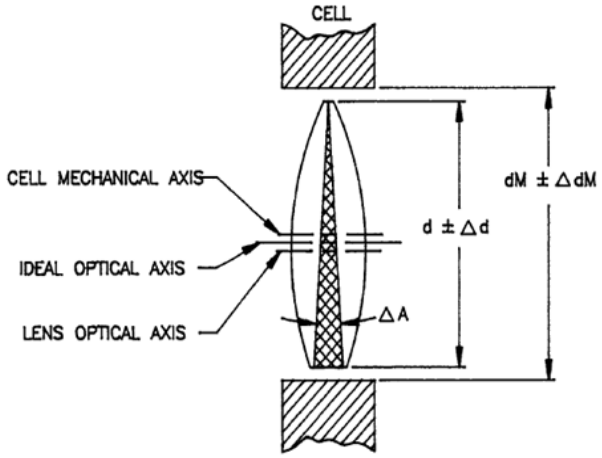

Figure 2.2 - Decentering factors of a lens in a cell

The centering of the mounting bore with respect to the ideal axis is what the machine shop works on. There needs to be some fit clearance, f, for the assembler to insert the lens into the cell.

An ideal lens might be tilted with respect to the system's ideal optical axis because the metal locating surface of the cell is tilted by an angle ΔAT, as shown in figure. This may be an error on support or a request.

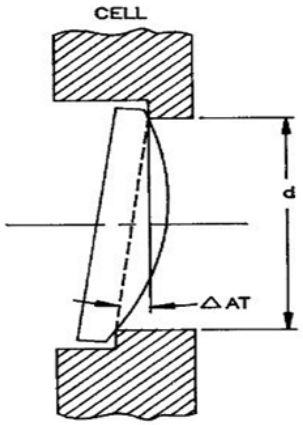

Figure 2.3 - Tilt factors of a lens

Tilt movements enable the user to tilt the plane of sharpest focus so that it no longer lies perpendicular to the lens axis. Usually the image plane (containing the film or image sensor) the lens plane, and the plane of focus are parallel, and are perpendicular to the lens axis; objects in sharp focus are all at the same distance from the camera. When the lens plane is tilted relative to the image plane, the plane of focus (PoF) is at an angle to the image plane, and objects at different distances from the camera can all be sharply focused if they lie in the same plane.

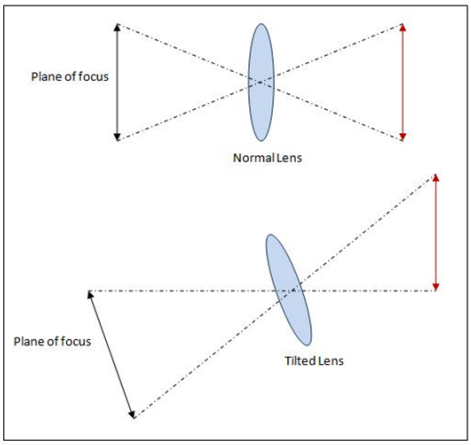

Figure 2.4 - Tilt effect

The ideal lens might also roll an oversized bore as shown in follow figure. This shows that the left-hand surface tilts while the right-hand surface is correctly located against the perfect cell. The lens will roll about the center of curvature of the right-hand surface R2.

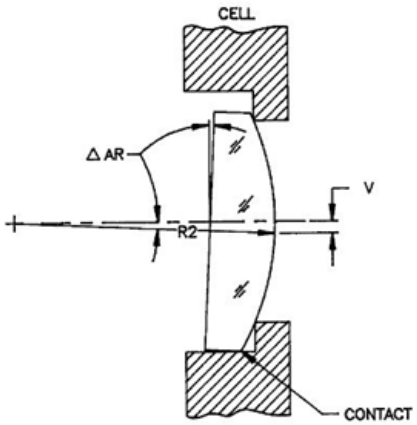

Figure 2.5 - Roll factors in a lens

Axial force applied to a lens mounted in this manner will introduce nonsymmetrical stresses. If the lens is constrained by large axial force and also touches the internal diameter of the mount, warpage of the lens and asymmetrical stress concentrations will occur. It clears the important to define accurate tolerance to avoid stress concentration and optic errors.

In the following table typical tolerance values have been reported.

Parameters	Units	Tolerance		Limit Precision Value
		Large	Low	
De-centering	[mm]	0.1	0.010	0.005
Tilt	[arcmin]	3	0.3	0.1
Mean error angle	[arcmin]	5	0.5	0.1

Table 2.2 - Tolerance mounting values

2.6 Mounting Forces

Preloads applied to the surfaces of optical components compress the optic and produce corresponding elastic stresses within the material; force concentrated on small surface areas cause localized high stresses (force on area).They can lead to excessive distortion of malleable materials such as plastics or some crystals, or breakage of brittle materials such as glass or crystal. Also reaction forces work on the mount, which can distort the mount temporarily ,permanently or in the worst case ,cause the failure of the system.

In addition to the strictly mechanical problem, applied forces, and stresses, introduce physical optical problems. They may cause birefringence (inhomogeneity of the

refractive index) into normally isotropic optical materials: this affects the propagation speeds of the perpendicular and parallel components of polarized light passing through the material. Even low levels of applied force can cause optical surfaces to deform, especially if the forces are not applied symmetrically. Minute surface deformations, of the order of fractions of a wavelength of light, affect system performance.

2.7 Mounting Individual Lenses

There are several techniques for mounting optical components such as individual and multiple lenses, windows, domes, filters, small mirrors, and prisms. Principles of opto-mechanical design and material selection intended to minimize the adverse effects of imposed forces while retaining component function, location, and alignment as has been explained.

Below different method of assembly among the most widespread, have been submitted to underline the characteristics and difficulties of interface design. Particularly the following sections will be referred to mountings of single lenses or mirrors, because this condition will be the last step of this thesis work.

2.7.1 Spring Suspension

In applications involving large temperature changes with loose centration, tilt, and/or axial positioning tolerances, lenses might be supported by springs.

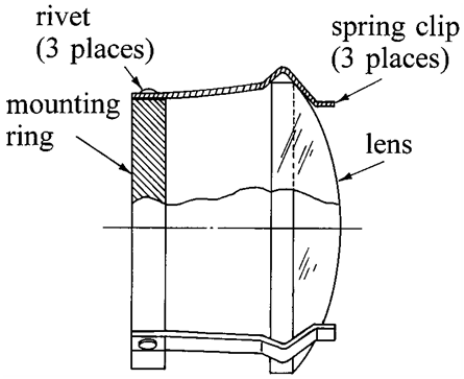

Figure 2.6 - Spring Suspension

Three flat springs spaced at 120°C intervals around the lens rim are shaped to interface with that rim. Symmetry of the cantilevered springs tends to keep the lens centered. Free circulation of air around the lens is allowed. This type of mount also offers some protection against shock and vibration.

2.7.2 Snap Ring

A discontinuous ring that drops into a groove machined into the inside surface of a cell is commonly termed a snap ring. This ring, which acts as a spring, usually has a circular cross section as shown in follow figure. Rectangular cross-section rings are less frequently used. The opening or slot in the ring allows it to be compressed slightly

while sliding into alignment with the groove. The groove cross section is usually rectangular. Ensuring contact between the lens surface and the ring using this technique is difficult since thickness, diameter, and surface radius of the lens as well as ring dimensions, groove location, dimensions, and temperature changes all affect the degree of mechanical interference, if any, existing between the lens and ring. For this reason, this technique is used only where the location and orientation of the lens is not critical. If the cell is designed without a groove, a snap ring can be inserted against the lens and constraint offered by friction between the ring and cell wall. A rectangular ring is preferred in this case.

Disassembly is possible. This design is sensitive to shock and vibration.

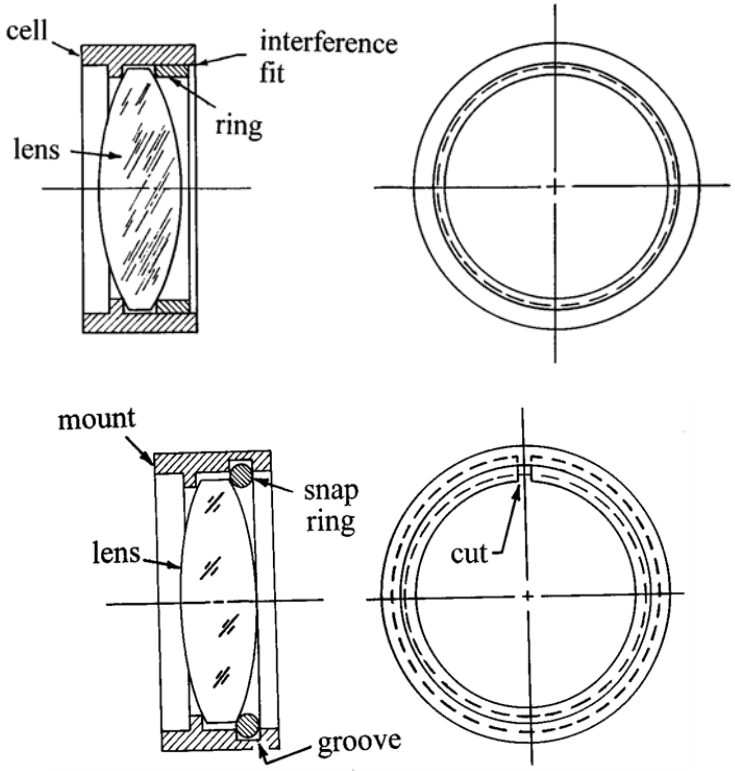

Figure 2.7 - Snap ring

2.7.3 Retaining Ring Mounts

Among the most frequently used technique for mounting lenses is to clamp the lens near its rim between shoulder flange. Axial preload induces axial stress into the lens and cell as discussed in the previous chapter. Manufacturing variations in axial dimensions of lenses and cells can be compensated with this type of mounting and the decentering can be corrected.

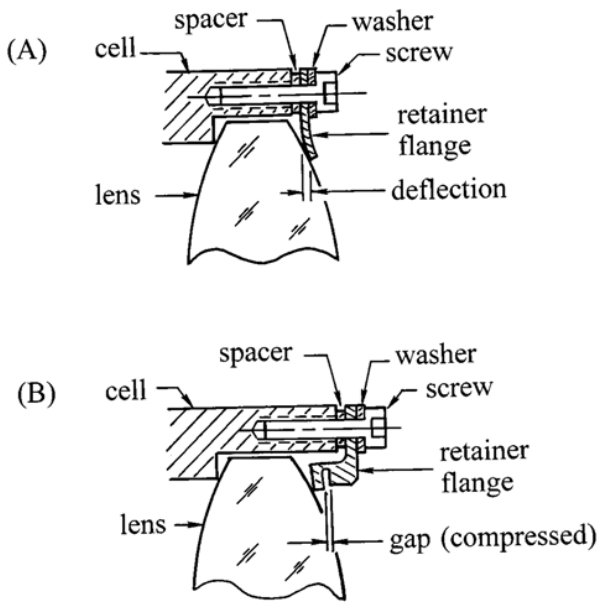

Figure 2.8 - Clamping lens

2.7.4 Threated Ring

Follow figure illustrates a typical threaded retaining ring mount design for a biconvex lens. Contact between the lens and the mechanical parts occurs on the polished glass surfaces as recommended for precise centering of the optical axis to the mechanical axis of the cell and to minimize the need for precise edging or close tolerances on diameter of the lens. To minimize bending of the lens, contact should occur approximately at the same height from the axis on both sides of the lens. Since the spherical surface (either convex or concave) is more or less tilted with respect to the axis at the contact region due to its curvature, an axial preload applied at any point around the lens rim develops force component directed toward the axis that tends to center the lens. When the lens is centered, these radial components balance each other and tend to hold the lens in the aligned condition.

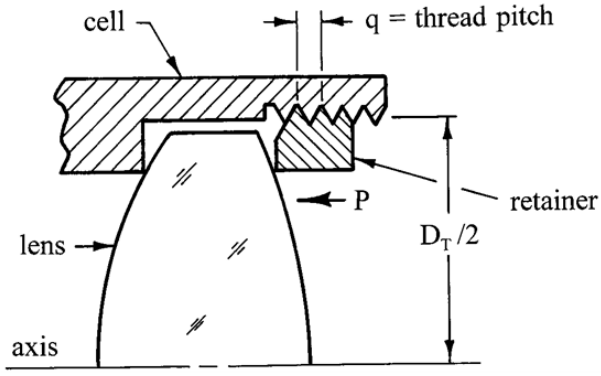

Figure 2.9 - Typical configuration of a lens held in place by axial preload, P, from a threaded retaining ring

3 Numerical Modeling of SMAs

3.1 Constitutive law implementation: Lagoudas model

The fundamental concepts of SMA behavior were introduced in first chapter where the nonlinear behavior and the close link between efforts and temperature have been explained.

Smart structure design is strongly dependent on the availability of useful numerical tools for the performance prediction of the whole system. Therefore, the target is to be able to develop a method by which SMAs behavior might be accurately predicted. The main difficulty is the modeling of the temperature-stress dependence and a non-linear behavior of those alloy. It is necessary to adopt constitutive laws able to be embedded in commercial Finite Element codes and to predict the SMAs response. Among the various existing approaches the Lagoudas model has been adopted and is presented below.

Constitutive equations are mathematical model that to describe the principal features of a material behavior in an idealized form. They are combined with other equations governing physical laws to resolve physical problems. SMAs are materials that undergo a phase transformation and therefore are characterized by a sequence of thermodynamic states that can be describe by combination of external(observable) and internal state, as the martensitic volume fraction. Thermodynamic state variables are all quantities that characterize a material body at a certain state. A certain thermodynamic state of a material can be described with a thermodynamic potential, that depends on state variables, both external and internal.

The constitutive model used here, follows the formulation proposed by Boyd and Logoudas. It is a thermodynamic model, based onto the expression of the Gibbs free energy, G. This potential, introduced in the first chapter, is defined as the portion of enthalpy available for doing work at constant temperature. The first step to described the constitutive model is the individuation of state variables.

Recall that the martensitic phase itself can exist in two different forms: the twinned and detwinned martensite. Moreover the twinned martensite is induced by cooling without causing macroscopic deformation. Detwinned martensite, on the other hand, is induced by stress that leads to macroscopic deformation. This transformation induced deformation, is associated with the *transformation strain*}, ε^T. Thus, the total strain can be additively decomposed into an elastic component, a transformation component and thermal component.

$$\varepsilon = \varepsilon^{EL} + \varepsilon^{TH} + \varepsilon^{T}$$

The *total martensitic volume fraction* is used to track the progression of the phase transformation, and it may include multiple variants, fully twinned, fully detwinned or some combination.

$$\xi = \xi^{Detw} + \xi^{Tw}$$

The constitutive model considers the martensitic volume fraction, and the transformation strain to be the internal state variables since both play an important role in characterizing the phase transformation and the observable thermomechanical response of SMAs.

The Gibbs free energy is a function of the independent state variable, σ, temperature, T, and of state variables, ξ and ε.

$$G = G(\sigma, T, \xi, \varepsilon)$$

At this stage all the necessary information is known and the constitutive equations governing the problem, are:

$$\varepsilon = S\sigma + \alpha(T - T_0) + \varepsilon^T$$

$$S = \frac{1}{E_A} + \xi\frac{1}{E_M} - \frac{1}{E_A}$$

$$\alpha = \alpha_A + \xi(\alpha_M - \alpha_A)$$

Where S is the compliance, α is the CTE, and T_0 is the reference environment temperature. In conclusion, the model is defined through the use of five state variables: strain ε, stress σ, temperature T, martensitic fraction ξ, and transformation strain ε^T .

The relation between the evolution of the transformation strain and the evolution of the martensitic volume fraction during forward or reverse transformation is assumed as:

$$\dot{\varepsilon} = \Lambda\dot{\xi}$$

Where λ is the transformation tensor, which determines the transformation strain direction, and is assumed to have the following form:

$$\Lambda = \begin{cases} H^{Curr} sign(\Sigma^{eff}) & when\ \dot{\xi} > 0\ (A \to M) \\ (\varepsilon^T_{max}/\xi_{max}) & when\ \dot{\xi} < 0\ (M \to A) \end{cases}$$

H^{curr} is the current maximum deformation strain (dependent on the applied stress); Σ^{eff} is the effective stress, ε_{max}^{T} is the maximal martensite strain ever reached in the process, and ξ_{max} is the correspondent martensitic fraction. The expressions $\dot{\xi} > 0$ and $\dot{\xi} < 0$ specify the transition phase direction.

Lagoudas defines an empirical formula for the definition of the Σ^{eff}, the effective stress, which causes the phase transition and depends on the martensitic fraction, the deformation, some material parameters and empirical coefficients *D*:

$$\Sigma^{eff} = \sigma + \left\{-D_3[-ln(1-\xi^d)]^{\frac{1}{m_1}} + D_2 H \xi^d + D_1\right\} sign(\varepsilon_m)$$

The strain evolution consequent to the martensitic fraction is treated as a plastic deformation, and a function Φ that determines the behavior of the transition is defined as follows:

$$\Phi = \begin{cases} +\Pi - Y & when\ \dot{\xi} > 0\ (A \to M) \\ -\Pi - Y & when\ \dot{\xi} < 0\ (M \to A) \end{cases}$$

During both forward and reverse phase transformations, the function Φ respects the conditions below:

$$\dot{\xi} \geq 0; \quad \Phi(\sigma, T, \xi) = +\Pi - Y \leq 0 \qquad \Phi\dot{\xi} = 0$$
$$\dot{\xi} \leq 0; \quad \Phi(\sigma, T, \xi) = -\Pi - Y \leq 0 \qquad \Phi\dot{\xi} = 0$$

The *Y* is a material constant, which defines the energy dissipation over volume due to a complete transformation, or it can be described as critical value for thermodynamic force to cause transformation. Π is the thermodynamic force, conjugated to ξ, which drives the transformations and it is representative of the chance that this phenomenon is occurring. It is experimentally defined by a function dependent on characteristic temperatures of the material and other materials parameters.

$$\Pi = \xi^{eff} + \frac{1}{2}\Delta\alpha(T - T_0) + \rho\Delta s_0(T - M^{OS}) + D_4\xi + \cdots$$
$$\ldots - \rho\Delta c[T - T_0 - Tln(1-\xi)] - D_5\left[ln(1-\xi)^{\frac{1}{m_2}}\right] + Y$$

3.2 SMA_UM: User Material Subroutine for SMAs

SMA_UM is a FORTRAN coded numerical implementation of an SMA thermo-mechanical constitutive model. The current version of SMA_UM implements the unified constitutive model presented by Lagoudas et al., which unifies and generalizes to three dimensions the constitutive models presented by Tanaka, Boyd and Lagoudas and Liang and Roger. The current implementation was developed on the specific user-subroutine of Abaqus®. So, modeling and analysis have been developed with this pre-post analysis software. The characteristics of the implementation are not treated in this context, details can be found in the various references. The finite element modeling of

the geometry has been developed using Abaqus/CAE, which compiles the input file .That is editable directly to run the subroutine for SMAs

The modeling requires several properties of the materials and specific post-process. Such characterization is essential for materials with a peculiar behavior as the SMAs. SMA_UM subroutine requires several materials parameters to be used: the Young's moduli of both austenite and martensite E^A and E^M, thermal expansion coefficients α^A and α^M, martensite start/finish and austenite start/finish temperatures at zero stress M^{0S}, M^{0F}, A^{0S} and A^{0F}, maximum transformation strain H and austenite and martensite stress influence coefficients, $\rho\Delta s^M$ and $\rho\Delta s^A$. Following is presented the standard procedure for the determination of the material constants.

- The **transformation temperatures** at zero stress can be determined from a Differential Scanning Calorimeter (DSC) test.
- The **stress influence coefficients** $\rho\Delta s^M$ and $\rho\Delta s^A$, presented in the first chapter as linked to the slope of the stress-temperature curve, can be determined from the stress-temperature phase diagram and a pseudoelastic test:

$$\rho\Delta s^A = -\frac{\sigma^A}{(T_{test} - A^{0S})} H = C^A H$$

$$\rho\Delta s^M = -\frac{\sigma^M}{(T_{test} - M^{0S})} H = C^M H$$

where T_{test} is the temperature at which the pseudoelastic test was performed and σ^A and σ^M are defined in previous figure (Figure 3.1). These coefficient are calculated only for the start transformation.

- The **elastic Young's moduli** are obtained from a uniaxial loading test, see Figure 3.1. The elastic stiffness of the austenite is determined by measuring the slope of the stress-strain curve at the beginning of the loading, where the material behavior is quasi-linear. The elastic stiffness of the martensite is determined by measuring the slope at the beginning of the unloading.

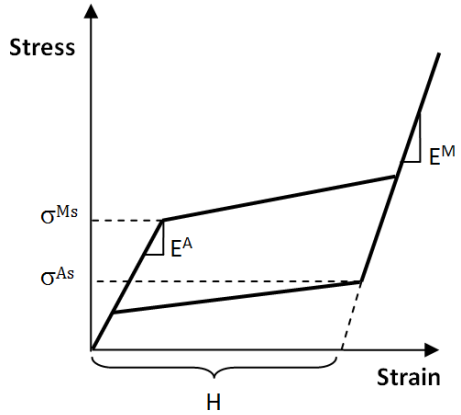

Figure 3.1 - Schematic of an SMA uniaxial pseudoelastic test

- The **maximum transformation strain**, *H*, can be obtained from a pseudoelastic test(Figure 3.1). It is the theoretical maximum strain recoverable.
- **Thermal expansion coefficients** (CTE) can be obtained by strain-recovery tests where the stress is constant and the driving force is the temperature. Usually the adopted value is α=22E-06, as suggested by the literature.

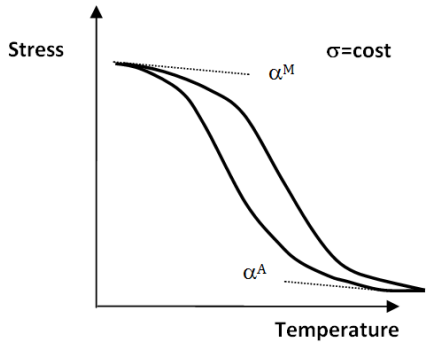

Figure 3.2 - Strain Recovery, coefficients of thermal expansion

The input file is compiled according to the conventions of the subroutine of Abaqus®. The properties of material are modified with the use of 24 constants. The command sequence is reproduced below.

```
*MATERIAL, NAME=SMA
*DENSITY
6450.0
*SPECIFIC HEAT
329.0
*CONDUCTIVITY
22.0
*DEPVAR
100
*USER MATERIAL , CONSTANTS=24
1.0 , 2.0 , 1.0E-8 , 0.0 , 16 , 55E+9 , 46E+9 , 0.33 ,
22.0E -6 , 22.0E-6 , 245, 230, 270, 280, 0.056 , -0.42E+06,
 -0.42E+06, 0.0 , 0.0 , 0.0 , 0.0 , 0.0 , 0.0 , 1.0}
```

The first few lines of command are common definitions of the property of any material in the output-file of ABAQUS/CAE®. The command line *USER MATERIAL and the keyword *DEPVAR gives the number of solution-dependent state variables.

Symbolically, the command line of *USER MATERIAL, is equivalent to writing:

```
*USER MATERIAL , CONSTANTS=24
IPHASE,MODEL,TOL,xi0,NELMTP,EA,EM,nu,
alphaA,alphaM,Mos,Mof,Aos,Aof,H,rDs0A,
rDs0M,epstr11,epstr22,epstr33,2epstr23,2epstr13,2epstr12,FRULE
```

- IPHASE: The phase of the material: 1 - austenite, 2 - martensite
- MODEL: The constitutive model: 1 - Tanaka's exponential model, 2 - Boyd and Lagouda's polynomial model, 3 - Liang and Rogers's cosine model
- TOL: Convergence criterion tolerance
- xi0: Initial value of the martensitic volume fraction
- NELMTP: Number of integration points in all SMA finite elements
- EA,EM: Young modulus for austenite and martensite, [Pa]
- nu: Poisson ratio
- alphaA, alphaM: Thermal expansion coefficient of austenite and martensite, [K^{-1}]
- Mos,Mof,Aos,Aof: Start(*s*) and finish(*f*) transformation temperatures of martensite and austenite, [K^{-1}]
- H: Maximum transformation strain
- rDs0A,rDs0M: Stress influence coefficient of austenite and martensite, [PaK^{-1}]
- epstrXX: Initial value of the XX-component of the transformation strain tensor
- FRULE: Flag for the form of the transformation tensor.

3.3 Example

Following is presented a simple example to show the algorithm performances. The analysis is done in the case of material in the austenitic phase, $T_{test} > A_{Of}$ in order to highlight the hysteresis of material.

Four tests were carried out to show the behavior of material at four different temperatures: 25°C 35°C 45°C 55°C

The model has been loaded with tensile force and it adopts 9x1 3D elements, in order to investigate also the deformation outside the plane. The number of elements is sufficient to describe the problem and it has been verified with other models that a more refined mesh.

The properties of the material used for the test are:

Material Parameter	Value
E^A	55 GPa
E^M	46 GPa
M^S	-28°C
M^F	-43°C
A^S	-3°C
A^F	7°C
$C^A=C^M$	7.4 MPa/°C
H^{max}	0.056

Table 3.1 - Standard parameters used for Lagoudas implementation

The figures below refers to the central element, that is not affected by boundary conditions.

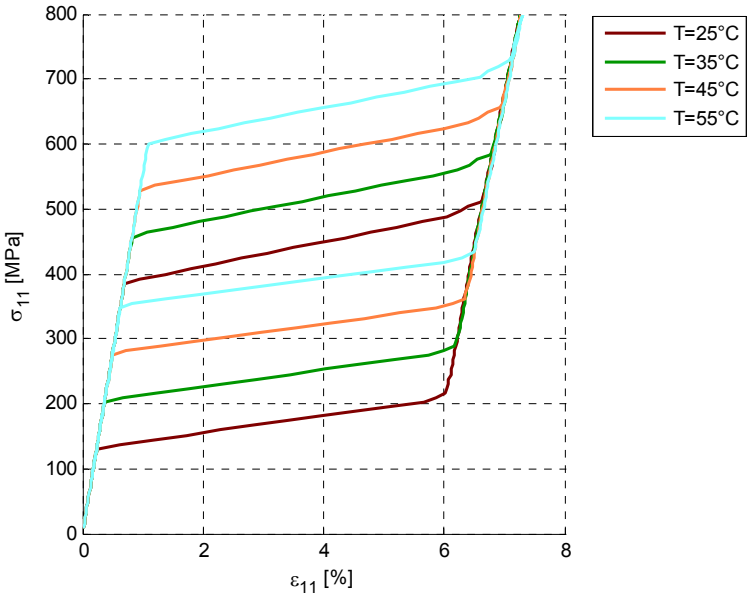

Figure 3.3 - Pseudoelastic loading/unloading results for various numerical test

The values of stress to induce martensite and austenite are defined to one temperature. In fact, they increase with temperature, as the Clasius-Clapeyron (dσ/dT) curve describes.

The values of stress influence were obtained by interpolating the data of some tensile tests. The same coefficients can be calculated by the analytic formula of the slope coefficient of curve $\sigma - T$:

$$C^M \sim 7.16\ MPa/°C \qquad C^A \sim 6.78\ MPa/°C$$

The error between values is ~3% for C^M and ~8% for C^A. Using these values into Lagoudas algorithm the behavior of material slightly changes, as it can be noted by figure below, at 25°.

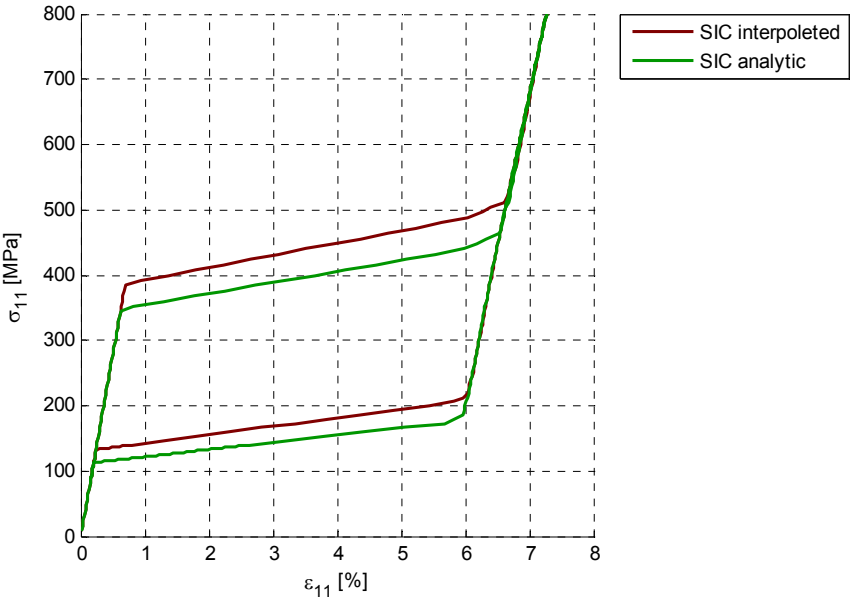

Figure 3.4 - Stress influence coefficients (SIC) compared

3.4 Sensitivity

The simulation of material behavior depends on how its parameters are chosen.

A Matlab® script able to change some parameters in the command line *USER MATERIAL has been written. The program read one output file of Abaqus/CAE where there are the geometry and finite elements discretization; it seeks the user material command line and writes a new material or change some parameters. Finally the end it launches the Abaqus analysis and reads the results.

The script allows the selection of the geometry type and the 12 material variable parameters:

var =[M0s M0f A0s A0f H EA EM T_test sigmaA sigmaM CA CM]

- M0s: start martensitic temperature at zero stress
- M0f: start martensitic temperature at zero stresses
- A0s: start austenitic temperature at zero stress
- A0f: start austenitic temperature at zero stress
- H: maximum strain transformation
- EA: austenitic Young's modulus
- EM: martensitic Young's modulus
- T_{test}: test temperature

- σ_A: stress of star austenitic transformation
- σ_M: stress of star austenitic transformation
- C_A: slope austenitic coefficient
- C_M: slope martensitic coefficient

A specimen characterized by experimental test (DSC, uniaxial loading), has been analyzed. It is a sample of NiTi wire, of length 100 mm and diameter 1.2 mm, divided in 15 truss elements: it is encastred on one side and loaded on the other side. The characteristic of a wire is that it responds more uniformly then a strip, and it is more easy the parameters detection.

The experimental behavior of uniaxial loading test at 81°C is show in figure below.

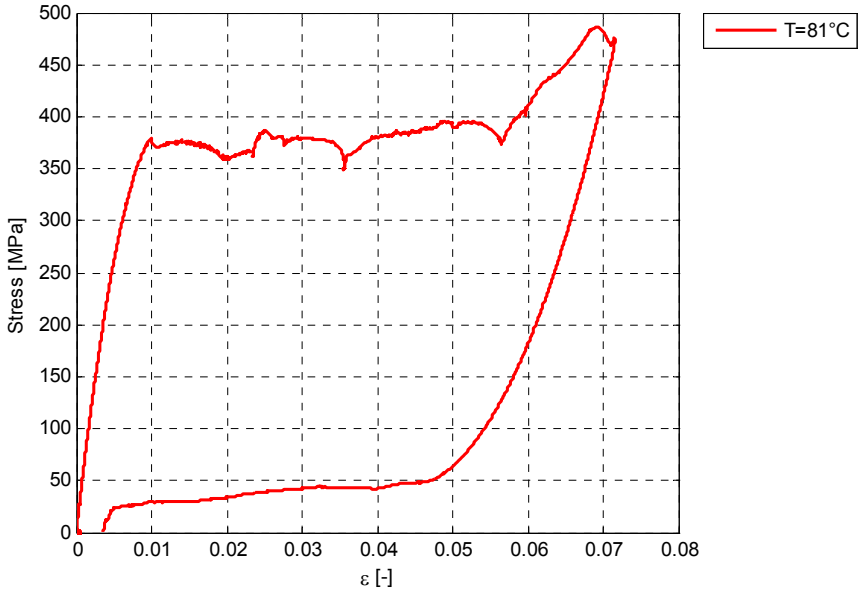

Figure 3.5 - Uniaxial loading test

Using the equation at page 32 for the slope coefficients, the parameters obtained by the uniaxial loading test at 81°C, are:

Material Parameter	Value
E^A	56 GPa
E^M	32 GPa
M^S	4.7°C
M^F	-20.5°C
A^S	50.7°C
A^F	65.4°C
H	5.2 %
C_A	1.548E+6 Pa/K
C_M	4.9934E+6 Pa/K

Table 3.2 - Sensitivity

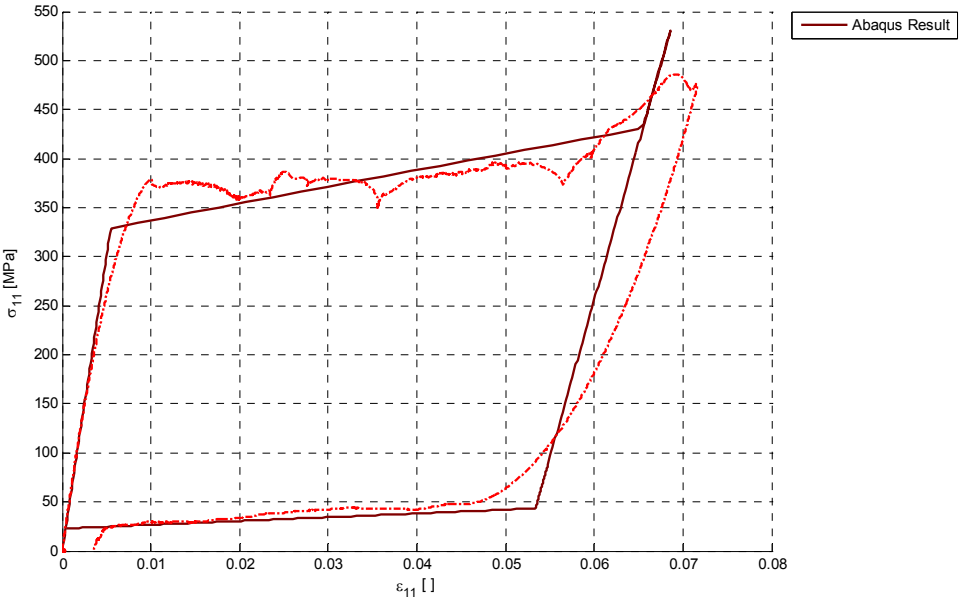

Figure 3.6 - Numerical-Experimental test at T=81° C

The script has been used to evaluate the sensitivity of material behavior respect to algorithm parameters. The sensitivity analysis has been done varying the selected parameters (one by one) of a certain value. The modification of the stress-strain curve has been then investigated. It must be careful that some of the parameter changes can lead to non-convergence conditions.

Young's moduli

The values of Young's moduli of martensite and austenite are changed and all the other parameters are constant. The reference curve, that uses the value of Table 3.2 is ID 3. (Figure 3.7)

Curve ID	E^A [GPa]	E^M [GPa]
-1-	48	26
-2-	52	28
-3-	56	32
-4-	61	35
-5-	67	38

Table 3.3 - Curves and values of sensitivity with respect to E

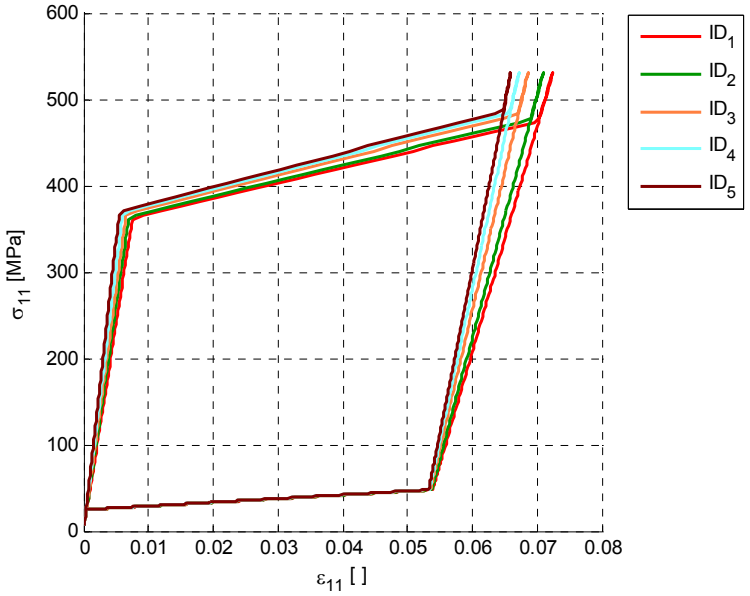

Figure 3.7 - Sensitivity, Young's moduli

It can be noted the modulus variation influences the value of start and finish transformation stresses, both for loading and for unloading phase. The maximum transformation strain is constant.

Maximum transformation strain

The maximum transformation strain locates the right limit of hysteresis and the intersection of x-axis with the extension of the unloading curve. It is difficult have a value that responds proper in different numerical test conditions. All parameters are constant and H is changed, the curve reference is the ID 3. (Figure 3.8)

Curve ID	H [%]
-1-	4.8
-2-	5.0
-3-	5.2
-4-	5.4
-5-	5.6

Table 3.4 - Curves and values of sensitivity with respect to H

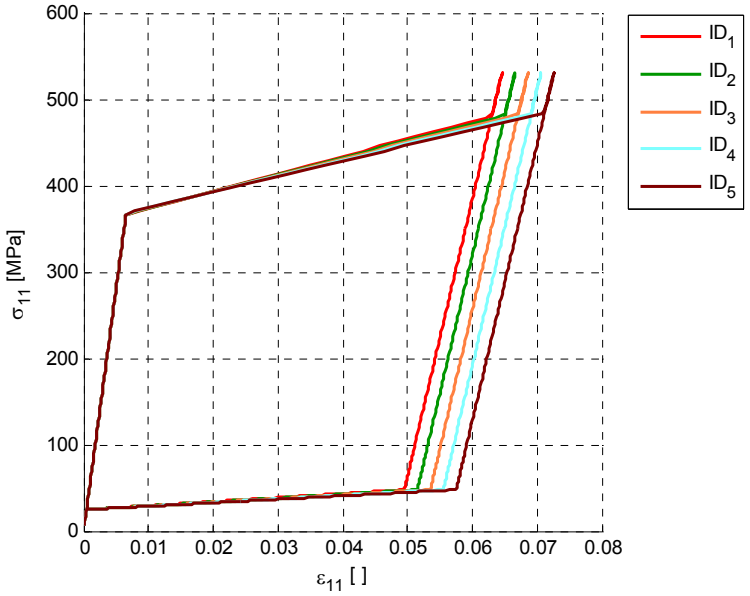

Figure 3.8 - Sensitivity, Maximum transformation strain H

The area of hysteresis is almost constant, while the martensitic transformation plateau raise and its slope is increased. An observation of H is affected when the temperature varies test. Experimentally should close the area of hysteresis and reduced H. In fact this behavior is not respected by the sub routine. (Figure 3.9)

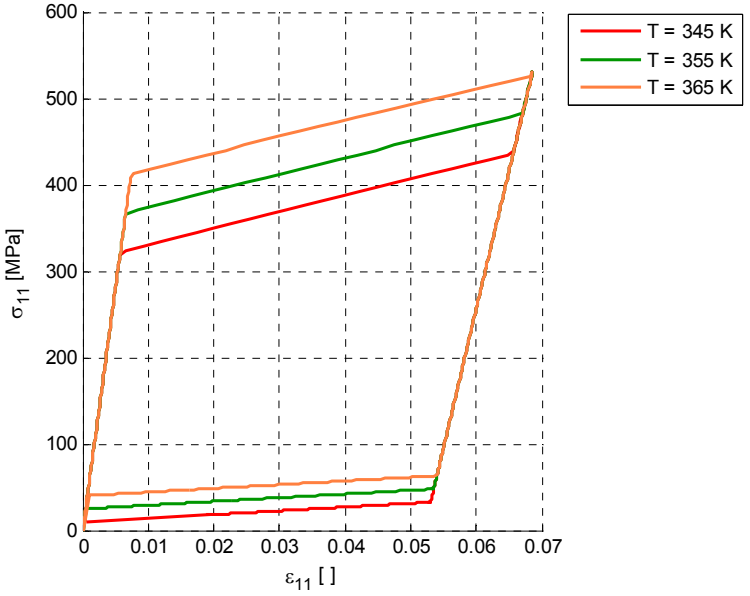

Figure 3.9 - Maximum transformation strain with test temperature variation

Start transformation stress of martensite and austenite

The change of σ^{As} and σ^{Ms} modifies also the stress influence coefficient as described in equation at page 32. The main effect is to raise the plateau with constant slope. In first figure σ^{Ms} is changed in the second only σ^{As}. The curve reference for σ^{Ms} is ID 1. (Figure 3.10 and Figure 3.11)

Curve ID	σ^{Ms} [MPa]
-1-	355
-2-	365
-3-	375

Table 3.5 - Curves and values of sensitivity with respect to σ(Ms)

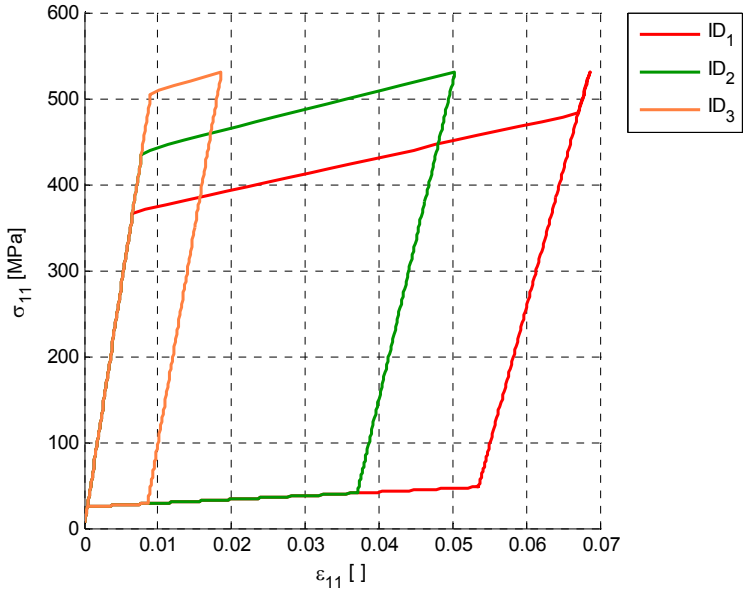

Figure 3.10 - Sensitivity, σ^{Ms} variation

Curve ID	σ^{As} [MPa]
-1-	48
-2-	55
-3-	60

Table 3.6 - Curves and values of sensitivity with respect to σ(As)

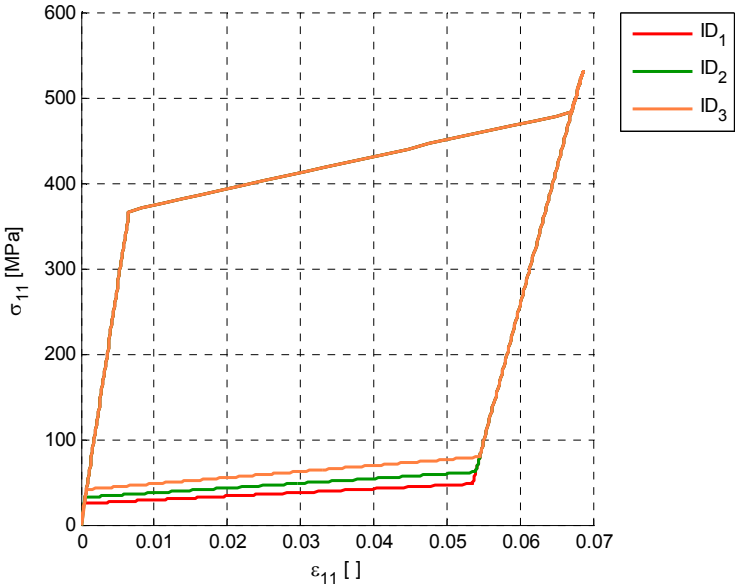

Figure 3.11 - Sensitivity, σ^{As} variation

Start and finish transformation temperature: phase martensite

In first figure the M^{0s} has been changed, and it can be noted as an increase of temperature modifies the slope of plateau and reduces the start stress martensite transformation. The same observation is also valid for M^{0f}, the value of finish stress martensite transformation. (Figure 3.12 and Figure 3.13)

Curve ID	M^{0S} [K]
-1-	270.85
-2-	277.85
-3-	285.85

Table 3.7 - Curves and values of sensitivity with respect to M^{0S}

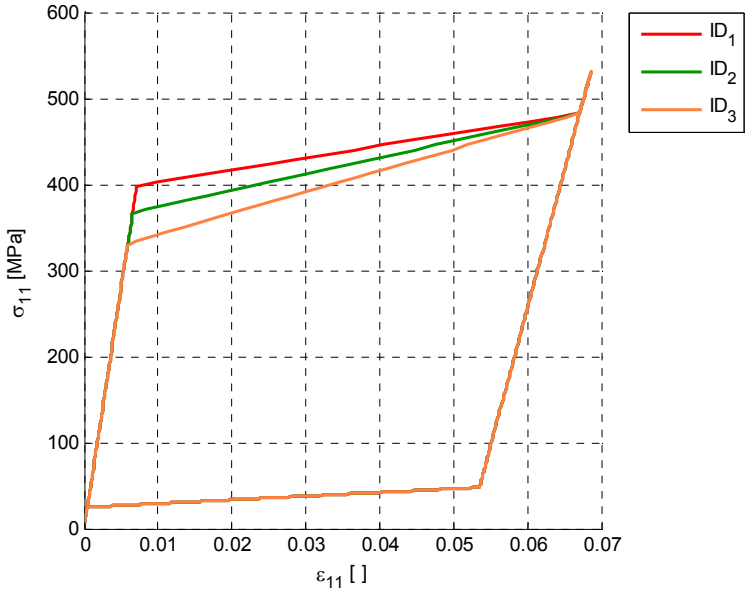

Figure 3.12 - Sensitivity, M^{0s} variation

Curve ID	M^{0F} [K]
-1-	245.65
-2-	252.65
-3-	260.65

Table 3.8 - Curves and values of sensitivity with respect to M^{0F}

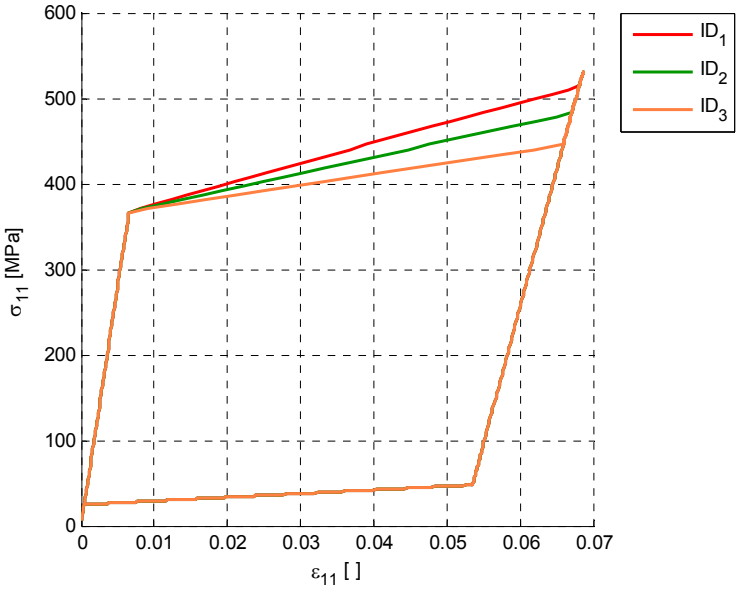

Figure 3.13 - Sensitivity, M^{0f} variation

Start and finish transformation temperature: phase austenite

An increasing of austenitic start and finish temperature, A^{0s} and A^{0f}, causes a reduction of start stress austenitic transformation and finish stress austenitic transformation. (Figure 3.14 and Figure 3.15)

Curve ID	A^{0S} [K]
-1-	313.85
-2-	323.85
-3-	333.85

Table 3.9 - Curves and values of sensitivity with respect to A^{0S}

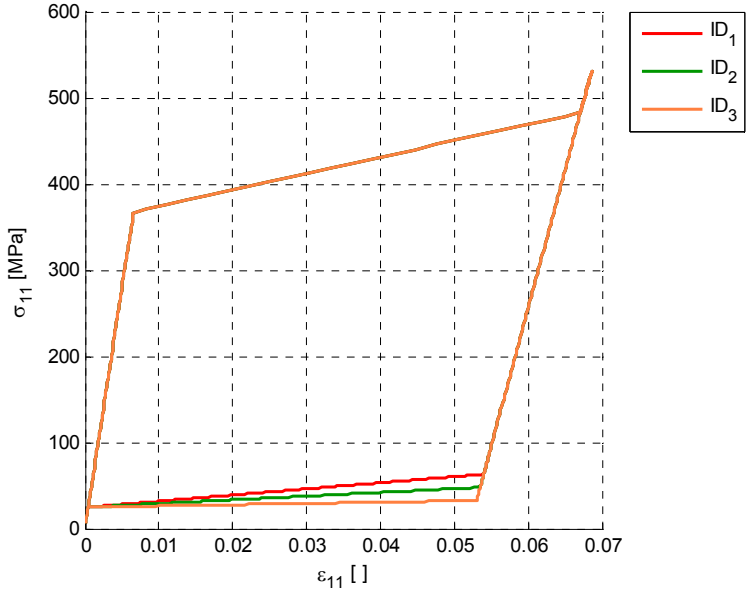

Figure 3.14 - A^{0s} variation

Curve ID	A^{0F} [K]
-1-	328.85
-2-	338.85
-3-	348.85

Table 3.10 - Curves and values of sensitivity with respect to A^{0F}

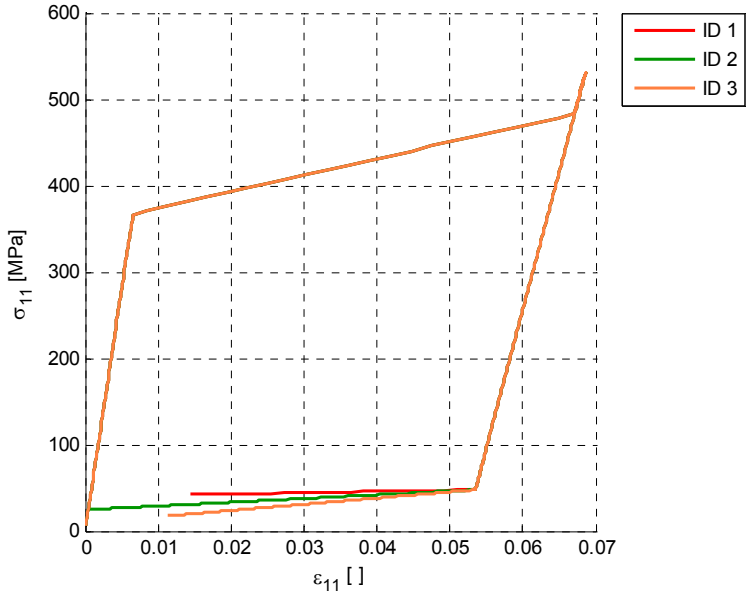

Figure 3.15 - A^{0f} variation

In the graph it could be noticed that the curves 1 and 3 do not reach convergence and so do not close the hysteresis loop. This is probably due only to numerical difficulties.

Martensitic and austenitic transformation temperatures

It can be changed the values of temperature by keeping constant the difference between start and finish transformation temperatures. This changing modifies the slope of transformation curve and the values of stress transformation. (Figure 3.16 and Figure 3.17)

Curve ID	M^{0F}-M^{0S} [K]
-1-	277.85-252.65
-2-	287.85-262.65
-3-	297.85-272.65

Table 3.11 - Curves and values of sensitivity with respect to ΔM

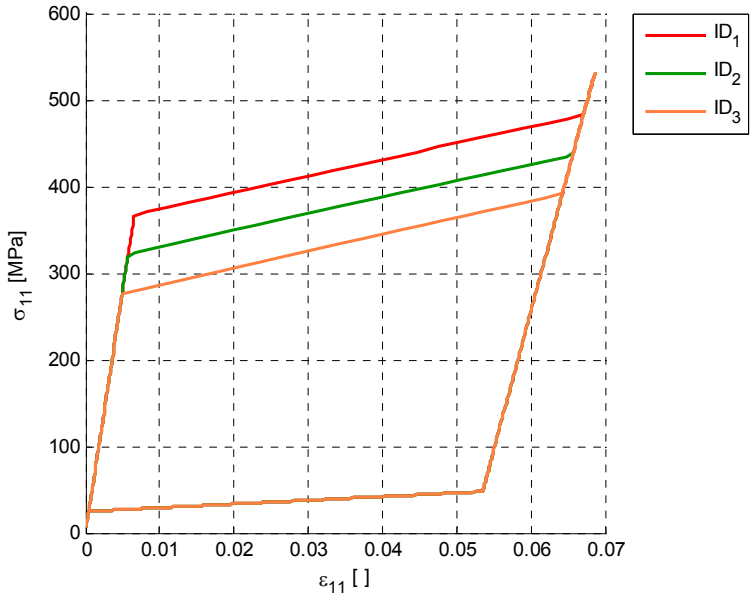

Figure 3.16 - ΔM temperature increase

Curve ID	A^{0F}-A^{0S} [K]
-1-	323.85-338.85
-2-	313.85-328.85
-3-	303.85-318.85

Table 3.12 - Curves and values of sensitivity with respect to ΔA

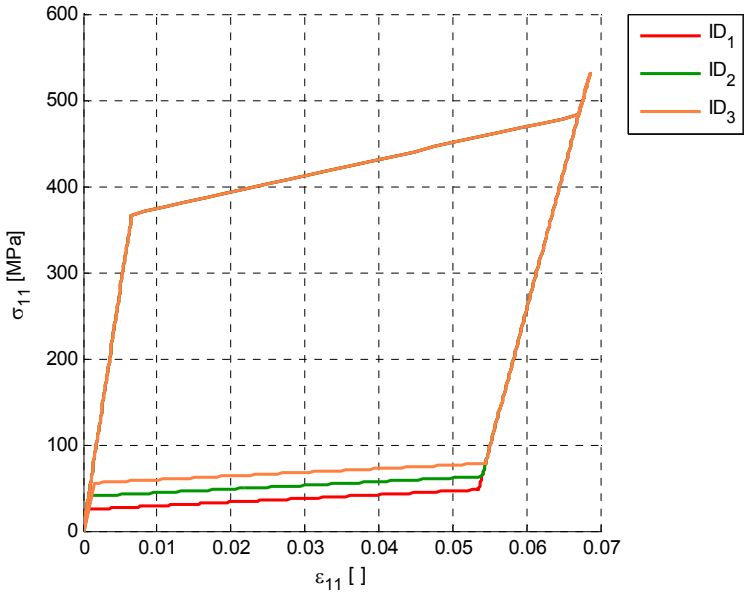

Figure 3.17 - ΔA temperature increase

Stress influence coefficients (*SIC*)

Only the sic parameters are changed so there is no needing to insert in the script the value of stress transformation.(Figure 3.18 and Figure 3.19)

Curve ID	SIC austenitic [MPa/K]
-1-	1.548
-2-	2
-3-	2.58

Table 3.13 - Curves and values of sensitivity with respect to Austenitic SIC

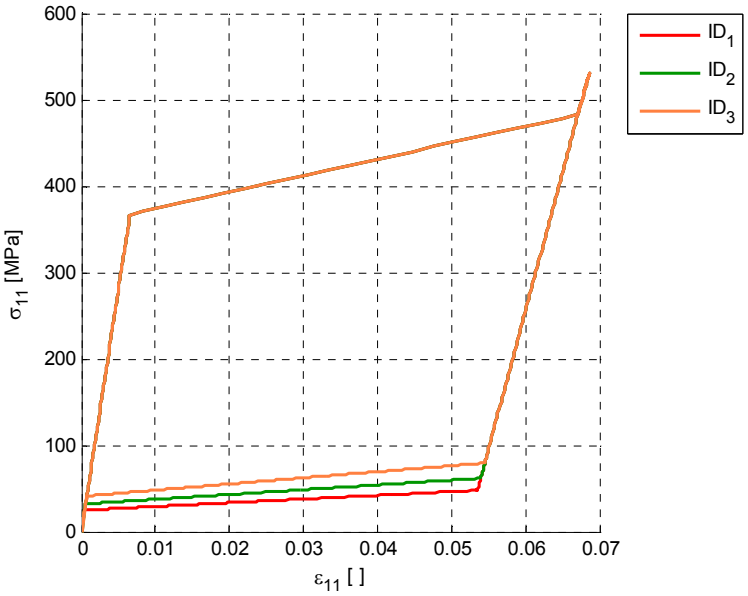

Figure 3.18 - SIC(A) variation

Curve ID	SIC martensitic [MPa/K]
-1-	4.9934
-2-	5.9934
-3-	6.9934

Table 3.14 - Curves and values of sensitivity with respect to Martensitic SIC

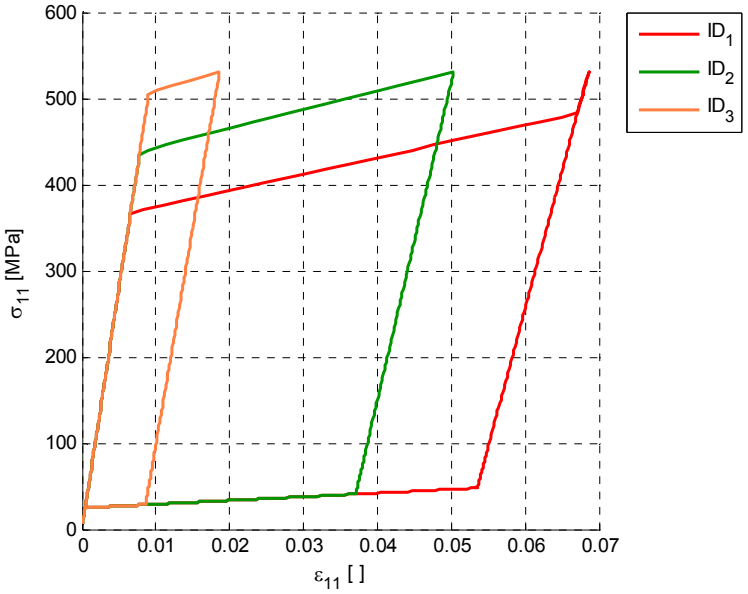

Figure 3.19 - SIC(M) variation

4 Experimental Characterization

4.1 Thermal analysis

Shape memory alloys can be produced, processed and even sold with very different thermal and mechanical characteristics, for which before use is necessary to perform a detailed characterization thermomechanical in order to investigate the exact behavior.

Due to the particularities of the Ni-Ti alloys already described in Chapter 1, it is clear that is essential first of all to identify the material phase transitions when the temperature changes. To do this it is used the *Differential Scanning Calorimetry* (i.e. DSC), which allows to highlighting the phase transformations and in particular the transformation temperatures, which are essential to perform correctly all the following mechanical analysis.

DSC is part of the family of thermal analysis, a group of techniques in which a physical property of a substance is measured as a function of temperature while the substance itself is subjected to a treatment temperature-programmed. Specifically, the property evaluated in the DSC is the difference between the heat flows in the substance to be characterized and in a reference one. The reference sample should have a well-defined heat capacity, constant over the range of temperatures to be scanned.

During the test both sample and reference are subjected to a heating at a controlled rate, made in inert atmosphere and with constant pressure to avoid the influence of chemical phenomena such as oxidation or other reactions.

The basic principle underlying this technique is that, when the sample undergoes a physical transformation such as phase transitions, more (exothermic process) or less (endothermic process) heat will need to flow to it than the reference to maintain both at the same temperature. By observing the difference in heat flow between the sample and

reference, the DSC is able to measure the amount of heat absorbed or released during such transitions.

The instrument used for this analysis is composed of a furnace and a measuring cell with a heat block and two platforms, on which should be placed two pans sample-holder containing the material to be analyzed and the reference one. The instrument detects the temperature difference (T_{sample} - $T_{reference}$) during the scan, by means of two thermocouples. With the available instrument, are possible scans in the temperature range [-150, 400]°C, at controlled scanning speed variable from 0.1 up to 100°C/min.

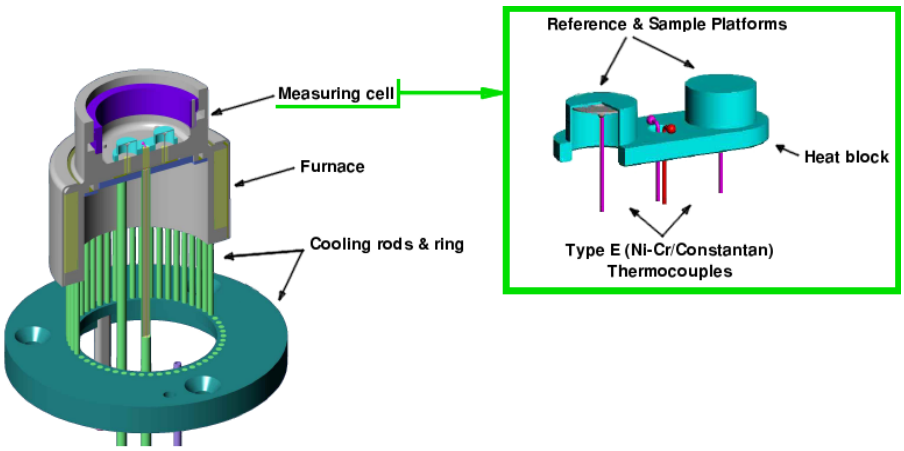

Figure 4.1 - Internal cell scheme and the detail of sensor assembly

The result of a DSC experiment is a thermograph, with heating and cooling curves. In the context of shape memory alloys the thermograph obtained is of the kind represented in Figure 4.2.

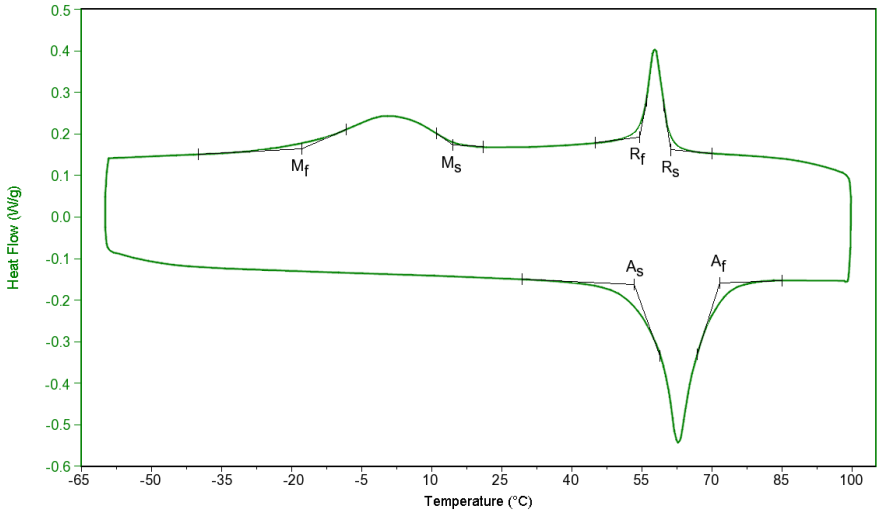

Figure 4.2 - Example of a DSC curve of a SMA, highlighting phase transformations

Starting from the far right of the graph and following the cooling curve, the first peak encountered is that of the phase transformation from austenite to rhombohedral. Even though it is calorimetrically very evident, from the mechanical point of view this transition is of little significance, corresponding to only about 1% of strain, even though it may be useful for some particular applications. Note that, as already explained in the chapter describing the SMAs, this step is not always present, so this peak may not occur.

Still proceeding on the upper curve of the graph we observe the proper martensitic transformation, pointed out by the second peak. This leads to low temperatures, therefore proceeding in the opposite direction along the heating curve, it is encountered the inverse transformation, which bring the phase back again from martensite to austenite.

It is evident from the graph that the martensitic transformation is exothermic, indeed it releases heat in the transition from parent phase to product one. The inverse transformation clearly is endothermic, with absorption of heat corresponding to the down peak.

By applying the method of the tangents to the various peaks, are obtained temperatures of the start and end of the transformations, as shown in Figure 4.2. Removing the trace obtained when the pan of the sample is empty, the so-called baseline is obtained. The area enclosed between the curve and the baseline is proportional to the enthalpy exchanged during transformation.

It should be noted that the shape of the peaks and the temperature ranges that identify the two phases can be very different depending on the type of alloy and heat treatment that it has undergone. So from the presence of multiple peaks, from their width and shape and from the enthalpies, we can extract information about the microstructural state of the alloy.

4.2 Mechanical analysis

From the mechanical point of view, the tests that are performed on NiTi materials do not differ much from those for other metals. The data obtained are the classic ones of metals (elastic modulus, yield stress, etc..) and in addition those characteristic of shape memory alloys, which will be described in detail in the following paragraphs with regard to specific graphs.

The issue on which we must always be focused is the combination of the two driving forces: stress and temperature. As part of this thesis were carried out Stress-Strain (SS) tests, with cycles of loading and unloading at constant temperature, both in tensile and bending configuration, and Strain-Recovery (SR) tests, where the stress level remains fixed and changes the temperature.

To perform the mechanical tests two instruments have been exploited: an MTS (*Mechanical Testing System*) and a DMA (*Dynamo-Mechanical Analyzer*).

With reference to the MTS, the device installed is a machine MTS 2\M of the electromechanical type, with a 10kN load cell equipped with micro-strain gage with gauge length of 25 mm and span +/-20%. The climatic chamber cooled with liquid nitrogen allows to perform measurements in the range [-90C, +250 C]. A pair of pneumatic grippers of 10kN allows controlling the clamping force of the sample in a reproducible way.

Figure 4.3 - MTS: global and detail of the chamber

Figure 4.4 - DMA

The DMA supplied uses a non-contact, direct drive motor to provide the oscillatory or static force required. The force produced by the motor is then transmitted to the sample by means of a drive piston on air bearing (drive shaft). The direct control, therefore, is in force, while the displacement is measured by an optical linear encoder. DMA can also be defined as DMTA (Dynamo-Thermo-Mechanical Analyzer) because the temperature of the sample is controlled by a thermocouple and can be changed during the test, by means of a furnace and a gas cooling accessory. The other variables are derived and are calculated with the formulas associated with the tool. The sample is mounted via a locking mechanism (clamp). For the tests carried out, it has been exploited a mounting of the type Tension, for tensile test, and one of the type Single Cantilever, for bending tests, in which the sample is blocked at both ends: to one of the fixed supports and to the shaft.

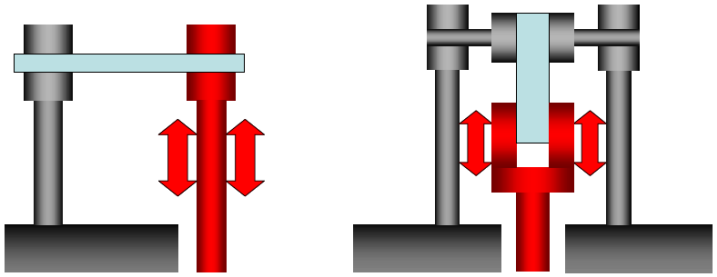

Figure 4.5 - Single cantilever (left) and Tension (right) mounting

For application limits of the two different machines, the SS tests in bending and SR tests were usually performed with the DMA, while SS tests in tension both with DMA or MTS.

4.3 Dynamic analysis

To determine the characteristics of isolation and damping, a dynamic mechanical test is performed, where a sinusoidal force is applied to the material (at constant maximum strain) and a resultant sinusoidal strain is measured.

Also measured is the phase difference δ, between the two sine waves. The phase lag would be 0° for purely elastic materials and 90° for purely viscous materials (a symbolic representation is in the first line of Figure 4.6). Viscoelastic materials will exhibit an intermediate phase difference (second line of Figure 4.6).

Since modulus equals stress/strain, the complex modulus E* can be calculated. From E* and the measurement of δ, the storage modulus E^{I} and loss modulus E^{II} can be calculated. The storage modulus is the elastic component and related to the sample's stiffness. The loss modulus is the viscous component and is related to the sample's ability to dissipate mechanical energy through molecular motion.

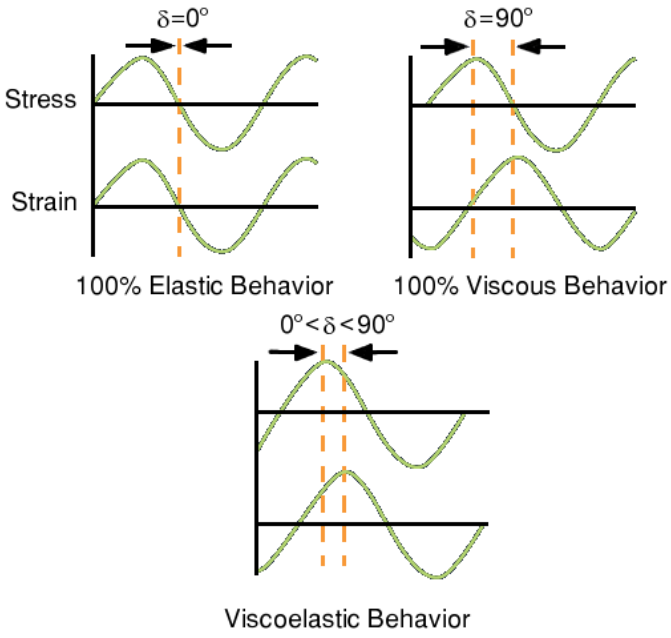

Figure 4.6 - Graphical representation of the phase shift

The tangent of phase difference, or tan(δ), is the common parameter that provides information on the relationship between the elastic and inelastic components. It represents the q^{-1} or the internal friction of the material.

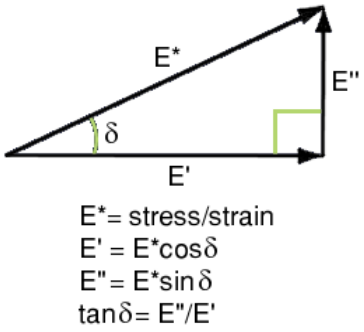

Figure 4.7 - Graphical representation of damping and the parameter tanδ

4.4 Extraction of Lagoudas parameters for specific materials

Were performed numerous tests on different materials. At the end have been selected three materials that are considered significant for three different ways to derive the parameters of interest. They are different NiTi alloys, and also have different geometry and thermal treatment. Following they will be indicated with codes that indicate the geometry and the thermal treatment undergone:

1 - wire, diameter 0.3mm, thermal treatment n°7
2 - wire, diameter 1.2mm, no thermal treatment (supplier)
3 - strip, section 4x0.5 mm, thermal treatment n°2

4.5 Material 1: Wire 0.3 mm Thermal Treatment 7

This material was a wire of small diameter, which then can produce sufficient stress, even with a relatively low load and is therefore suitable to be characterized via DMA.

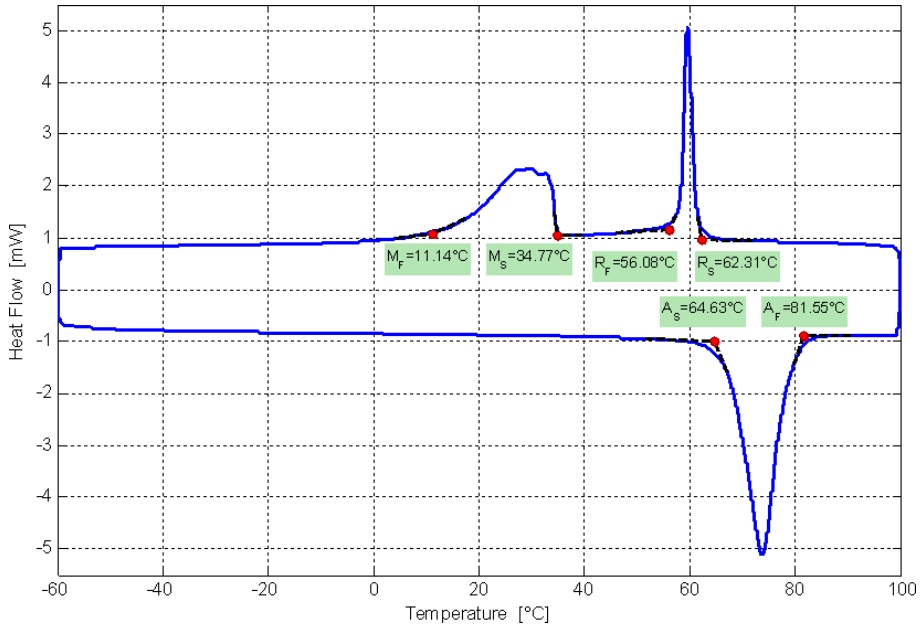

Figure 4.8 - Wire0.3TT7, DSC

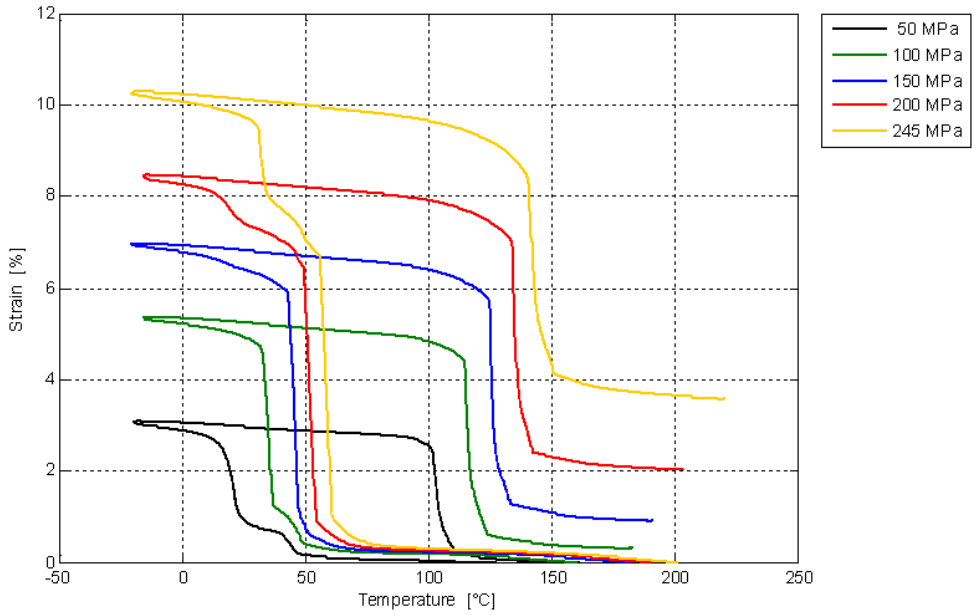

Figure 4.9 - Wire0.3TT7, DMA Strain Recovery Tensile test

The complete test expected to bring at settled stress levels and, once seated on them, vary the temperature thus inducing the transformation. The graph shows the result of this test carried out for a range of stress varying between 50 and 245 MPa. For values of greater stress are of course also reached values of higher deformation and also the residual strain is greater.

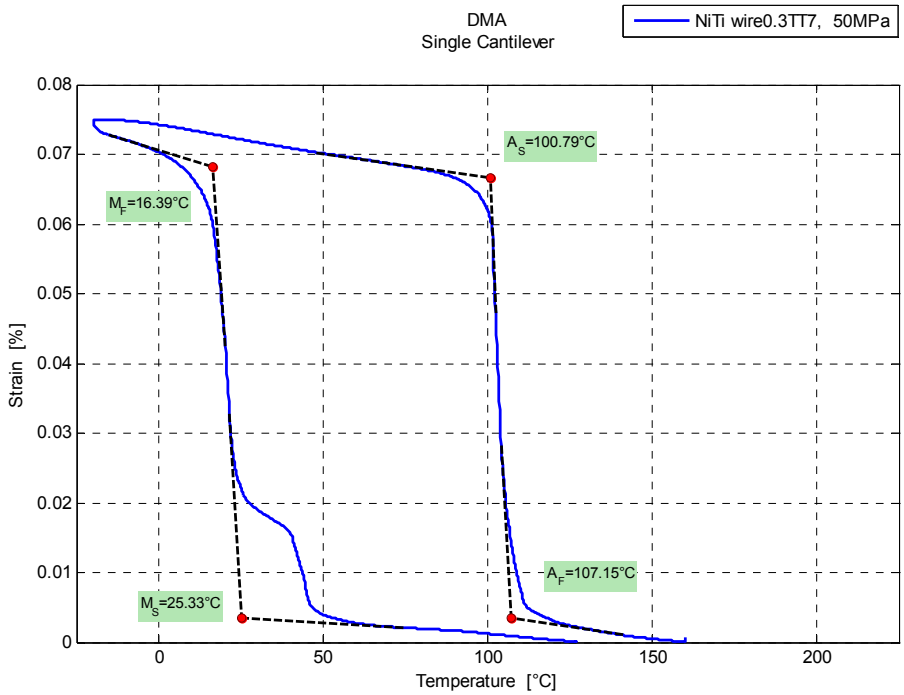

Figure 4.10 - Wire0.3TT7, SR: single temperature cycle

Again, to estimate the transformation temperatures are used the tangents. As an example it is reported the analysis carried out on the test at 50 MPa. The elbow at the temperature of martensitic transformation start can be skipped, because afferent to the rhombohedral phase, which is omitted for our purposes.

By performing a quite similar analysis of the curves also to other levels of stress, we obtain the data shown in the table below. With these data we obtain the stress influence coefficient values.

Stress [MPa]	0	50	100	150	200	245
M_S [°C]	34.77	25.33	37.61	47.84	54.51	60.88
M_F [°C]	11.14	16.39	31.99	41.96	47.66	53.00
A_S [°C]	64.63	100.79	113.84	124.16	133.46	139.79
A_F [°C]	81.55	107.15	119.18	128.13	137.37	145.24

Table 4.1 - Transformation temperatures at different levels of Stress

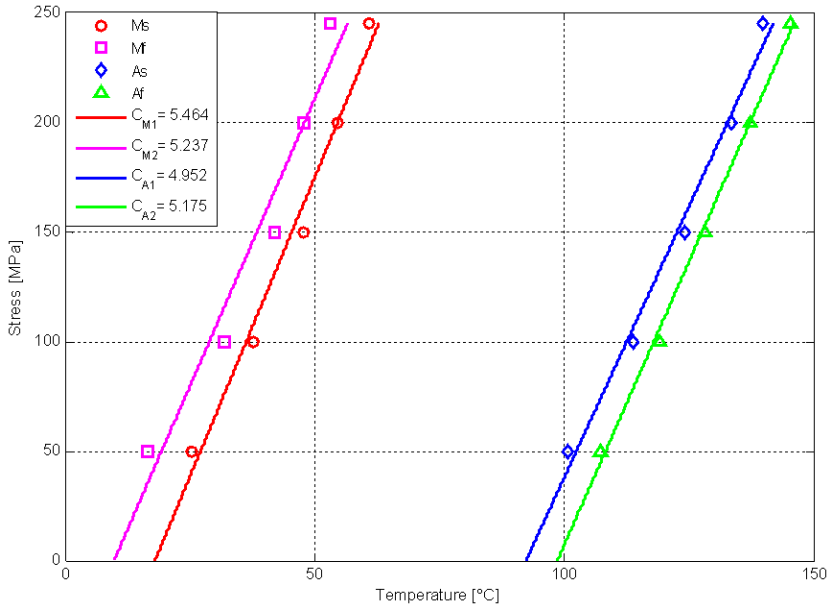

Figure 4.11 - Wire0.3TT7, Experimentally Derived Phase Diagram

In this case, in the linear regression are excluded the data at zero stress (i.e. those of DSC). This is because the furnace of the DMA has a certain hysteresis in the temperature: as a systematic error, if the data are all derived from the same tool it is negligible for evaluating the slope of the stress-temperature rate, but it becomes important if these data are associated with those of DSC (much more accurate temperature) or if they are needed as absolute values.

To more accurately estimate the slope is affordable to be based on data from the austenite transformation. In fact, the martensitic one is disturbed by rhombohedral transformation and provides less precise data. In addition, the martensite is transformed only with the de-twinning, while the austenite first induces the martensite to stress and then twins, then also presents the actual crystallographic transformation. In addition, the martensite has a ratio stress-temperature less definite when it comes down to low values of stress (see graph of the phase diagram below).

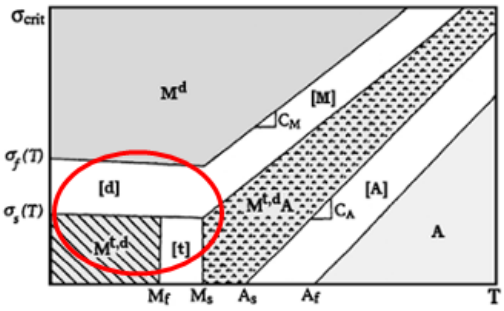

Figure 4.12 - Phase Diagram, in the circle the region at low stress with the less definite ratio stress-temperature

For each value of stress is derived also H, as the difference between the maximum strain reached and the non-recoverable amount.

Stress [MPa]	H [%]
50	3.086
100	5.028
150	6.029
200	6.426
245	6.670

Table 4.2 - Wire0.3TT7, Max. transformation strain

To obtain the values of the elastic modules, stress-strain test are needed. In this case they are performed with DMA in tensile configuration.

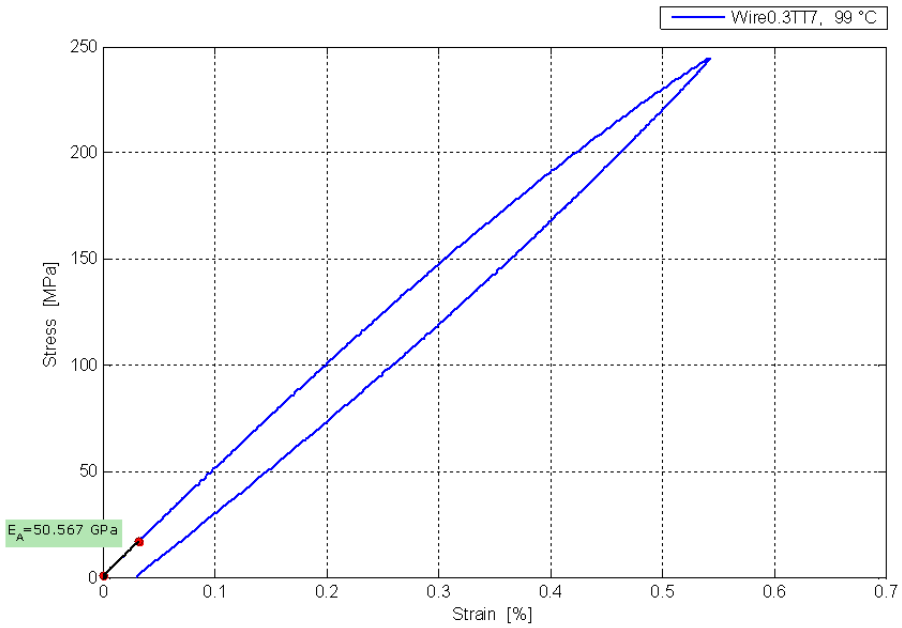

Figure 4.13 - Wire0.3TT7, DMA Tensile test, austenite

The limit imposed by the load cell (18N) prevents to investigate the curve in austenite beyond the 0.5% strain. This value is however sufficient to evaluate the elastic modulus, but not the start stress for the induction into martensite.

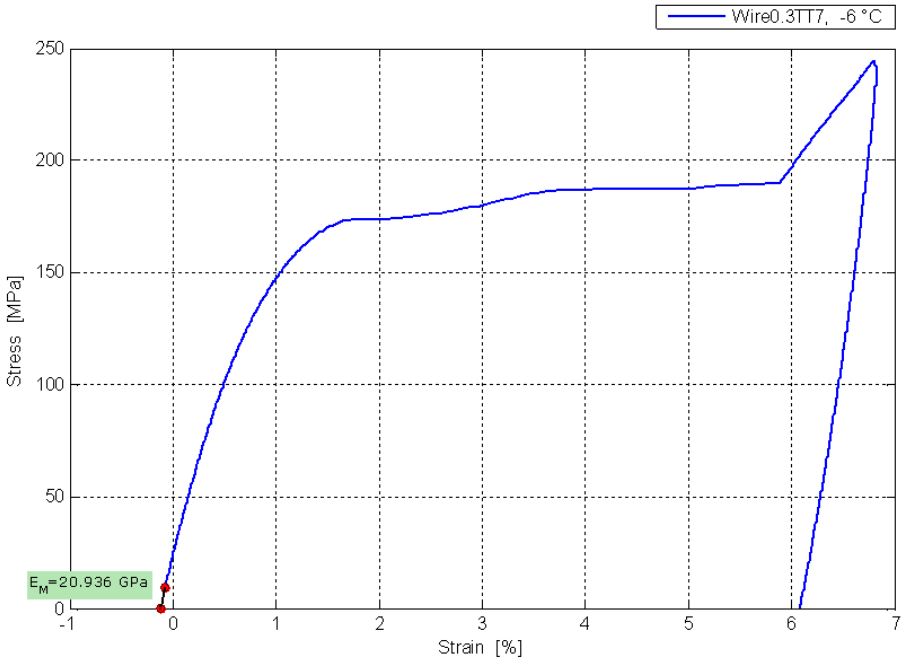

Figure 4.14 - Wire0.3TT7, DMA Tensile test, martensite

M_S	34.77 (307.92)	°C (K)
M_F	11.14 (284.29)	°C (K)
A_S	64.63 (337.78)	°C (K)
A_F	81.55 (354.70)	°C (K)
E_A	50.651	Gpa
E_M	20.936	GPa
H	5.45	%
C_M	5.35	MPa/K
C_A	5.06	MPa/K

Table 4.3 - Summary of average parameters for Wire0.3TT7

4.5.1 Material 2: Wire 1.2 mm No Thermal Treatment

This material was tested as received from the supplier, without any additional heat treatment. From the DSC test, the transformation temperatures results:

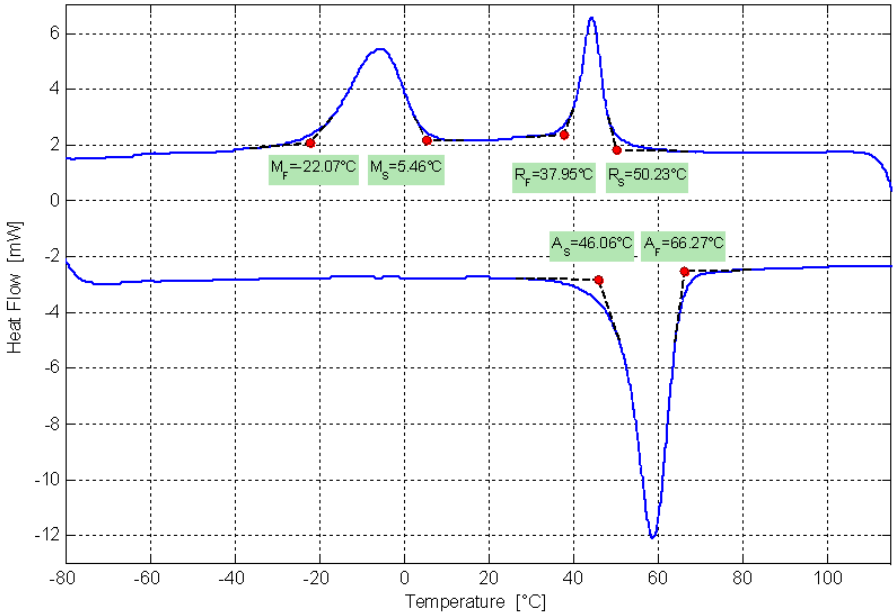

Figure 4.15 - Wire1.2TT0, DSC

To characterize the material this time have been exploited more sets of tensile tests at different temperatures beyond A_F. For each test were performed the same analysis, of which the first is reported only by way of example. The summary results are shown in Table below.

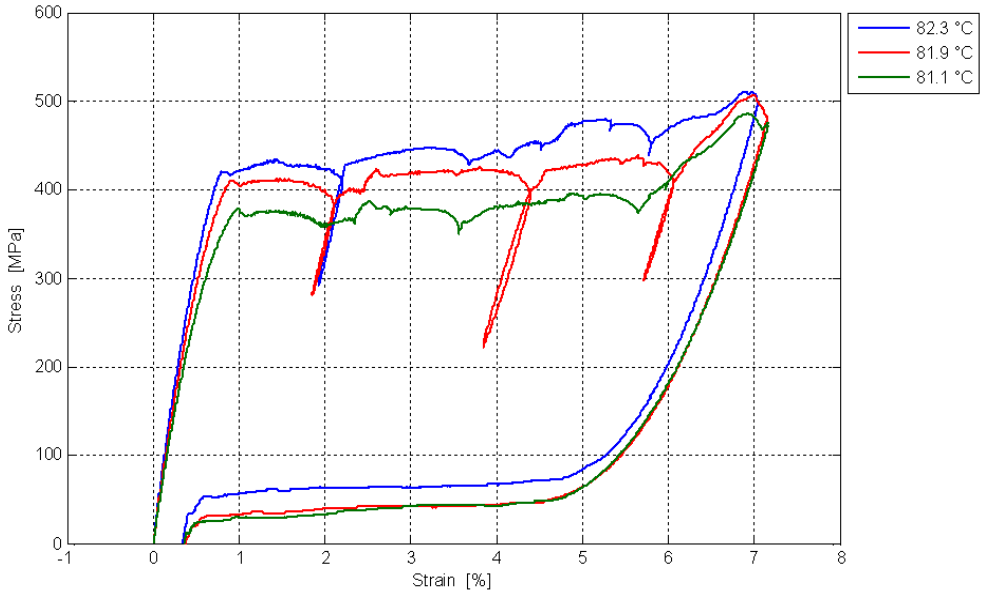

Figure 4.16 - Set of test at about A_F+15

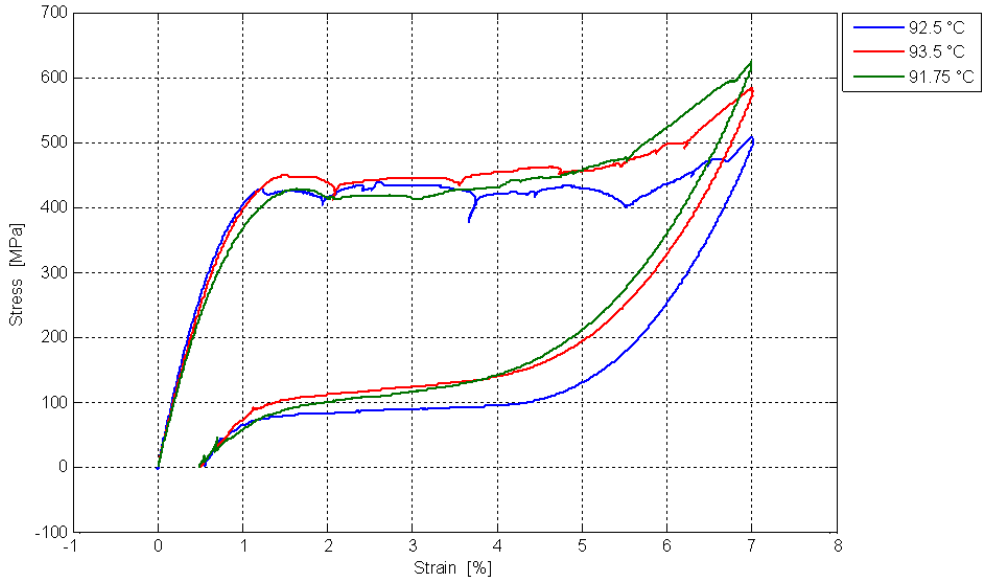

Figure 4.17 - Set of test at about A_F+25

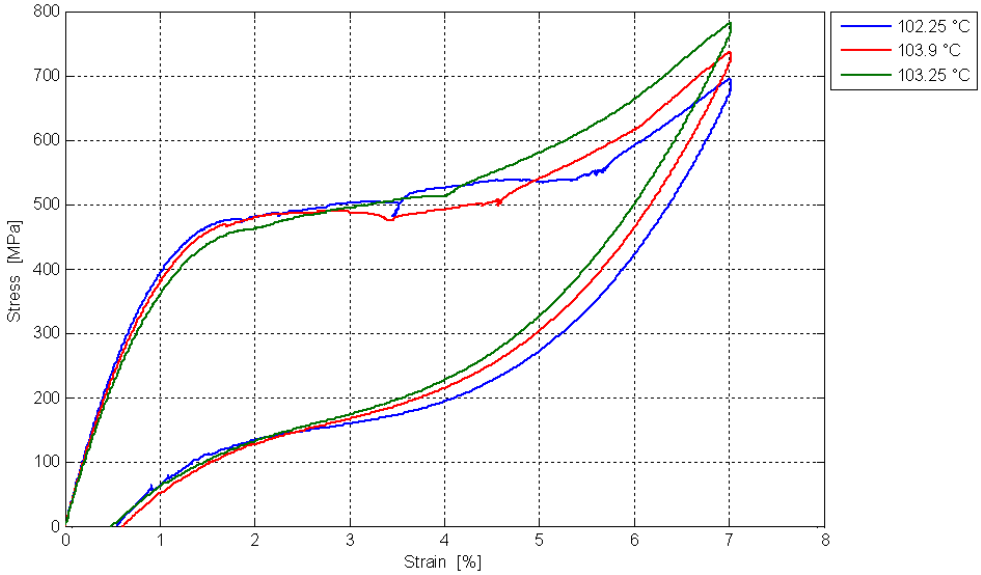

Figure 4.18 - Set of test at about A_F+35

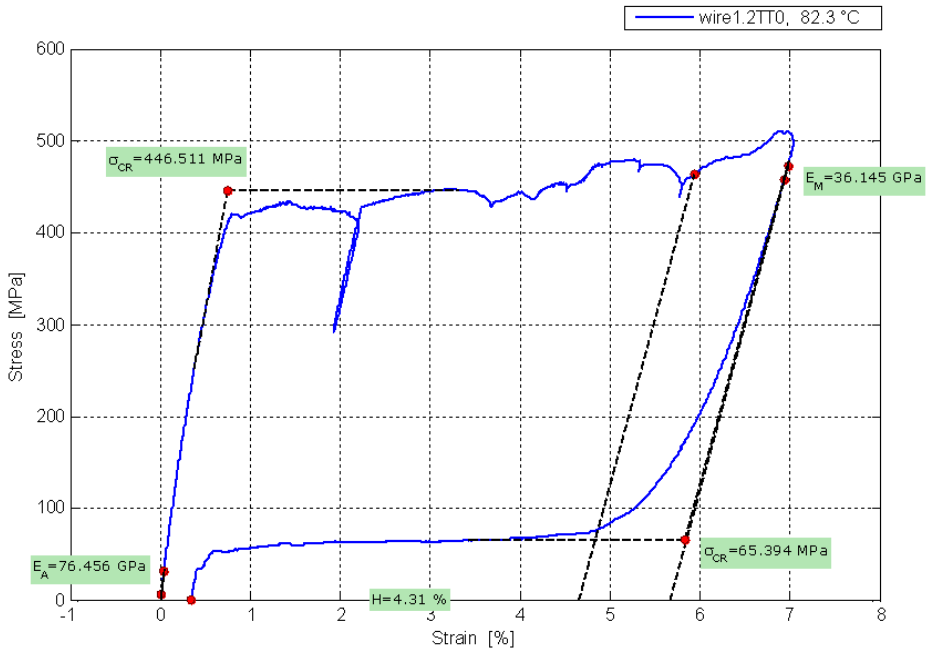

Figure 4.19 - Wire1.2TT0, Example of extracted parameters for the first test

As already mentioned between the data to be collected figures the classic elastic modulus of the material. In this case the modules are two: the first one of the austenite phase (the test temperature being more than AF, is that relative to the first portion of the load curve), the second one of the martensitic phase induced under stress.

Another couple of important parameters are formed by the critic stresses of start induction of martensite and start return to austenite. The first of these identifies the plateau of the load path: under the effect of the applied force, the martensite is induced with the variants that orient themselves in the preferred direction of stress, opposing then poor tensile strength, for which the deformation increases while maintaining the constant stress. The second critic stress identifies the unloading plateau: being the martensite phase unstable at these temperatures, when removing the load the alloy returns spontaneously to the austenitic condition.

The small loop that can be seen in the middle of the upper plateau is a lack in the control of the machine, which can happen when the slope of the plateau is not regular, for internal effects of the material (for example, the settling of a variant of martensite which was previously blocked).

The last parameter calculated directly from this test is the maximum transformation strain H. It is calculated starting from the end point of the plateau and projecting it on the zero-stress axis with the slope of the elastic modulus of martensite. From this value should be subtracted the amount of any residual strain. In this way we obtain the percentage of deformation to be fully recoverable.

Finally, it is necessary to obtain the relationship between stress and temperature. To do so are linked the stresses obtained for the test temperature, to the transformation

temperatures obtained from the DSC. This is possible only because the temperature of the specimen during the test is measured directly with a thermocouple, and is therefore sufficiently precise to be comparable with those of the DSC.

Af= 65.4							
Temp. [°C]			$\sigma(M_S)$	$\sigma(A_S)$	E_A	E_M	H
82.30	Af+	16.9	446.511	65.394	76.456	36.145	4.310
81.90	Af+	16.5	424.700	62.518	70.403	32.917	4.520
81.10	Af+	15.7	378.261	58.692	64.610	32.002	4.190
				mean values =	70.490	33.688	4.340
92.50	Af+	27.1	432.947	102.907	60.572	29.720	3.860
93.50	Af+	28.1	455.264	157.995	53.663	28.365	3.380
91.75	Af+	26.4	431.869	161.341	51.192	28.755	3.410
				mean values =	55.142	28.947	3.550
102.25	Af+	36.9	516.538	220.458	55.835	28.510	3.190
103.90	Af+	38.5	509.301	250.578	57.088	28.209	3.170
103.25	Af+	37.9	514.590	262.639	54.177	28.441	3.020
				mean values =	55.700	28.387	3.127

Table 4.4 - Summary of all the tests on wire1.2TT0

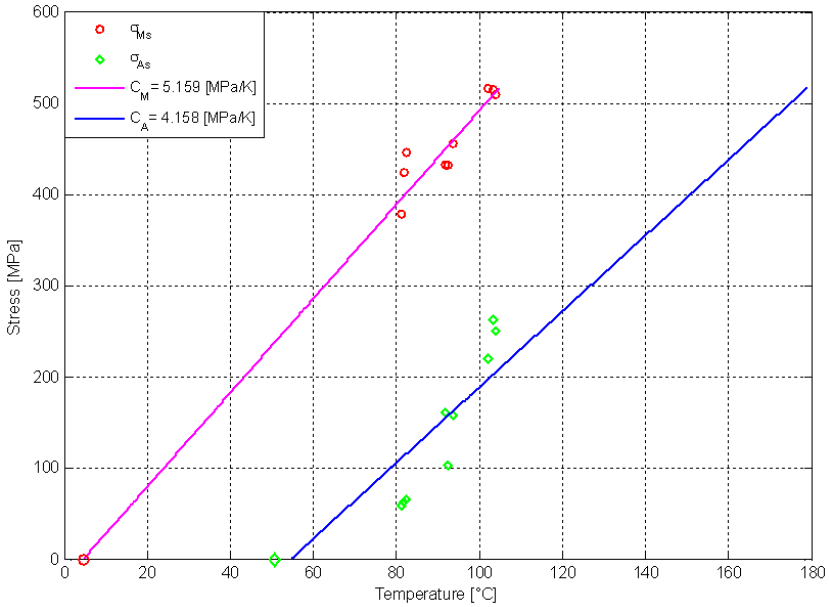

Figure 4.20 - wire1.2TT0, Experimentally Derived Phase Diagram

M_S	4.7 (277.85)	°C (K)
M_F	-20.5 (252.65)	°C (K)
A_S	50.7 (323.85)	°C (K)
A_F	65.4 (338.55)	°C (K)
E_A	60.444	Gpa
E_M	30.340	GPa
H	3.672	%
C_M	5.159	MPa/K
C_A	4.158	MPa/K

Table 4.5 - Summary of average parameters for Wire1.2TT0

4.5.2 Material 3: Strip 4x0.5 mm Thermal Treatment 2

The material chosen for the analysis is a strip, obtained by lamination, width of 4 mm and thickness 0.5 mm.

The material was available as cold worked, then have been performed some testing both in its original condition, and after two heat treatments. In its original state the material is stronger, but presents a hysteresis very small and, above all, does not allows observing the characteristic behavior of the martensitic transformation. The first heat treatment at higher temperature (450°C 30') makes it closer to the annealed condition, producing a softer material, which shows a higher hysteresis and an unloading plateau at low values of stress, with a significant residual deformation. With the intermediate heat treatment (350°C 30') there is a reduction of the recoverable strain field and a lower area of hysteresis, but the flag shape characteristic of these materials is tightly closed, with a very small residual strain.

The comparison between the three behaviors can be found in Figure 8.

Both tests are conducted at a temperature higher than A_F, thereby providing pseudo-elastic conditions. Already from these graphs, it is known the ability to stretch up to very high rates of strain, in this case 5-7%

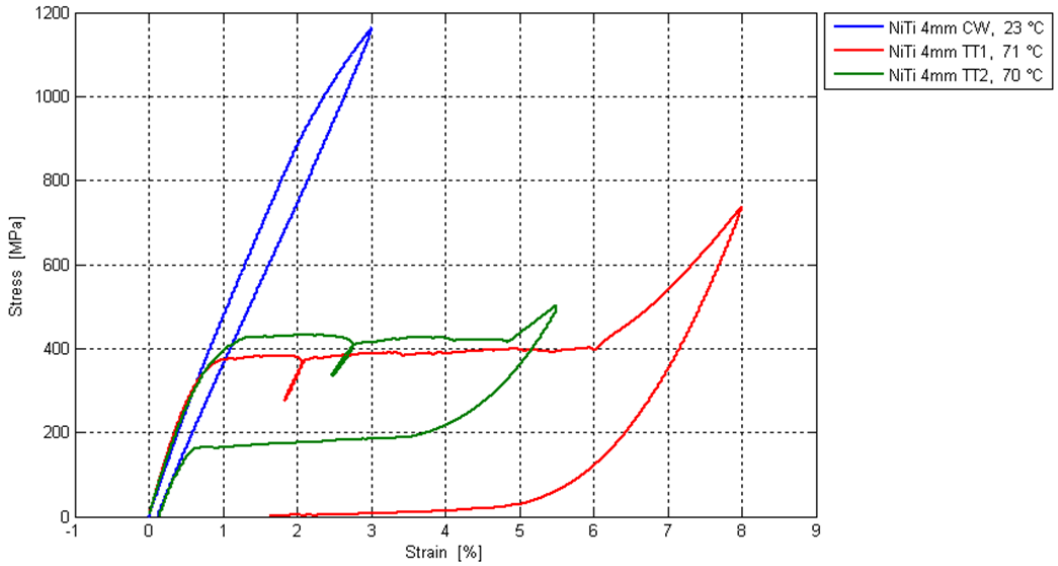

Figure 4.21 - Comparison between tensile tests for three heat treatments

Below is reported the analysis made to state the material in the condition of the second heat treatment (in green in the previous graph).

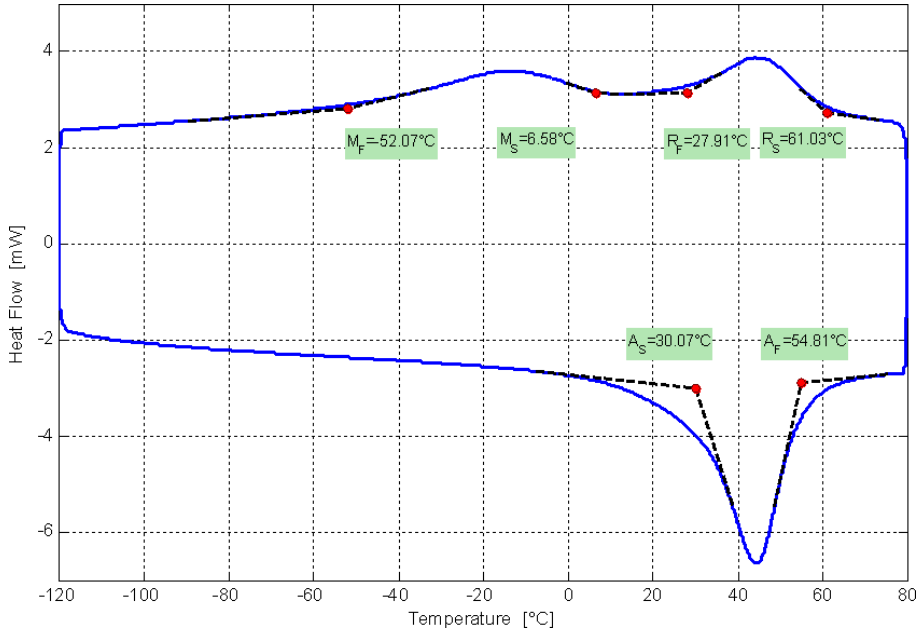

Figure 4.22 - Strip4x0.5TT2, DSC

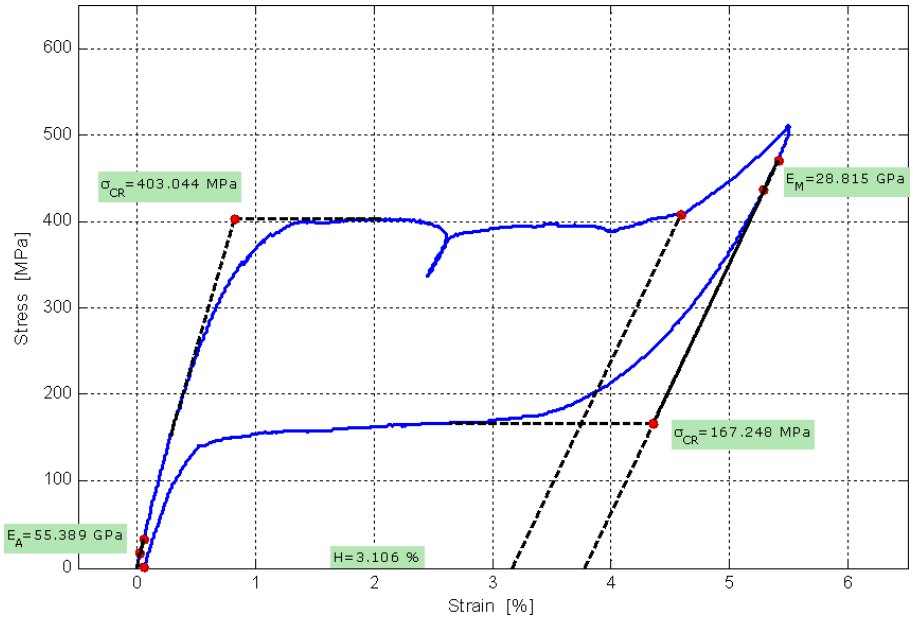

Figure 4.23 - Strip4x0.5TT2, MTS Tensile test

For the meaning of the various parameters, see comments below Figure 4.19, page 62.

One way to improve the accuracy of this parameter is to carry out many tests in traction at different temperatures and then perform an interpolation of all the values obtained as done for the wire in Figure 4.20.

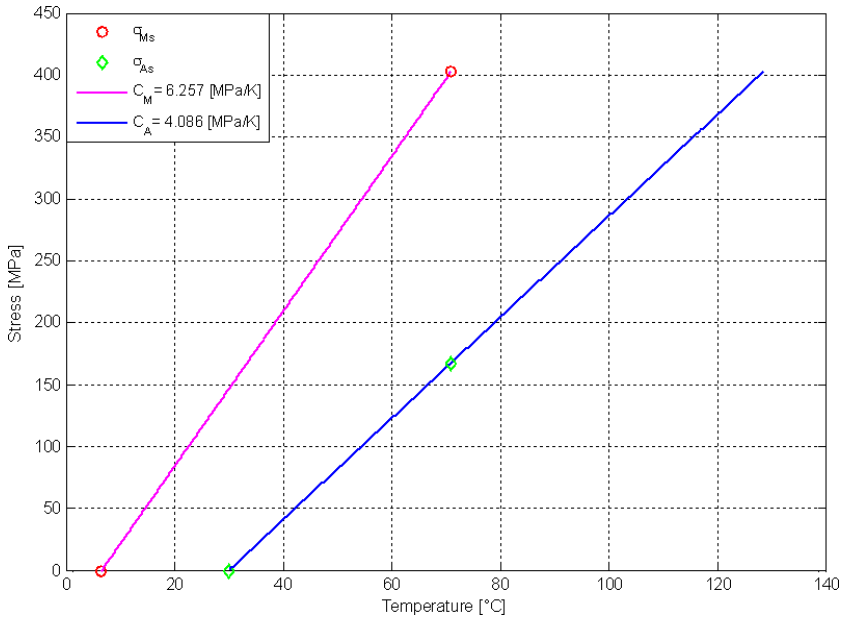

Figure 4.24 - Strip4x0.5TT2, Experimentally Derived Phase Diagram

For this wire tests in frequency were also carried out to evaluate the damping properties. Referring to the transformation temperatures, shown in Figure 4.22 page 65, the phases that have been studied are:

- fully austenitic, +80°C
- fully martensitic, -60°C
- during the martensitic transformation, -15°C
- between the phases martensitic and rhombohedral, +25 ° C

Multiple scans have been carried on two frequency ranges: from 1 to 36 Hz and then from 36 to 72 Hz, while setting a fixed maximum strain of 0.1%.

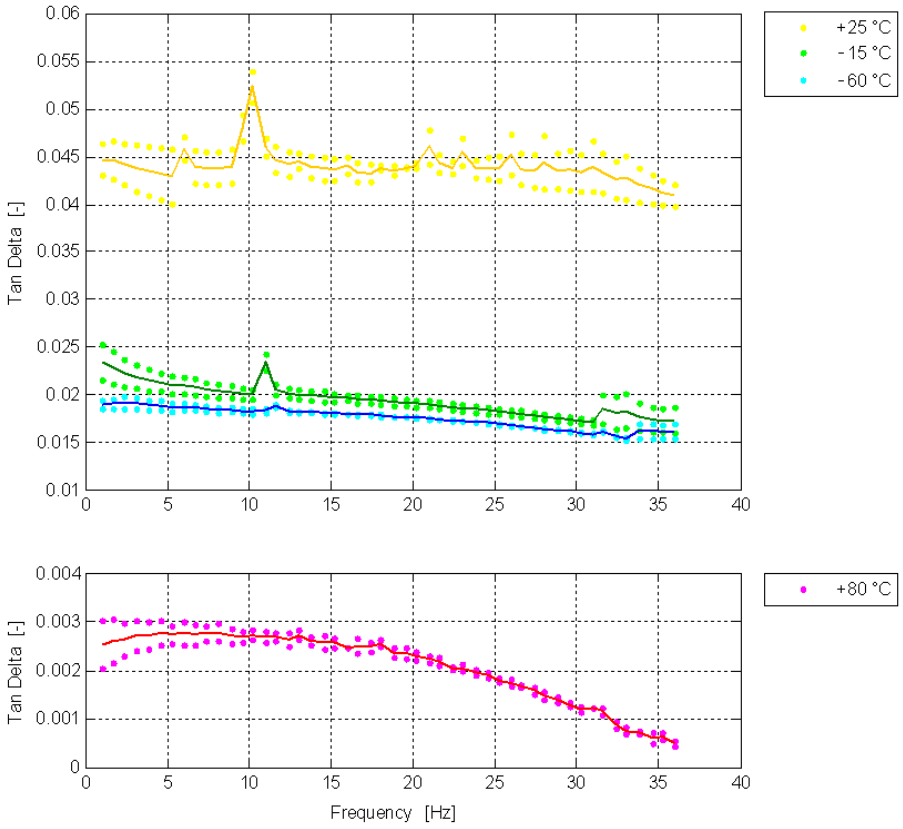

Figure 4.25 -NiTi Strip4x0.5TT2, dynamic scan freq. 1-36 Hz

The first thing to notice is that in the case of NiTi systems, the tan(δ) of martensite and rhombohedral is an order of magnitude higher than austenite: respectively 0.04 and 0.02, compared to 0.002. The phase with higher damping behavior is the rhombohedral one, while there is no much difference between the behavior of the fully martensite phase and during transformation.

The reasons for this behavior (for which also refers to the chapter 1.3.3) are related to the presence of twin boundaries in martensite phase, which absorb energy absenting,

and to the particular form "stretched" of the rhombohedral crystalline structure; in the austenitic cubic phase the only mechanism of absorption is that of the hysteresis of pseudoelastic cycle, which is small for these values of strain and then determines small values of damping.

In addition to having a greater absorption in general, NiTi systems also present localized peaks. It is recalled that a peak of tan(δ) identifies a peak phase shift and then a maximum power dissipation. The most interesting peculiarity is that the alloy can be modulated much in the microstructure and consequently in the height and position of these peaks and in any case has multiple frequencies of absorption and therefore a better overall reduction of the vibrations at low frequencies.

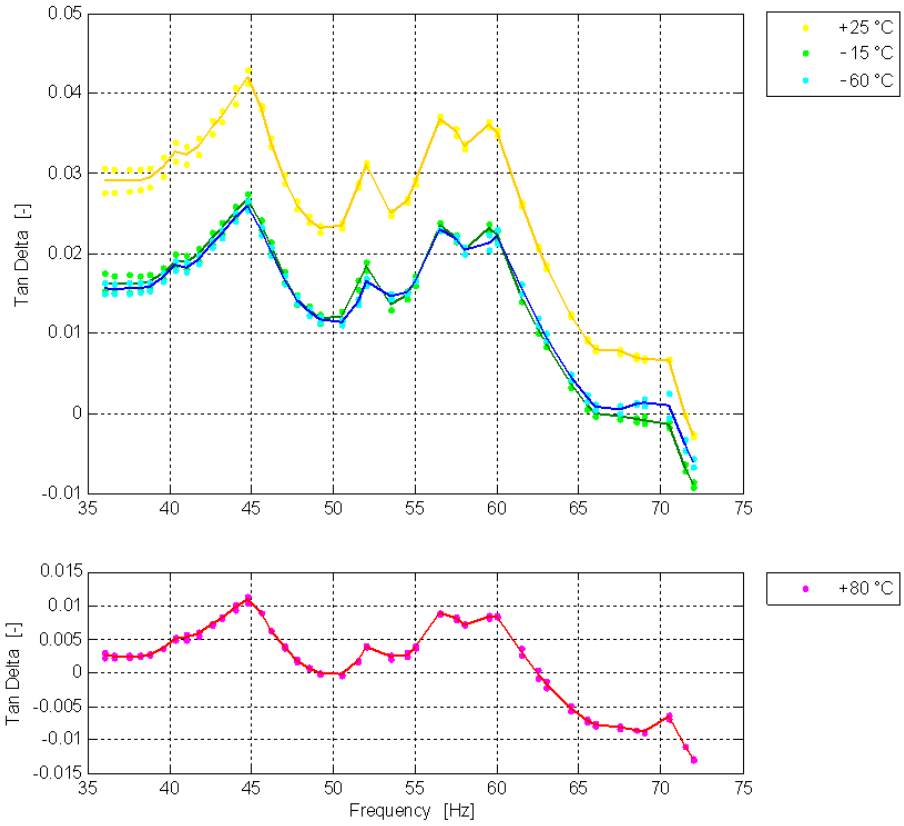

Figure 4.26 - Strip4x0.5TT2, dynamic scan freq. 36-72 Hz

Going to the next range of frequencies, the mean values remain at levels comparable to the previous ones, but the response is far less clean. This may be due to interactions with the natural frequencies of the clamp of the instrument. Furthermore, towards the end of the scan, features some negative values of tan(δ). This is produced by the fact that the sample responds in an anomalous way, retorting and then giving a force to the shaft. Obviously these values are to be entirely ignored because they do not represent a physically correct answer.

M_S	6.58 (279.73)	°C (K)
M_F	-52.07 (221.08)	°C (K)
A_S	30.07 (303.22)	°C (K)
A_F	54.81 (327.96)	°C (K)
E_A	55.389	GPa
E_M	28.815	GPa
σ_{Ms}	403.044	MPa
σ_{As}	167.248	MPa
H	3.106	%
C_M	6.257	MPa/K
C_A	4.086	MPa/K

Table 4.6 - Summary of average parameters for Strip4x05TT2

5 Numerical vs. Experimental Comparison

5.1 Introduction

This chapter is the point of union of the previous two, i.e. the experimental characterization and the analysis of the sensitivity of the model of Lagoudas to its parameters. In fact, are used the parameters obtained from experimental tests, to try to reproduce the testing itself. This procedure was done in different ways, which will be described in detail at the specific case.

The material used for comparison are the same studied in Section 4.4 at page 54.

5.2 Material 1: Wire 0.3 mm

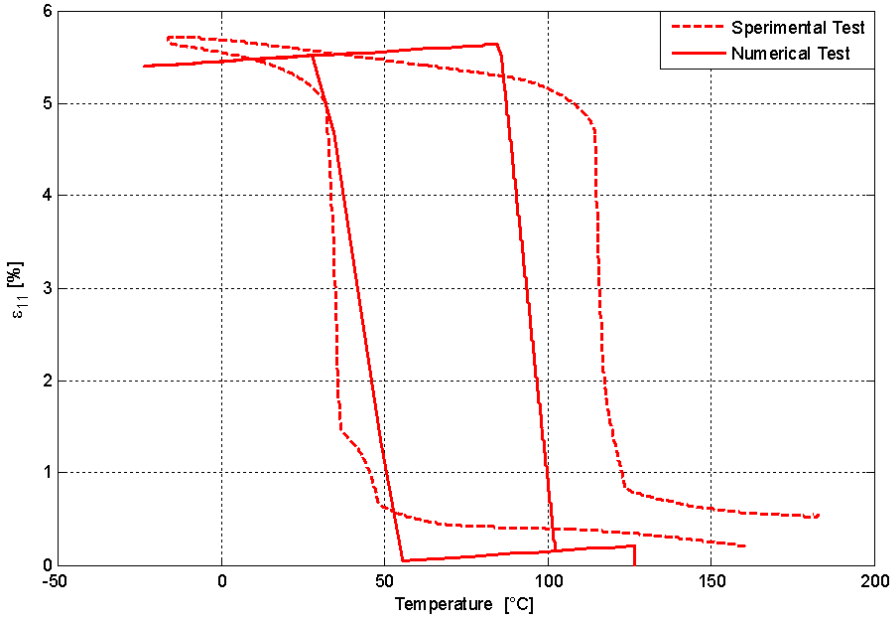

Figure 5.1 - Wire 0.3 mm, Tensile Strain Recovery Test

The first comparison investigated is test strain recovery on the thinner wire. The stress value is constant (in this case 100 MPa) and is set a cycle in temperature. The result is rather good, with some imprecision. For example that the sections at approximately constant strain have opposite slopes and the area of hysteresis of the numerical test is narrower than that of the experimental.

Furthermore, the portions that should be flat, that is at constant strain, instead have opposing gradients. This is because the model of Lagoudas considers the material with elastic modulus constant and there subtracts the effect of the decrease in temperature, instead the memory material real form, as the temperature changes varies its properties.

5.3 Material 2: Wire 1.2 mm

Figure 5.2 and Figure 5.3 display the curves obtained using the parameters extrapolated from a single experiment, a traction at 81°C (~A_F+15°C), to reproduce the test itself and a second one in which only changes the test temperature. In the first of two, the behavior is very good, almost perfectly reproducing the trend. In the second, at a temperature ~A_F+25°C, the experiment highlights the increase in slope of the plateau due to the increase in temperature, while the numerical test keeps the same inclination. In fact, as already mentioned in Chapter Figure 3.3 at page 35, the increase in test temperature produces the rise of the curve, but does not change the inclination of the plateau.

Note that the numerical test reproduces never the residual strain, but always closes, returning to the starting point.

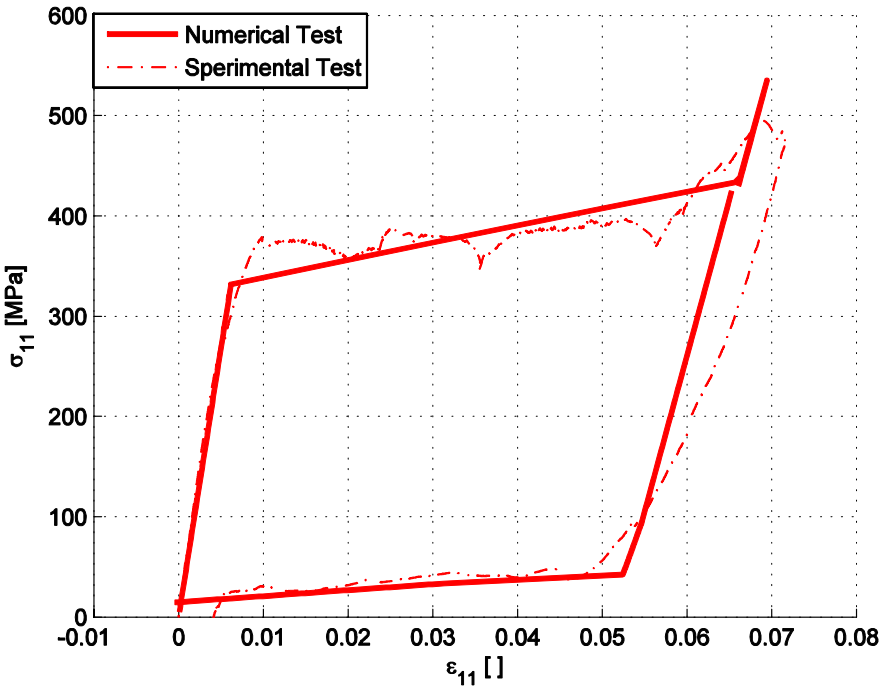

Figure 5.2 - Wire 1.2 mm, Tensile Test at 81°C, Approximated

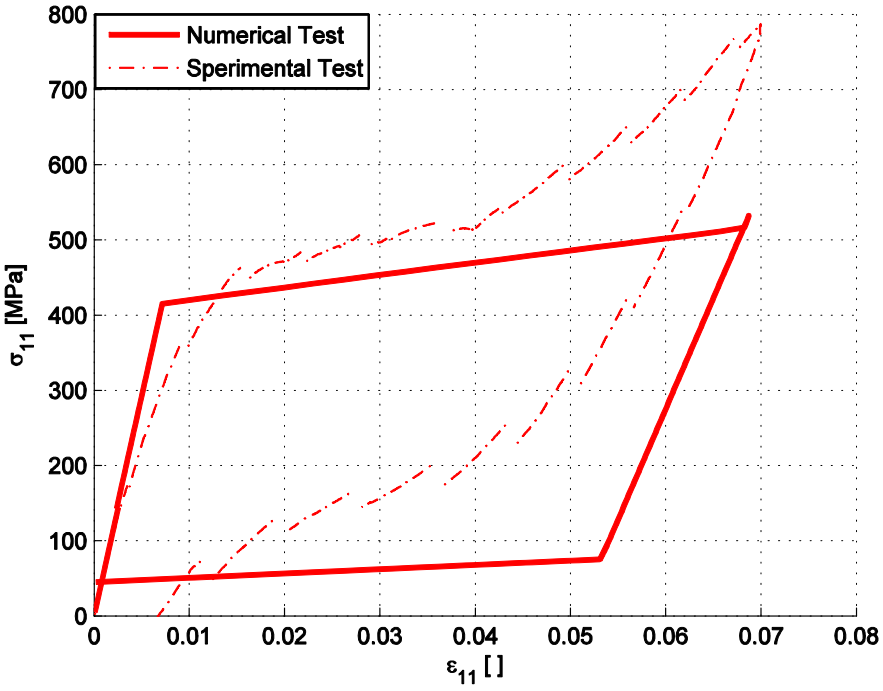

Figure 5.3 - Wire 1.2 mm, Tensile Test at 103°C, Approximated

To try to make the simulation independent from single test, were tried parameters averaged over all those effectuated. The results are in subsequent images, Figure 5.4 and Figure 5.5. As can be seen, the outcome is much less satisfactory. This leads to the conclusion that the simulation through Lagoudas is reliable if you want to model a single test, or materials with behavior very stable and constant, but becomes less effective if you need to represent the generic behavior of an alloy, releasing it from any contingent test condition.

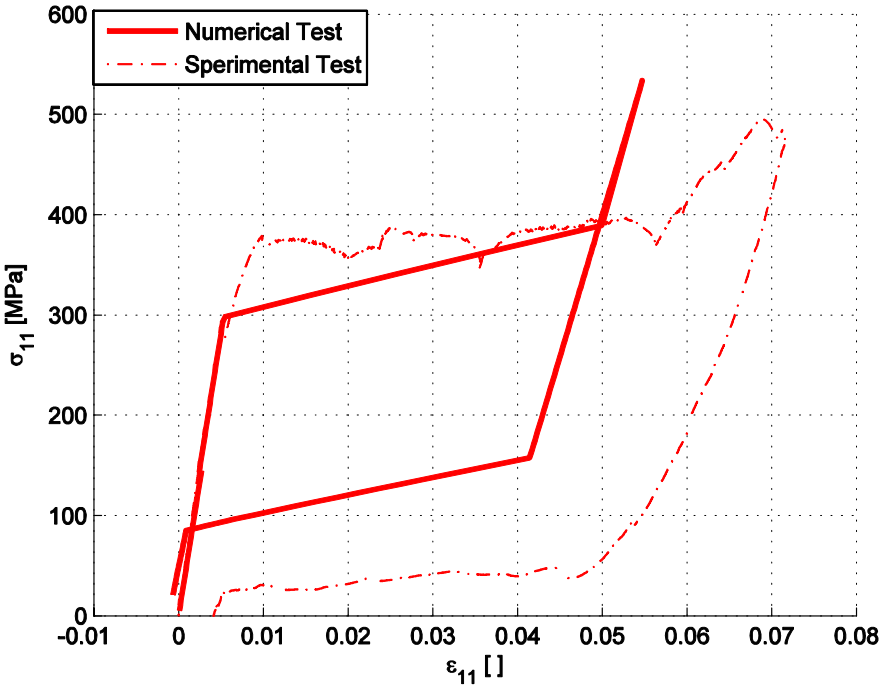

Figure 5.4 - Wire 1.2 mm, Tensile Test at 81°C, Interpolated

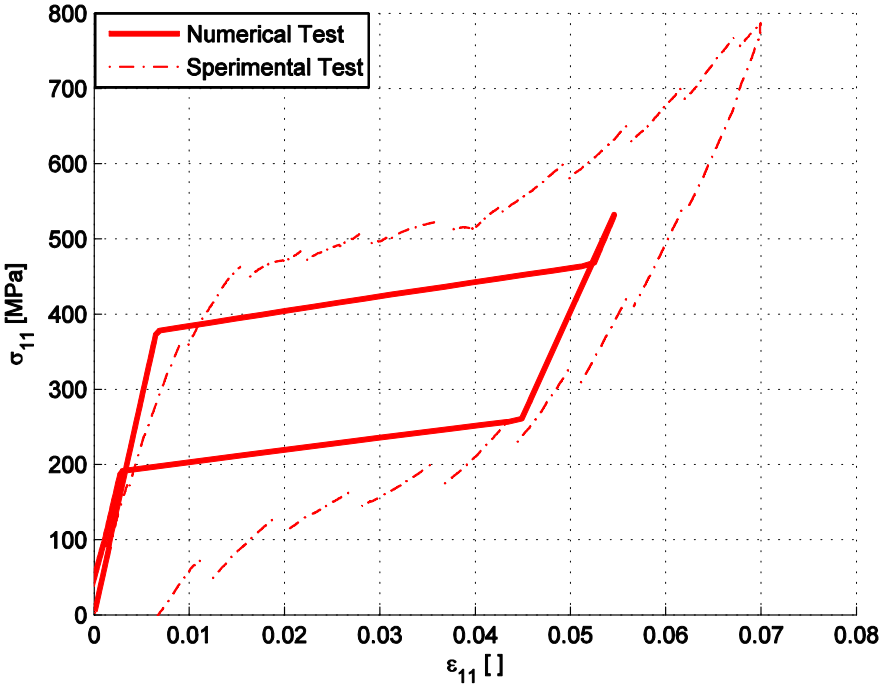

Figure 5.5 - Wire 1.2 mm, Tensile Test at 103°C, Interpolated

5.4 Material 3: Strip 4x0.5 mm

The last material compared is the strip, of which there is the single test in traction.

As mentioned in the previous paragraph one might expect that the numerical test follows quite well the real one, instead it is not so. In this case however it is permissible to justify the imprecision with the type of specimen: in fact, not only a strip presents an intrinsic strong geometric anisotropy, but also a texture within the material due to rolling, not representable by the elements of the FEM that instead have properties perfectly homogeneous.

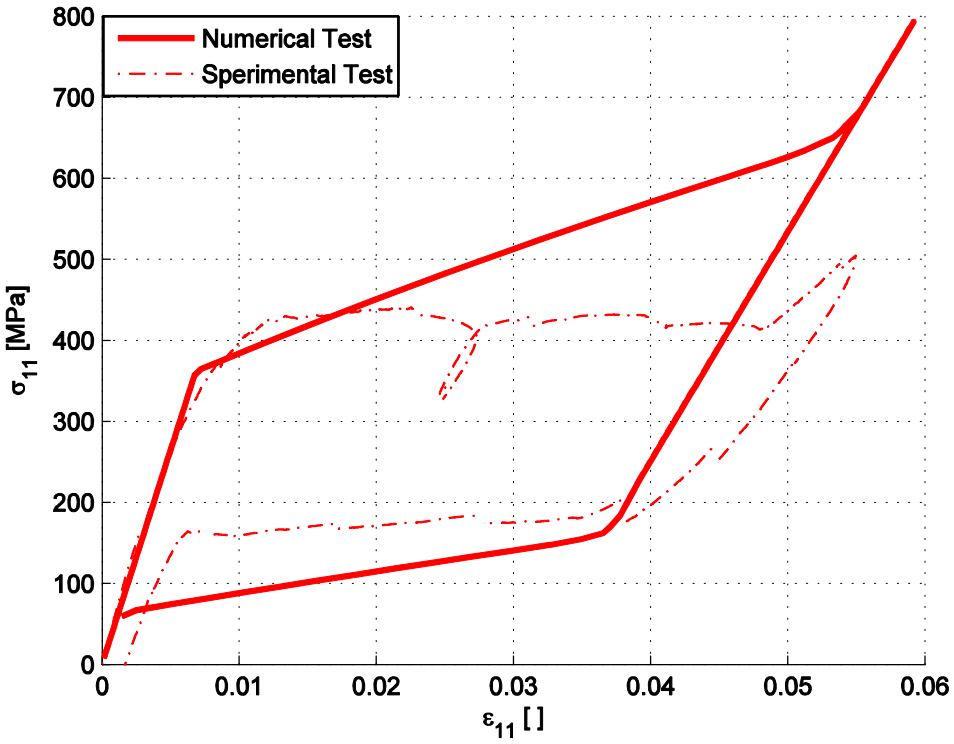

Figure 5.6 - Strip 4x0.5 mm, Tensile Test, Approximated

6 Technical demonstrator of a simple application

6.1 Underlying Concept

The demonstrator is intended to validate the numerical finite elements model with regard to the ground-based part of the application. In this context, the shape memory material comes into play in the fact of being able to withstand strain levels greater than steel, while maintaining its performance where the steel is deformed plastically and thus relieving the glass of the stress that would be induced on it.

The simple application realized through this demonstrator consists of a simplified optomechanical mounting, in which an optical glass plate (a dummy optical/mirror) is fixed to a plastic basement plate via four metallic blades. According with the purpose of comparing a NiTi alloy with a material traditional used for mounting, both Steel and NiTi have been considered for the flexures. The optomechanical design goal is to reduce stress on mirror and preserve the geometrical constrain.

In the ground-based application, the forces that affect the glass are the gravity and tension induced by the mismatching in thermal expansion coefficients between glass and plastic. Subjecting the demonstrator to a temperature gradient, the base expands more of the glass, so loads it with a stress through the bending of supports.

The ideal goal would be the application of mounting at large devices, but, for practical reasons, only a demonstrator on a small scale could be tested. So it is necessary to find a way to induce on it loads that allow us to analyze the peculiar properties of SMA materials. This aim has been achieved with two means. The first one

is a pre-load obtained with a base larger in size than the glass plate, and produced with a material provided with a greater coefficient of thermal expansion. The second one is using flexures with non constant thickness and two “bottlenecks” to concentrate stress in a hinges-like configuration.

6.2 Loads and geometrical sizing

Assuming also a possible use of this same system for space, the sizing of the flexures has been done setting as a critical dimensioning condition the acceleration provided by data sheet for launches of optics. The load used is the mass of mirror multiplied for a factor $n = 60$. The demonstrator configuration foreseen the use of four flexure, so the critical load must be divided equally on them.

The length of strip was sized with Eulerian instability:

$$\qquad\qquad$$

where L_0 is the free bending length, E the modulus of elasticity, I the area moment of inertia. The factor k relates the true geometrical length L with L_0 end it depends from the type of constrain. In this case it is assumed to be four, because of the following constrain condition:

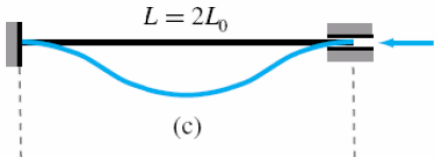

The area of inertia is calculated with the minimum thickness value of 0.2 *mm* both the supports configuration. With the property of Steel and NiTi it can be calculated the max length available. The model is design to work in austenitic phase (pseudoelastic effect), so for NiTi is used the Young's modulus of austenite.

$$\qquad\qquad$$

The dimension of mirror and of its weight are not critical to our model. The choice of the size depends only on the availability of stuff and simplifications of the assembly and test. The final length used is 40*mm* with 10 *mm* that are the total area of bonding.

The numerical test analyzes a thermal load supposed critical in Ground Base. The different CTEs are caused of differential displacement that case a mechanical loading on mirror. The stresses caused by this and the deformation of flexure are the focus for comparison the performance of NiTi.

6.3 Mirror and Basement description

The optical glass consists of a square plate, thickness 5 mm and lateral dimentions 100x100 mm. It has been received directly by the supplier with the size and the properties we required. The properties of the material are:

Opal diffusing Glass - Mirror:

- Density_____2.20 g/cm^3 = 2200 kg/m^3
- E_tensile_____73 GPa
- T_max_____1000°C
- CTE_____5.5E-7 1/K

The basement also has a square shape. The thickness is 10 mm and the lateral dimensions are 102x102 mm, in order to obtain the preload, which it is referred in Section 6.1. This component has been cut from a nylon plate of 500x600 mm. Its properties are:

Nylon natural, fused - Basement:

- Density_____1.14 $g/(cm^{3})$ = 1140 $kg/(m^{3})$
- E_tensile_____3300 MPa = 3.3 GPa
- T_max_____165°C
- CTE_____7E-5 K^{-1}

6.4 Experimental Characterization of supports material

For this application has been chosen a material close enough to the annealed condition. This is because in any case it is not expected to achieve high deformation so are not to be feared residual strain. In return, the alloy will be smoother. Furthermore has been chosen an alloy that is pseudoelastic at room temperature, so that absorbs the bending deformation induced by the greater expansion of the base.

The characterization was performed for strips made by electro-erosion from a semi-finished hot rolled. It has been carried out both for a “standard” strip with regular thickness and for the waisted strip which will then be mounted on the demonstrator.

First, the transformation temperatures are obtained from DSC. Being the same alloy, this applies to both strip types.

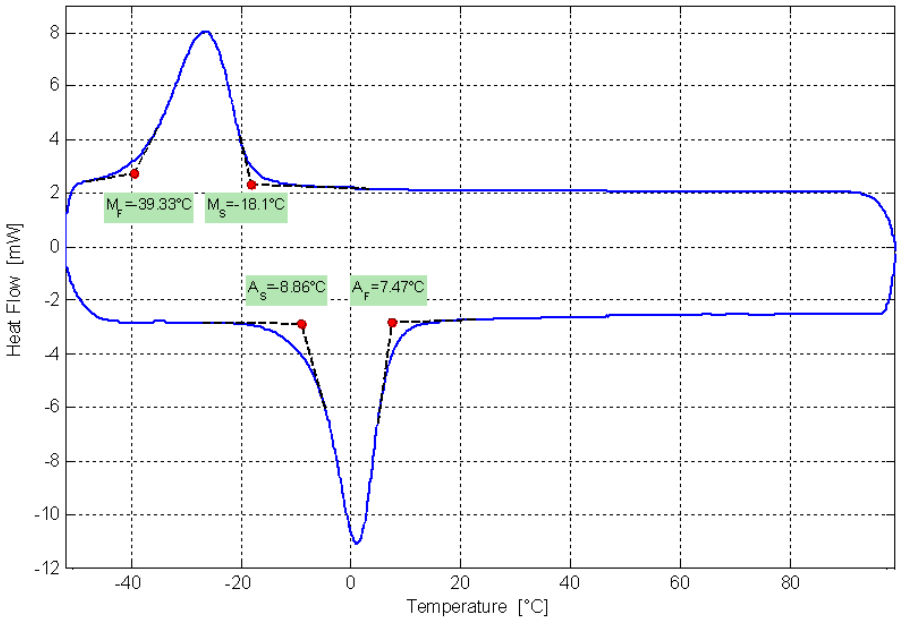

Figure 6.1 - Supports Material, DSC

As can be seen, the temperature A_F is about 7 degrees Celsius, respecting the requirement of pseudo-elastic at room temperature.

6.4.1 Standard for supports: rectangular, non waisted strip

The dimensions of the sample produced are:

- length = 17.5 mm
- width = 5 mm
- thickness = 1 mm

Due to the size, we opted for an analysis in bending via DMA. The applied method consists of five cycles, each of which first stabilizes the sample at a certain temperature (-50, 10, 15, 20, 25°C), and then performs a sequence of loading and unloading up to the maximum force attainable by the DMA and back to zero. After each cycle is performed a recovery of the alloy at 70°C.

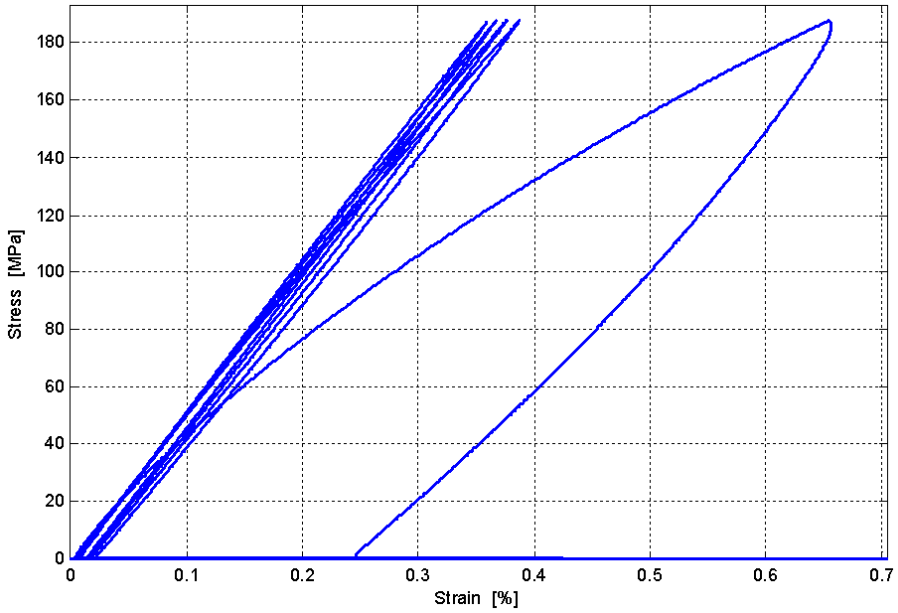

Figure 6.2 - Standard for support material, DMA bending complete cycle

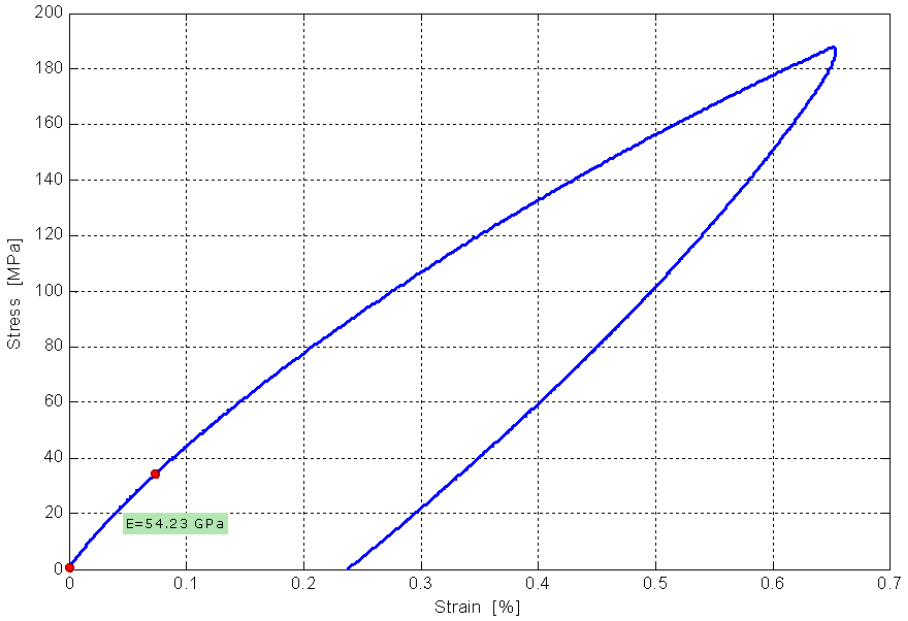

Figure 6.3 - Standard for support material, DMA bending in Martensite

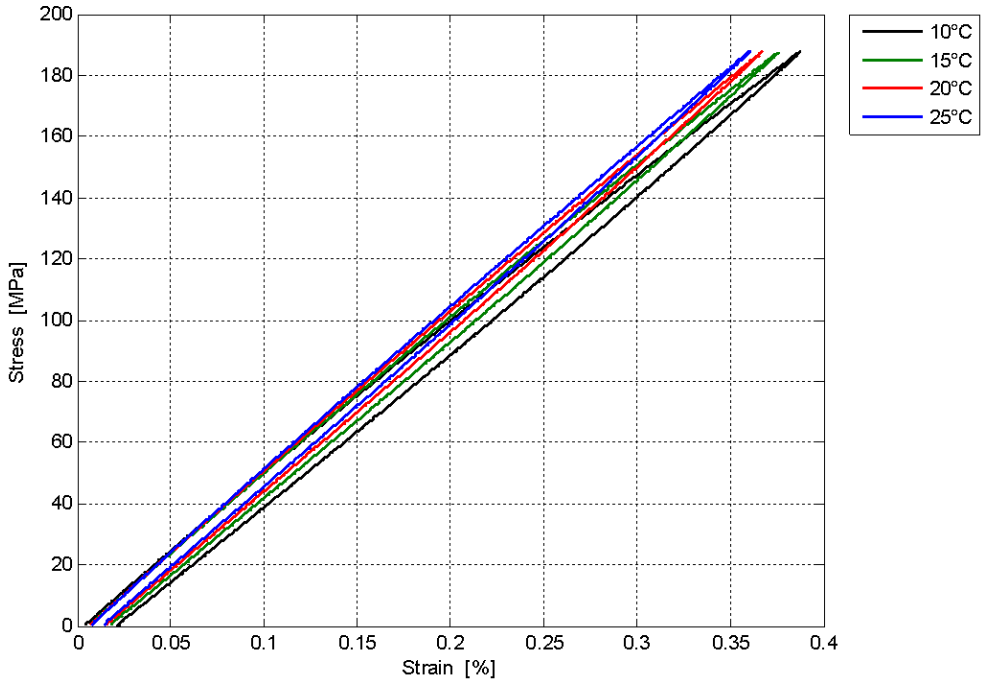

Figure 6.4 - Standard for support material, DMA bending in Austenite

For the single test in martensite and each test in the austenitic phase, the elastic modulus (E) was calculated using the formula provided with the instrument:

$$E = \frac{K_s}{F_c}\frac{L^3}{12J}\left[1 + \frac{12}{5}(1+\nu)\left(\frac{t}{L}\right)^2\right]$$

$$F_C = 0.7616 - 0.02713\sqrt{\frac{L}{t}} + 0.1083\ln\left(\frac{L}{t}\right)$$

Where K_S is the stiffness detected by DMA, L is the length (constant in the case of bending and equal to 17.5 mm, i.e. the distance between the holders of the clamp) and t is the thickness.

Temperature [°C]	-50	10	15	20	25
E [GPa]	54.230	52.655	54.208	54.947	56.179

Table 6.1 - Elastic modulus of the supports material

Note that with this value of thickness, only the elastic range of austenite is used, without inducing transformation.

6.4.2 Supports: rectangular, waisted strip

The dimensions of the sample produced are:

- length = 17.5 mm
- width = 5 mm
- thickness =
  - 1.00 mm (comparison)
  - 0.40 mm (minimum)
  - 0.70 mm (average)
  - 0.49 mm (equivalent)

The thickness that actually works during the solicitation is initially undetermined, to be discriminated, therefore in the data requested by the instrument is arbitrarily inserted 1 mm thickness. So doing the actual geometric data do not coincide with those set at the beginning of the test, therefore all the values of variables that the instrument derives from them are to be recalculated. The only direct measures - and therefore not to change - are force (from the load cell) and displacement (from the optical encoder).

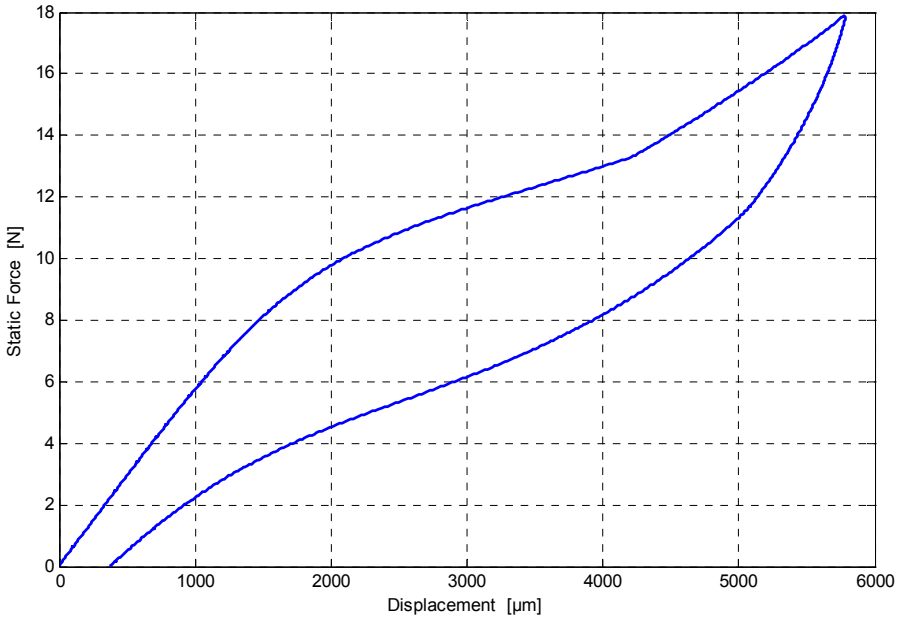

Figure 6.5 - Force vs. Displacement, waisted strip at 20°C

In this way the values obtainable in terms of stress and strain cannot be certain, however, it is possible to calculate a good estimation of them, which will serve to suggest values of first attempt for the model parameters of Lagoudas. To improve modeling will then be used the knowledge gained during the study of sensitivity to select the best parameters to represent the material.

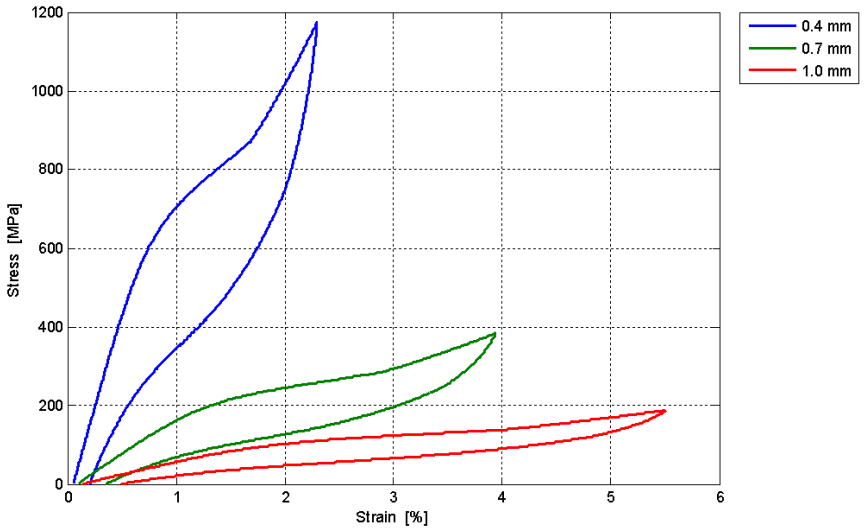

Figure 6.6 - Comparison between different thicknesses at 20°C

To derive this approximation an equivalent thickness is calculated: it is assumed that the elastic modulus should coincide with that of non-rectangular shaped specimen.

The model of the beam used to simulate the DMA clamping is:

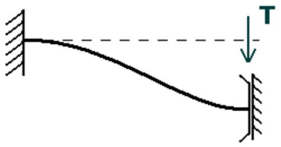

Hence, the PLV:

$$\int_0^L \delta w'' EJ w''(x)\, dx = \delta w(x = L) T$$

with boundary conditions:

$$\begin{cases} \delta w(x = 0) = 0 \\ \delta w'(x = 0) = 0 \end{cases} \quad (incastro)$$

$$\begin{cases} \delta w'(x = L) = 0 \\ EJ w'''(x = L) = -T \end{cases} \quad (pattino)$$

this dictates the elastic line:

$$EJ w(x) = -\frac{T}{6} x^3 + \frac{T}{4} L x^2$$

and the expression of stiffness:

$$K = \frac{12EJ}{L^3}$$

Known the stiffness measured by the DMA (as Force/Displacement) and fixed E (only in the first elastic portion) equal to that of the rectangular plate (55 GPa at 20°C), we obtain the inertia J and from it the thickness, which is about *0.49 mm*. With this value are recomputed strain and stress, then the elastic modulus.

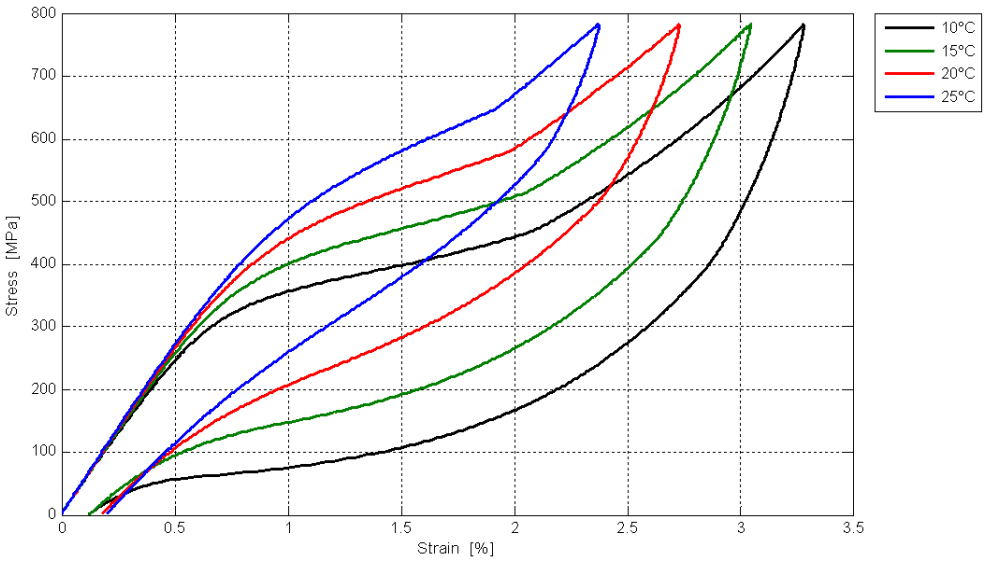

Figure 6.7 - Stress vs. Strain, waisted support, equivalent thickness (0.49 mm)

It should be noted that, compared to the standard strip, in this case, there is induction of martensite, reaching values of strain and stress higher.

Now that the correct values of the solicitation are available, it is possible to proceed with the computation of the parameters, as described in the pertinent chapter. Below is shown only the graph for 10°C temperature and the results are summarized in a table.

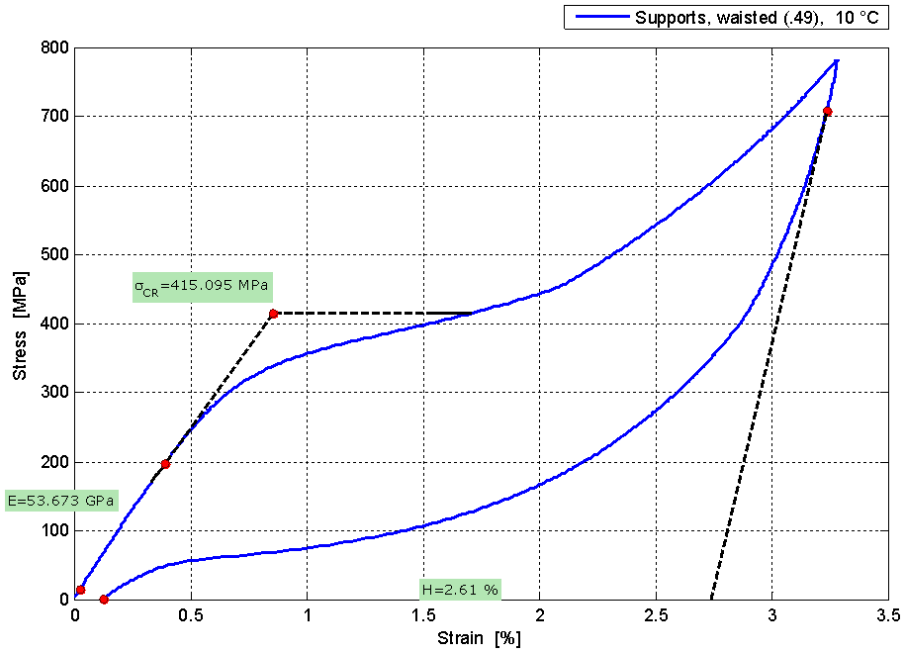

Figure 6.8 - Example of the parameters derived from graph

Temp. [°C]	E [GPa]	σ [MPa]	H [%]
10	53.673	415.095	2.61
15	54.842	471.067	2.33
20	55.471	531.705	1.89
25	56.325	594.263	1.43

Table 6.2 - Summary of parameters for supports material

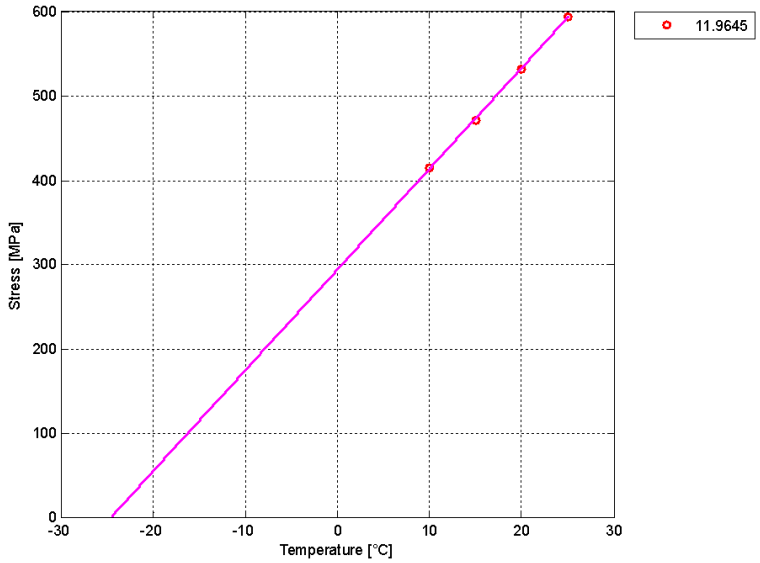

Figure 6.9 - Stress vs. Temperature rate

6.4.3 Damping Analysis

As regards the space-based part of the application, the idea is to use two properties of the SMAS: the ability to absorb vibrations and shape memory.

During the launch, in fact, one of the conditions mechanically more severe is vibrational stress. Major sources of vibration are at launch, with the acoustic noise that radiates from the engine and incorporates the entire vehicle, and when the vehicle crosses the transonic phase of its flight. The parts most affected by structural vibrations are those with an elevated area and a small mass. On the mountings of telescopes are commonly installed systems of vibration isolation, but the use of SMA material would further reduce the load on the optics, especially at low frequencies.

Reached the orbit, it is possible to prospect applying the shape memory, i.e. heating above A_F, to recover the original appearance of the mounting and to cancel any deformation due to load peaks in the launch.

Since it was not possible to make practical tests with the shaker, scans in frequency were performed. In the two different phases, austenite and martensite, and in single

cantilever configuration, that is the closest to the mounted condition of the demonstrator.

Series of scans were performed in two frequency ranges: 1-36 Hz and 36-72 Hz. The maximum strain of 0.1% is set.

It has also been subjected to the same scans a strip of harmonic steel as a comparison. In this case the set maximum strain is 0.05%.

Following are the results obtained.

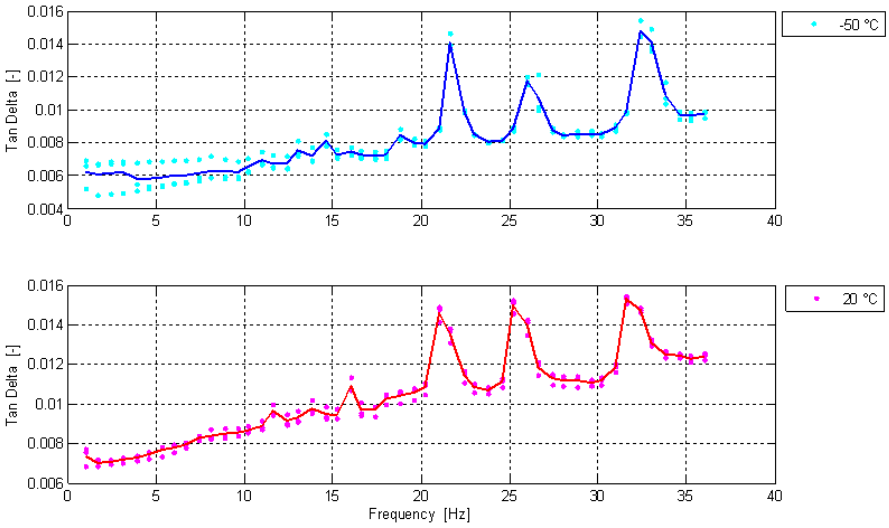

Figure 6.10 - Harmonic Steel, freq. 1-36 Hz

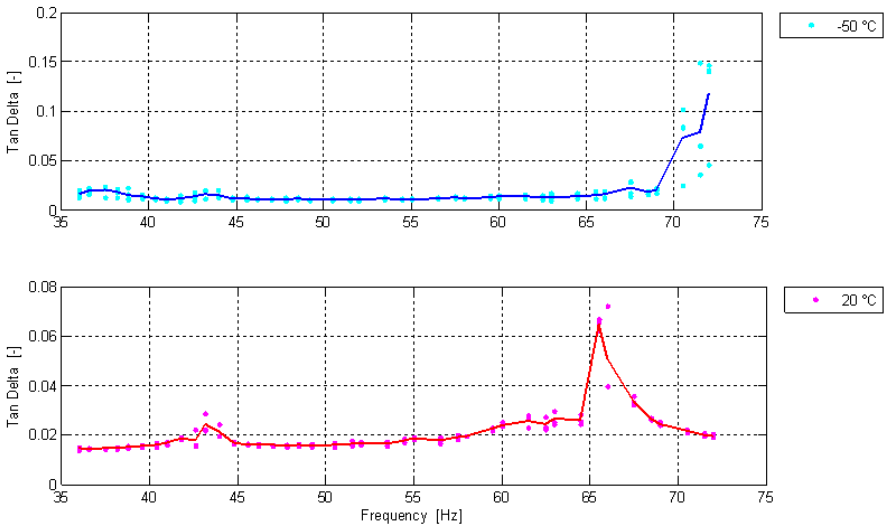

Figure 6.11 - Harmonic Steel, freq. 36-72 Hz

The harmonic steel has a level of tan(δ) independent of temperature, comprised between 0004 and 0.02. There are three peaks at 21, 26 and 32 Hz and one at 43 Hz. This is because the selected steel is of harmonic type; a generic steel would have had a lower and uniform absorption.

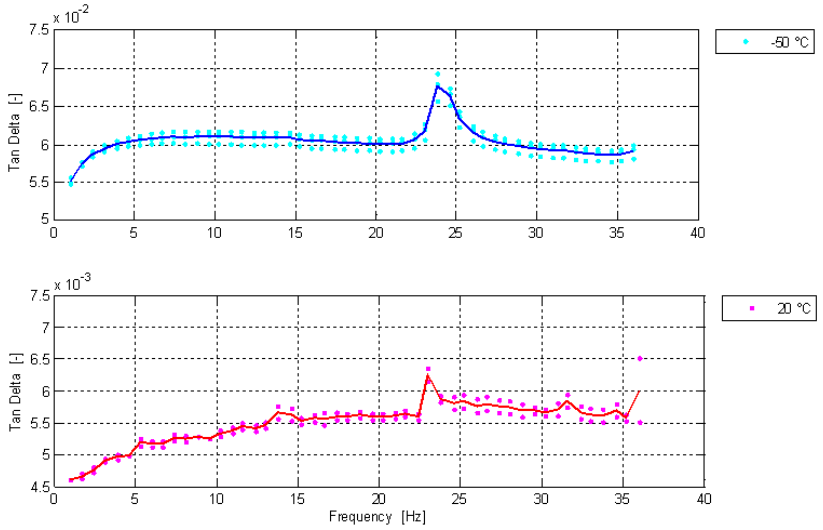

Figure 6.12 - NiTi Standard for supports, freq. 1-36 Hz

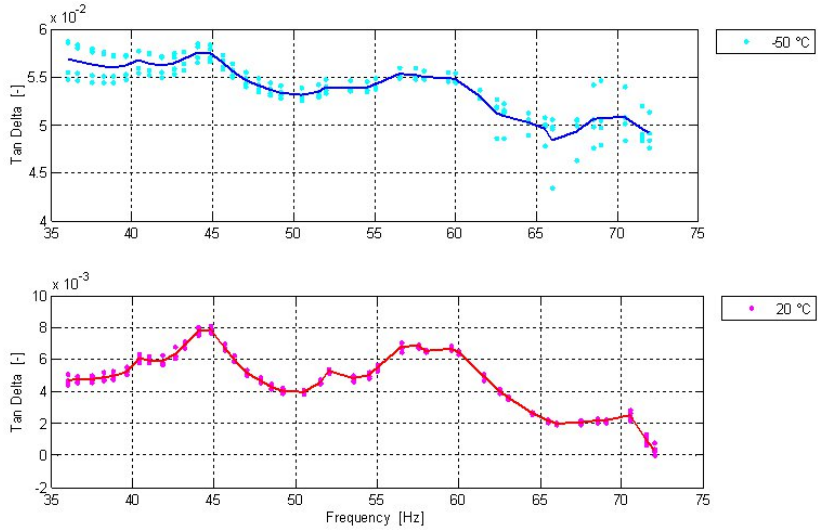

Figure 6.13 - NiTi Standard for supports, freq. 36-72 Hz

The first thing to notice is that in the case of NiTi, the tan(δ) of martensite is an order of magnitude higher than austenite: 0.06 compared to 0.005. In addition to having a greater absorption in general, NiTi systems also present localized peaks. It is recalled that a peak of tan(δ) identifies a peak phase shift and then a maximum power dissipation. The most interesting peculiarity is that the alloy can be modulated much in the microstructure and consequently in the height and position of these peaks and in any case has multiple frequencies of absorption and therefore a better overall reduction

of the vibrations at low frequencies. For example in this case there are some peaks at low frequencies and a peak at 41 Hz that were not present in the steel.

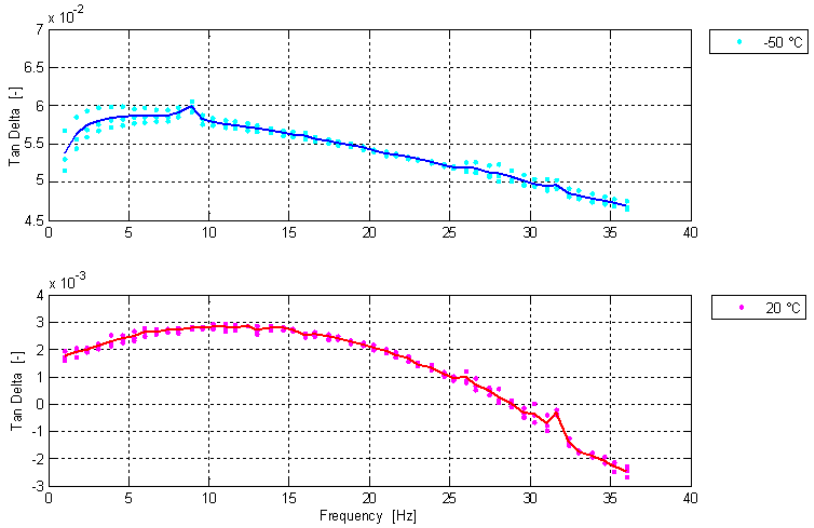

Figure 6.14 - NiTi Waisted supports, freq. 1-36 Hz

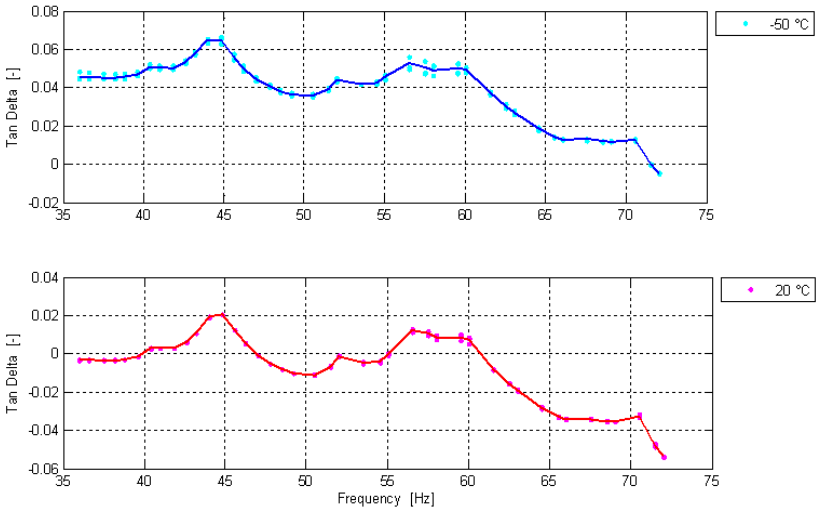

Figure 6.15 - NiTi Waisted supports, freq. 36-72 Hz

For the waisted supports is initially had a damping level comparable to the standard strips. In this case, however, the particular geometry ruins the test results, producing a significant lowering linked to an elastic return of the sample.

It is clear that this study is not sufficient to design a real space application. The purpose was to highlight that such capacity exists and is promising and widely exploitable. Will be needed deeper and more extensive campaign to better define this behavior in relation to vibrations on the satellite at launch with even a design of an alloy that meets the temperature conditions necessary for use in space.

6.5 Numerical Characterization of supports material

The material just presented constitutes the supports of the demonstrator, and its properties are used in the numerical model that will be developed for comparison and evaluation of the forces acting on the glass.

In the previous chapter has been discussed the problem of measurements made at the DMA and the fact that, since the geometry is so particular, the only certain data available are the force and displacement. This leads to having to introduce the use of a model which considers a geometry at constant equivalent thickness, used to derive stress and deformation by means of appropriate formulas, using as a starting point the elastic modulus in austenitic phase.

This has led to the use of a model of the flexure with an equivalent thickness equal to 0.49 mm, which has allowed to obtain a trend of stress and deformation, that the strip would have if it were with constant section. With these graphs has been achieved a first estimate of the possible parameters to be used for the implementation of Lagoudas. Using them as values of first attempt, the working path has proceeded with the iteration of the numerical models to obtain a trend of force vs. displacement as similar as possible to the experimental one.

The starting model for this iterative process has been a strip with the geometrical characteristics of the equivalent model on which we have simulated the bending test: length 17.5 mm, width 5 mm and a thickness 0:49 mm.

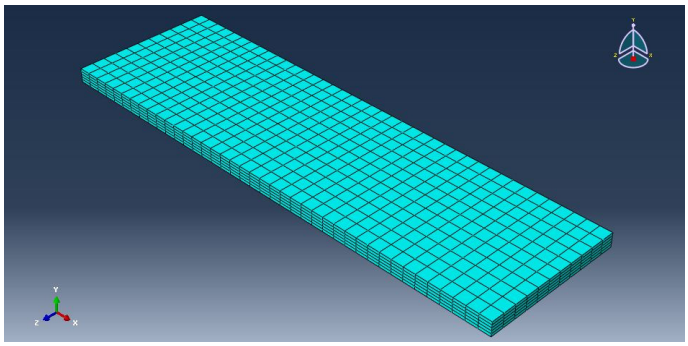

Figure 6.16 - Mesh of the first equivalent model

The simulation of the test with the DMA involves this set of conditions: hinge on one of the short sides of the foil, a sliding block on the upper and lower edges of the opposite side and, always on this, a displacement equal to that imposed by the DMA.

The parameters used for the Lagoudas sub routine have been evaluated in an iterative manner by exploiting the sensitivity process:

E_A=55 GPa; E_M=48 GPa; C_A=5.47 MPa/K; C_M=8 MPa/K; H=1.9%

The results obtained have led to the trend force vs. displacement reported in Figure 6.17 which discretizes in very good way the experimental one. The analysis during the unloading phase has been unable to reach convergence and thus the curve is not closed.

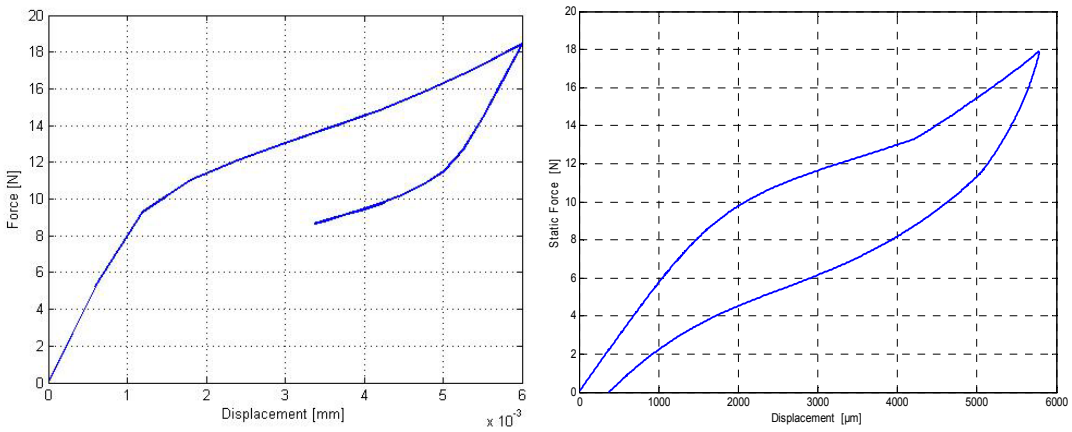

Figure 6.17 - Comparison between numerical (left) and experimental (right)

Once shown that the model works, the next step was to try to implement a model for the discretization of the strip shaped with the true geometry. The first approximation made was to simplify the hinge with a trapezoidal trend.

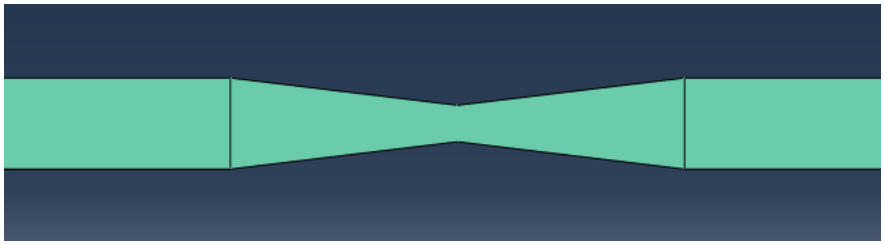

Figure 6.18 - Geometry trapezoidal to represent the support shape

Made the mesh and applied the same conditions of the previous case, the analysis was performed with the displacements imposed. Also in this case, during the unloading phase the model is not able to close the hysteresis loop. The result is, however, of the same quality of the previous one.

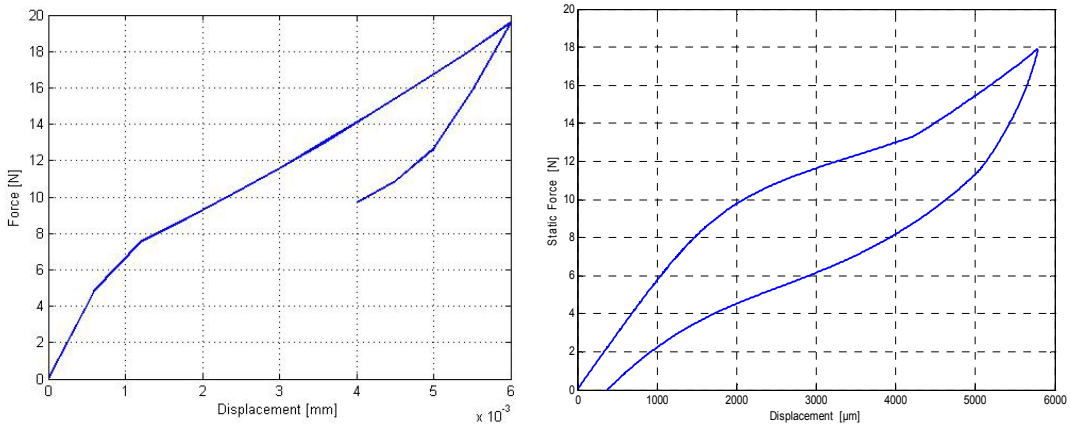

Figure 6.19 - Comparison between numerical (left) and experimental (right)

The last step was the attempt to model the actual geometry of the curved hinge and check the results. Since no convergence was achieved, using the parameters which have been verified to represent well the model, a further iterative process has been attempted. Despite this, the model does not work and it is not able to adequately represent the experimental behavior.

Therefore the model that has been chosen as validating is the one with the trapezoidal shape which respects the experimental behavior. The problem with this choice is that the stresses are focused on the central edge of the hinge, so if it is wished to get an idea of the maximum forces acting on the flexure, it is more convenient to go checking loads in surrounding areas.

6.6 Mounting Tools

In order to hold the assembly during mounting and transport, has been designed and implemented a mounting tool.

It consists of a four columns, with two notches on each of them, in which are to be inserted the angles of mirrors and basement. Realizing the notches with sufficient precision, both in terms of depth and positioning on the height of the column, it is possible to ensure a centered installation, and the parallelism between the surfaces of mirrors and basement.

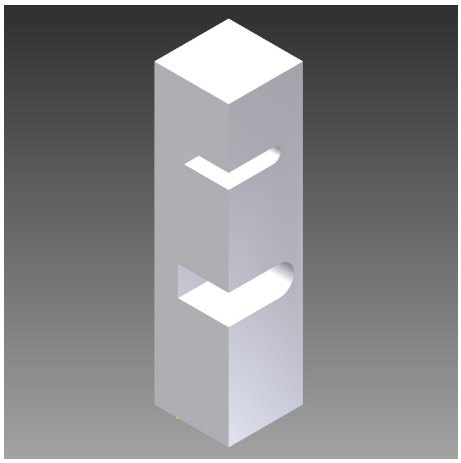

Figure 6.20 - Column, CAD model

To guarantee stability to the assembly, the columns are then screwed onto a further basis, provided with four indentations at the corners to fix the columns stable and straight and to prevent rotation.

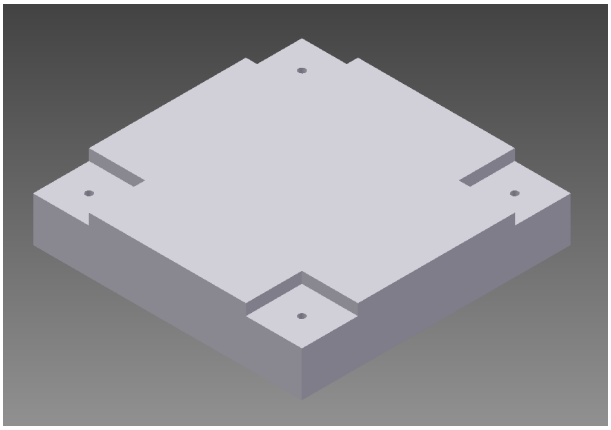

Figure 6.21 - Basement for columns, CAD model

The mounting tool is completed by a template, with the aim of pasting the supports vertical and centered in both width and height, and also can do so in a repeatable manner for each of the four sides. It has one groove where to put the NiTi strip, and a ladder to reach and to lean against the nylon, making slight pressure.

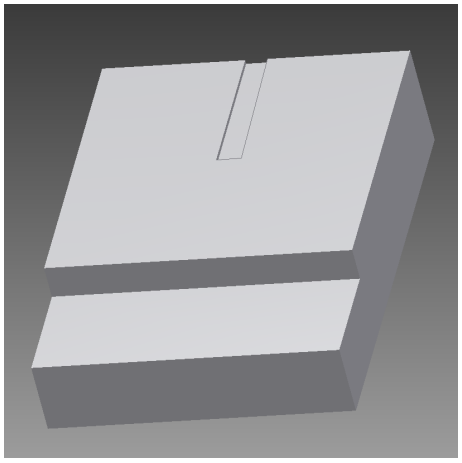

Figure 6.22 - Template, CAD model

Each part of the tool is produced from a plate semifinished in Delrin, with thickness 26.6 mm.

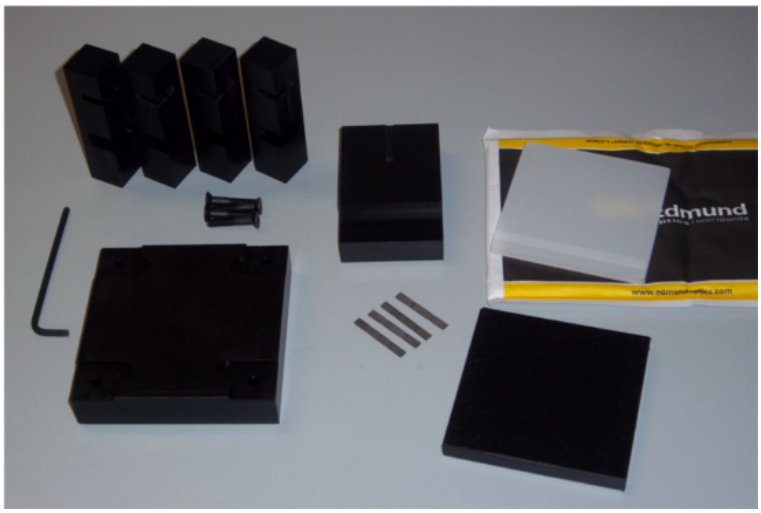

Figure 6.23 - Parts of demonstrator and mounting tools

In Figure 6.23 are present all the pieces ready for assembly. On the left the tools (columns, base and template) and on the right mirror, nylon basement and NiTi supports.

Before definitive bonding, some tests have been performed on two types of adhesives: a two-component epoxy and a cyanoacrylate. On scraps of each of the materials has been glued a strip of metal and the whole was brought to temperature over 60°C, to verify the held. For its best performance, was eventually chosen the cyanoacrylate.

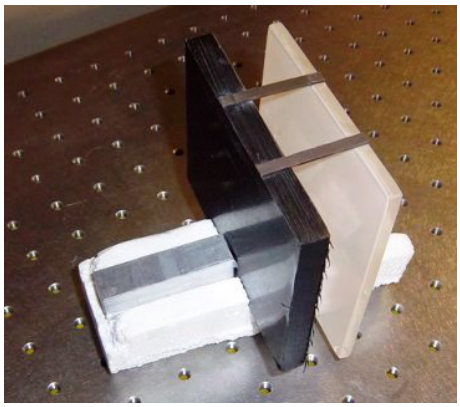

Figure 6.24 - Bonding test

The first step of the assembling is therefore to ensure the two plate among the columns and at their base. Subsequently, the four NiTi supports are bonded one at a time on the sides.

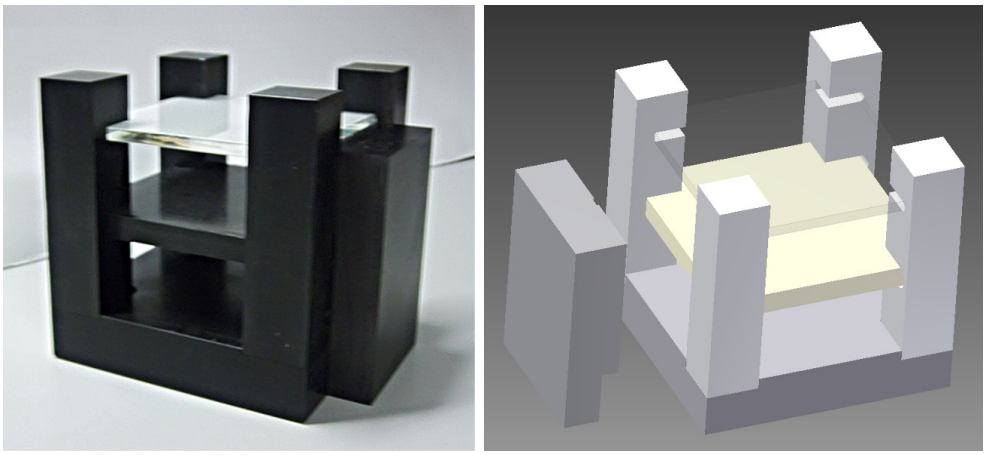

Figure 6.25 - Assembly mounted and ready for bonding

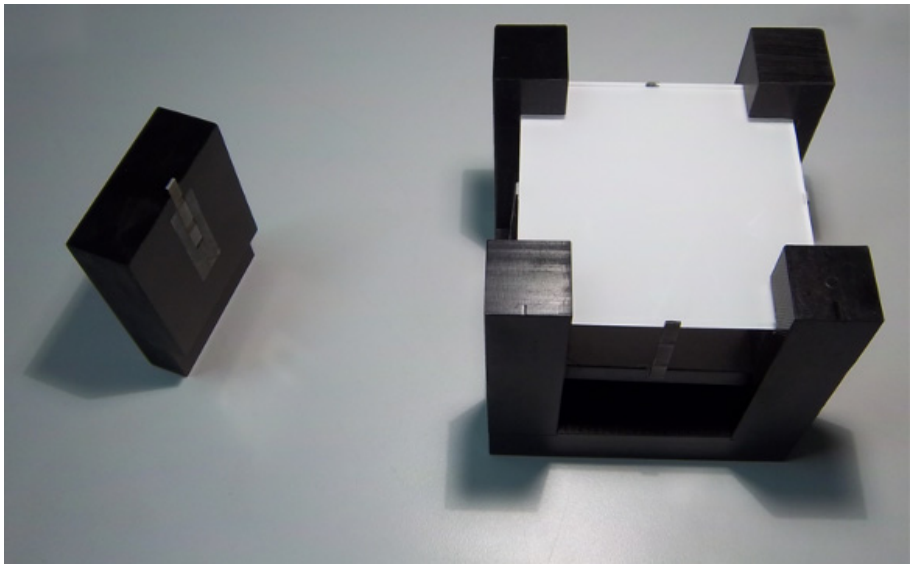

Figure 6.26 - Demonstrator assembled, still in the mounting tool

7 Numerical Modeling and Experimental Validation

7.1 FE Model

To generalize the study on the mounting application designed, has been exploited a Finite Element Model, which reproduce the same structure of the technical demonstrator described in Chapter 6 and moreover some different configurations (for which please refer to the next section 7.1.1) to assess the behavior of the supports.

In order to verify the reliability of the FE model in reproducing the behavior of the NiTi, and consequently also the comparison with the performance of the steel, an experimental validation has been performed. This is exactly the purpose of the technical demonstrator. Indeed, the validation is made by measuring the strain levels generated on the system during an experimental test and then comparing the obtained results with the data obtained from the numerical model under the same loading conditions.

For what described until now, in this chapter will be proposed comparisons between the various FE models, and between the FEM and the experimental testing of the structure of the demonstrator.

7.1.1 Geometry and Mesh

The first step of the FE modeling is the preparation of the geometry of the system. The basic model is the same already described in the discussion on the technical demonstrator (see section 6.2). Reminding it, the elements of the structure are:

- upper plate: the *Optical Glass*
- lower plate: the *Plastic Base*
- four flexures: the *Supports*

From the Figure 1.1, it is possible to get an image the structure of the assembly.

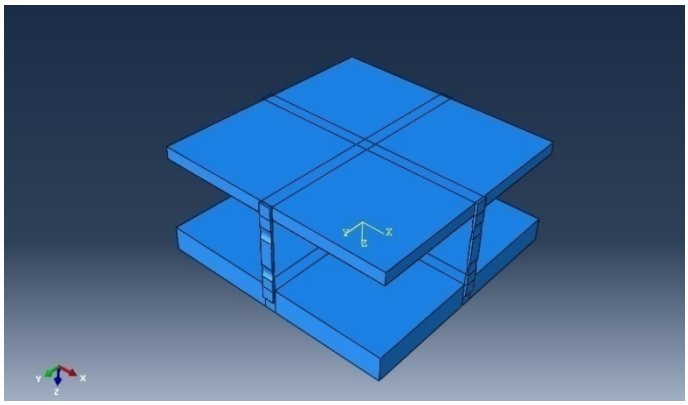

Figure 7.1 - Assembly model geometry

The scheme of the FEM configurations studied, with the main features of all the elements, is summarized in Table 7.1.

		Optical Glass	Plastic Base		Supports	
			NO preload	Preload		
Dimensions [mm]	width and length	100x100	100x100	102x102	40x5	
	thickness	5	10	10	constant 1	
					waisted: max=1, min=0.4	
Material		Fused Silica	Nylon		NiTi	Steel
ρ		2200 Kg/m	1140 Kg/m			7870 Kg/m
E		73 GPa	33 GPa			210GPa
CTE		5.5E-7 K	70E-6 K			11E-6 K

Table 7.1 - Summary of configurations

The optical glass and the base are modeled in a similar way, with 3D stress elements (C3D8), with 8 nodes. The mesh is refined next to the bonding area to better approximate the stress results in this important region of the system. Figure 7.2 shows the appearance of the two meshes.

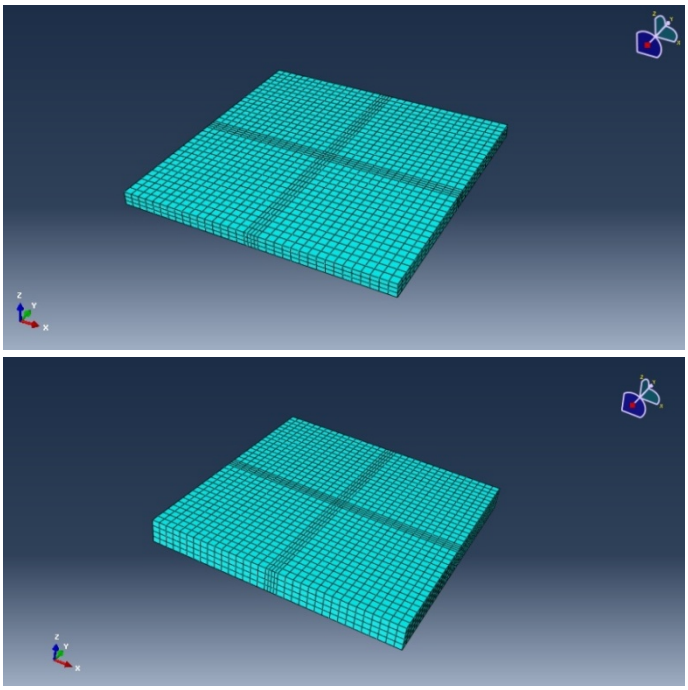

Figure 7.2 - Meshes of Optical glass (top) and Base (bottom)

The supports are modeled with the same element type of the other two parts of the assembly. The geometry configurations are two: the first with a constant rectangular section, the second with two "bottlenecks" (waisted flexure).

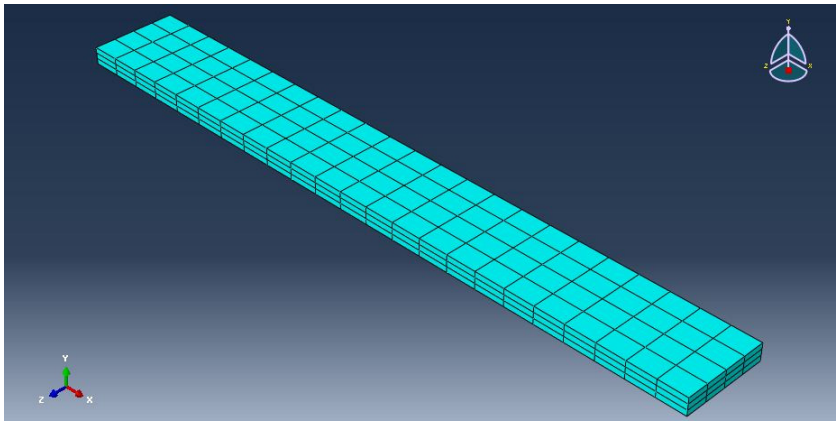

Figure 7.3 - Mesh of the rectangular flexure

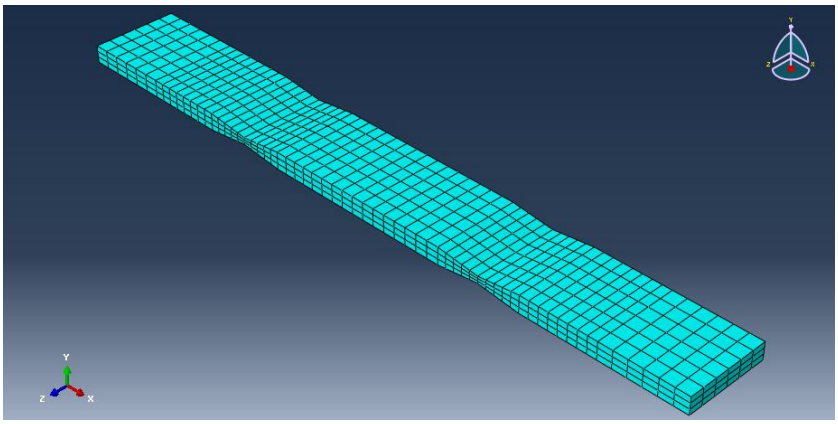

Figure 7.4 - Mesh of the Waisted flexure

7.1.2 Analysis

The geometry of the assembly is the one in figure Figure 7.1.

The bottom surface of the Base is pinned to simulate the constraint resulting from the lying on a plane. The central node of the same surface is encastred, so the thermal expansion works uniformly. The four Supports are located on the middle of Base and Optic sides. They are constrained to the surface with *TIE, to simulate the bonding.

The analysis simulates the action of ground load (gravity) and applies a thermal load of $\Delta T=30°C$. The preload is simulated with a further "bonding step", in which is recreated the displacement of upper part of the blades, to coincide with Optic side.

Different cases were analyzed, they are the same combinations summarized in Table 7.1, and are indicated as:

- **CASE 1** : the support has constant thickness and the Base and Optic has the same dimension (no preload)
    - **CASE 1.a** :Support in Steel
    - **CASE 1.b** :Support in NiTi
- **CASE 2** : the support in configuration of waisted flexure
    - **Support in Steel**
        - **CASE 2.a.N** :Base and Optic has same dimension (**N**o preload)
        - **CASE 2.a.P** :Base and Optic has different dimension (**P**reload)
    - **Support in NiTi**
        - **CASE 2.b.N** :Base and Optic has same dimension (**N**o preload)
        - **CASE 2.b.P** :Base and Optic has different dimension (**P**reload)

Model Results: Steel

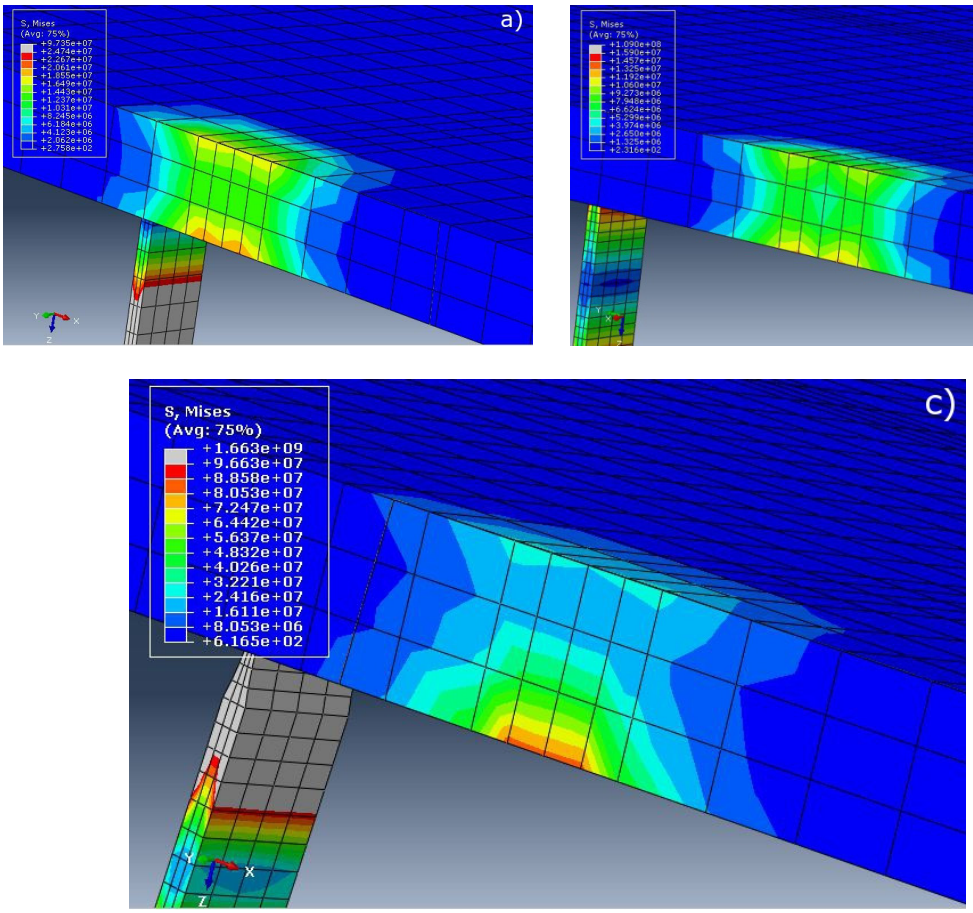

Figure 7.5 - Results for Steel in all configurations:
(a) case1.a, (b) case2.a.N, (c) case2.a.P

The above figures show the distribution of stresses on the optical glass, in the area of flexure bonding .

The first two images *a*) and *b*) refers to the configuration without preload, while figure *c)* to the configuration adopted by the demonstrator tested.

In all cases the stress is focused on the zones of greater geometric singularity: the upper and lower surface. In these configurations, the flexures bend and the stress is not distributed evenly, but it is greater on the lower surface of the optical glass. The maximum value is $\sigma = 7.32\ MPa$ in case *a)*, $\sigma = 4.12\ MPa$ in case b*)* while in the case *c)* is $\sigma = 31.9\ MPa$.

The stress is lower using the waisted flexure in the case without preload because most of stress and strain is loaded in the areas of singularities created by the narrowing. In the third case, despite the presence of the hinges, the load is high, due to high strain. In the rectangular case the maximum stress value on flexure is $\sigma \sim 41 MPa$ and it is

located in the bonding area, while for case *b)* and *c)* the maximum is $\sigma \sim 48MPa$ and $\sigma \sim 797MPa$, both localized in the hinges.

The strains have greater amplitude for the waisted flexure, the maximum values for the case with preload is $\varepsilon = 3789\,\mu$. The values of stress and strain for the case preload are high and then go beyond the range of allowable deformation for steel, making it not suitable, if not for direct comparison with the values in the case of NiTi.

Model Results: NiTi

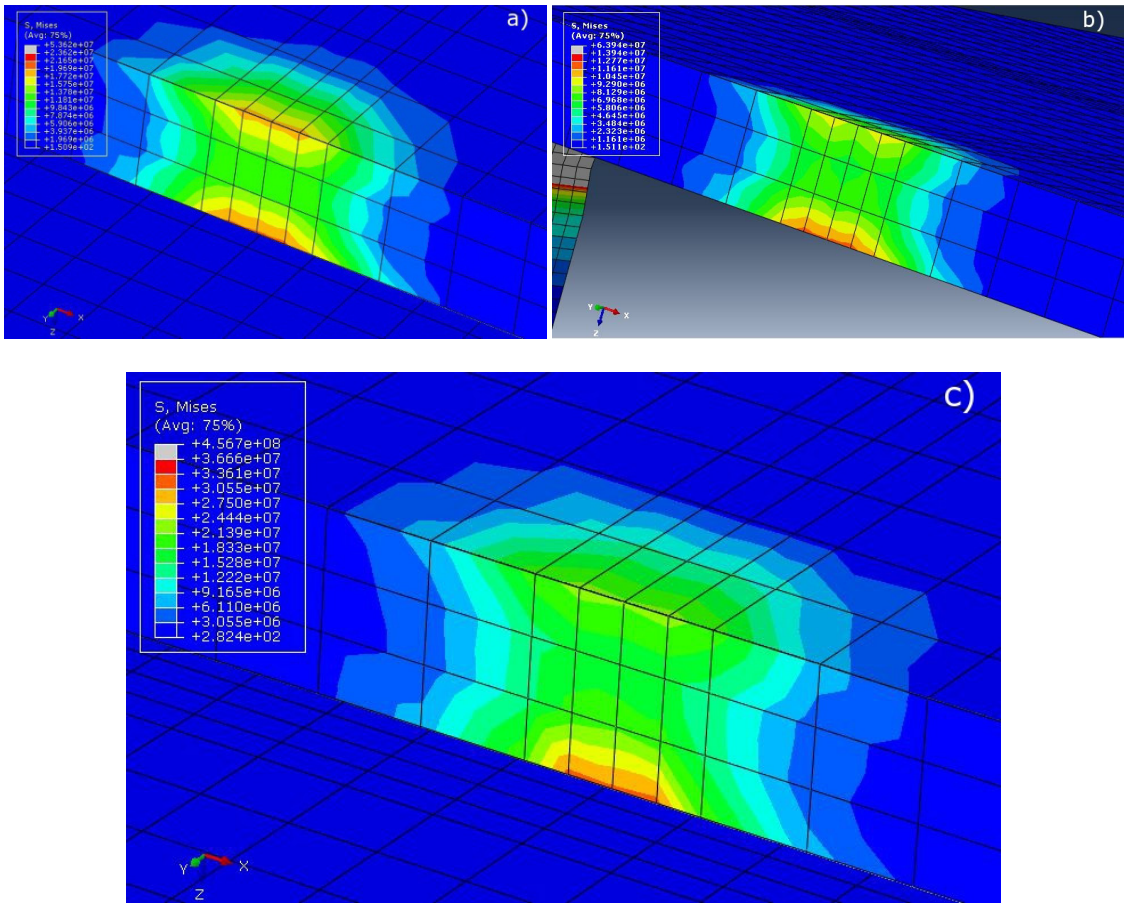

Figure 7.6 - Results for NiTi in all configurations:
(a) case1.b, (b) case2.b.N, (c) case2.b.P

As in the case of Steel the above figures show the stress distribution on optical glass, in the three cases.

In the model analyzed, has been used an equivalent material instead of the real NiTi. Doing so the model converges more easy, with no numerical crash, but it is not possible simulate the transformation start of martensite. The only difference with Steel

model is the Young's modulus. It is useful to describe only elastic behavior of SMA in austenitic phase and to obtain a first estimate of stress and strain.

The distribution of stress is the same of prior case with Steel, and the same observations are corrected. A concentration of stresses is located both at upper and lower surface of optic. The flexure works in bending, so the peak load is on lower surface. The maximum stress on glass is 6.3 *MPa* in case *a)* and in case *b)* 4.*2 Mpa*. The stress computed in Case *c)* is the value of comparison, and for this configuration is 8 *Mpa.* The maximum strain for flexure is $\varepsilon = 4094\ \mu$, in the preload configuration.

The results obtained in the case c) have a peculiarity. The use of a material with lower elastic modulus allows to obtain stresses lower than the steel at the same deformation, but this does not show the peculiarity of the NiTi, which is the induction of martensitic transformation and the recovery of greater deformations. To show this behavior even in the numerical model, it was necessary to make changes, which lead to the following case.

Simplified Model for SMA

The use of Lagoudas subroutine in the assembly caused numerical instability and non-convergence. The valuation of behavior of NiTi has been done with the use of another simplified model of waisted flexure. The model adopted is the same of section 6.5 at page 88, where it was used to find the parameters of NiTi for SMA subroutine. The narrowing is described with a trapezoidal geometry because the original curve geometry was also cause of non convergence when the subroutine were computed.

The model of the flexure, has been constrained on one side in order to simulate the bonding to the base, while on the other side receives as input a displacement, the value of which was derived from the complete model (CASE2.bP). The output that is obtained from this analysis is the reaction force acting on the area of bonding, which is then used to be reported on glass.

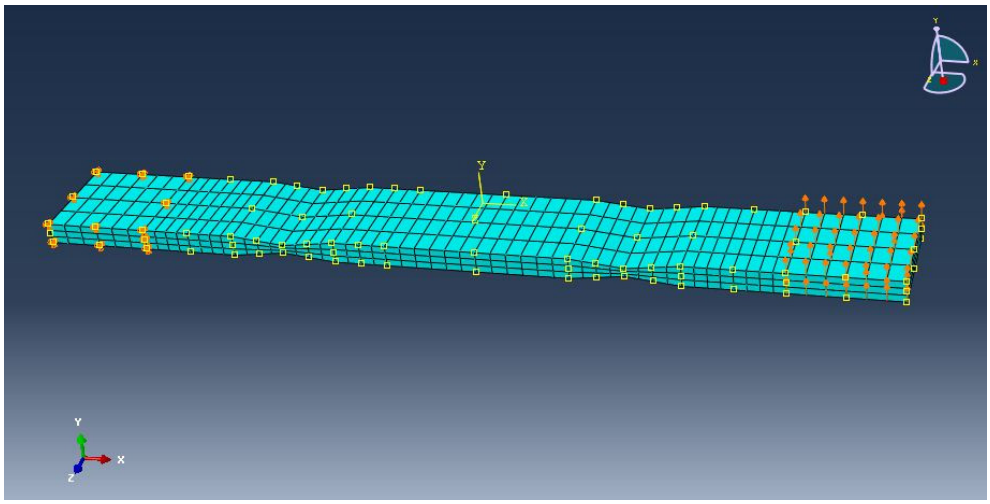

Figure 7.7 - Waisted flexure model

On the second model of the only glass, the force just calculated becomes the input to be applied, to obtain the stresses induced by the bonding with the flexure. The condition of constraint is made in order to recreate the operating conditions of the assembly and is achieved with hinges on the sides that are not loaded.

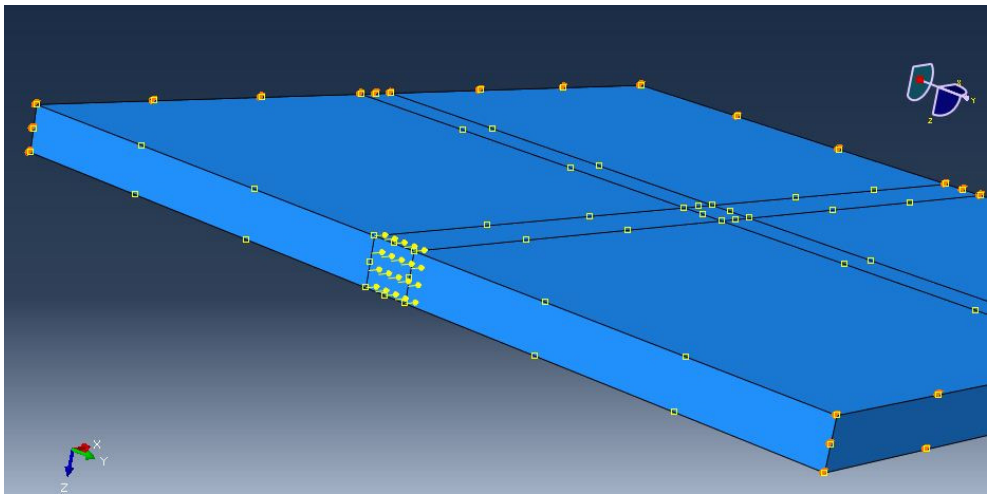

Figure 7.8 - Glass only model

In this manner it was possible to have an estimate of the average value of the stress that acts on optics, $\sigma = 0.32$ MPa. It is significantly less than the value of the case of flexure in steel (CASE 1.a.P).

As seen in previous results, even here the stress distribution on the thickness of the glass is not uniform, but unlike the other cases, the distribution in the thickness is symmetrical instead of concentrated on the lower surface. To better estimate this aspect and obtain a method for evaluating the maximum stress from that of the simplified model, it was decided to study in detail this effect on another model, identical to the last presented, but with the properties of steel. With this model were compared to values of the upper and lower faces of the glass.

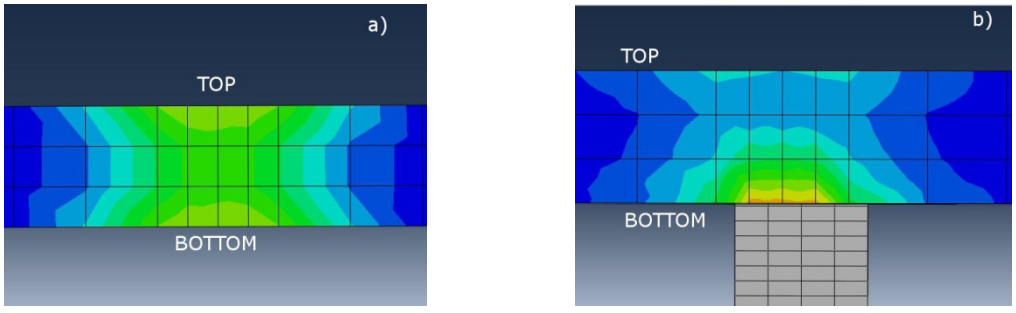

Figure 7.9 - Stress distribution: (a) simplified model with steel, (b) CASE 1.a.P

The value of maximum stress obtained in the case of the simplified model with steel, $\sigma = 14.19\ MPa$ is almost identical to the value of stress on the upper surface of the glass in the case of the assembly, $\sigma_{up} = 14.4\ MPa$. The value on the lower surface is the maximum and is equal to $\sigma_{bottom} = 31.9\ MPa$

By making the ratio between the values of stress on the two faces of the complete model with steel, is obtained a correction factor which can be used for the estimation of the maximum load which undergoes the glass in the case of use of flexure of NiTi.

$$k = \frac{\sigma^{Bottom}}{\sigma^{Top}}\Big|_{STEEL} = \frac{31.9}{14.4} = 2.22 \cong 2.5$$

It can be obtained so that the value of maximum stress for the NiTi is of the order $\sigma = 0.32 * k = 0.72\ MPa$, value which however is much lower than the maximum obtained with the steel.

7.1.3 Conclusion

The assembly model used, has a very simple geometry and it is a first step to understand the using of SMAs. However the stresses calculated on mirror validate the use of this alloys for optomechanical mounting. Figure 7.10 shows a comparison between Steel and NiTi behavior.

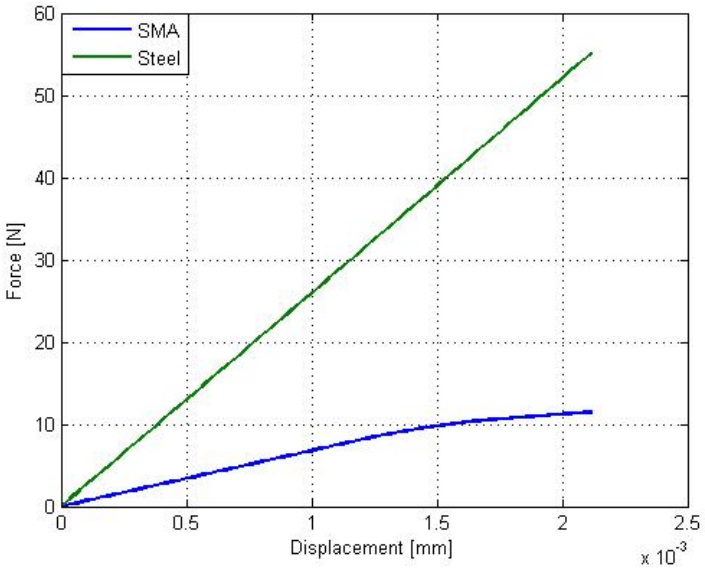

Figure 7.10 - Comparison between Steel and NiTi results

In Figure 7.10 are plotted the force results obtained both for steel and NiTi flexures by the numerical model. The curves range from relax position as initial condition to maximum displacement reached. The steel is approximated as only elastic material, but

this has been made only for comparison because, at this level of force and strain, it can be supposed that the steel yield stress is exceeded.

The strength reached by NiTi is always less than that of steel, for two reasons. One is the commonplace effect that the NiTi alloy has a minor magnitude of Young's modulus. The second reason is the most important: the induction of martensitic transformation allows to keep the stress level on constant and low values, even if reaching higher deformations. The properties of SMAs assure that this large strain can be recovered and the position of mounting is maintained.

7.2 Validation Tests

7.2.1 Experimental Setup

The demonstrator has been realized in order to validate the numerical results obtained in the FEM, in particular in the model with the waisted strips. To proceed and obtain strain and stress values, the work was concluded with the application of strain gauges to the demonstrator and a test of thermal expansion.

The application of strain gauges was decided at three points in the demonstrator: in the middle of the mirror, on the side near the bonding with a NiTi support and on the support itself. Those on the mirror are both bi-directional gauges, non-overlapping, but adjacent. Both in the middle and on the side, was given priority to the longitudinal ones, placing them along the center line of the square mirror. The one on the NiTi support was rather unidirectional, only longitudinal, directed in the length of the strip and, for practical reasons, it was stuck in the central part, where the thickness is 1 mm.

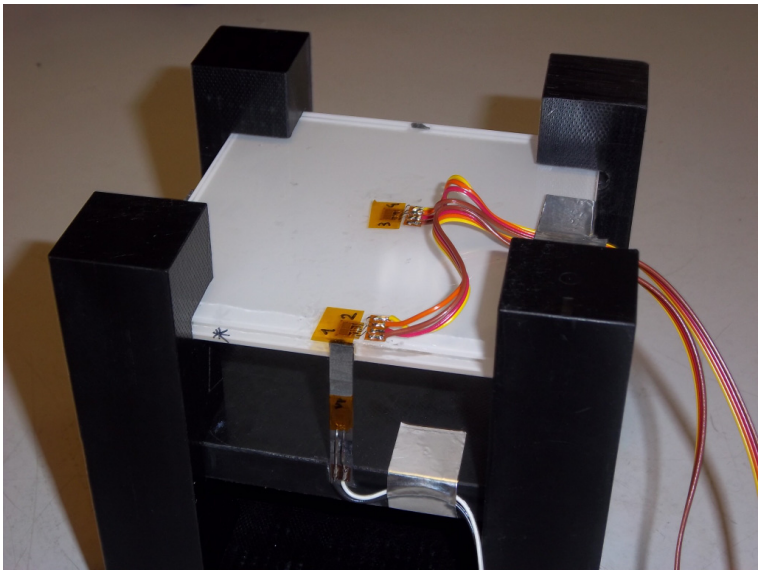

Figure 7.11 - Demonstrator with strain gauges applied on it

The test of thermal expansion is developed by inserting the demonstrator in the oven at room temperature and increasing the temperature of 30 degrees (i.e. approximately from 20°C to 50°C). To keep monitored the temperature were applied three thermocouples, one for each material: near the center of the glass, on a sheet of NiTi and on the basis of nylon.

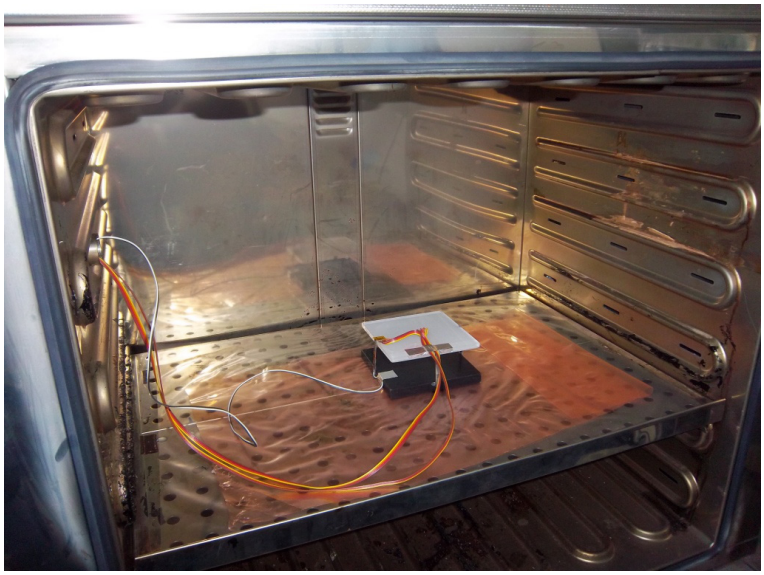

Figure 7.12 - Demonstrator in the oven

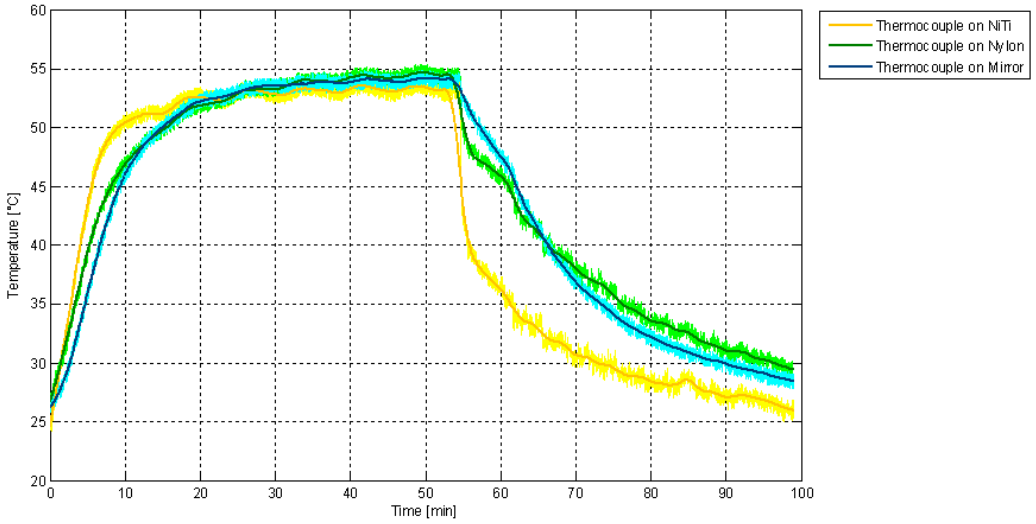

Figure 7.13 - Signals of thermocouples

7.2.2 Data Conditioning

Once acquired, the data from the strain gauges are not directly usable. Indeed the strain gauges applied are of the type compensated for steel and then it is necessary first of all removing the offset. To do so the manual on the effects of temperature, provided by the Micro-Measurements company, has been consulted.

When making strain measurements at a temperature different from the instrument balance temperature, the indicated strain is equal to the sum of the stress-induced strain in the test object and the thermal output of the gage. With the thermal output expressed in strain units, correction for this effect is made by simply subtracting (algebraically, with sign) the thermal output from the indicated strain.

Then, assuming that the strain indicator was balanced for zero strain at room temperature (specifically 24° C), compensation is made subtracting the thermal output calculated with the formula from the strain measurements at the test temperature. This procedure can be expressed analytically as follows:

$$\varepsilon' = \varepsilon'' - \varepsilon_{T/O}$$

where:

ε''= uncorrected strain measurement, as registered by the strain indicator.
ε'= strain indication corrected for thermal output.
$\varepsilon_{T/O}$= thermal output, in strain units, from the formula.
Approximate correction for thermal output can be accomplished most directly and easily using the formula on the gage package data label: a regression-fitted (least-squares) polynomial equation representing the thermal output curve. The polynomial is of the following form:

$$\varepsilon_{T/O} = A_0 + A_1 T + A_2 T^2 + A_3 T^3 + A_4 T^4$$

where: T = temperature; A_0=−1.23e+2; A_1=6.96; A_2=−8.51e-2; A_3=+2.51e-4; A_4=0.

It would be possible to obtain a compensation also for the application of the strain gage on a different material, but this is not necessary because from FEM are obtained strains due to the combined action of mechanical and thermal load.

Actually not even the correction related to the steel is necessary, because a couple of strain gauges has been placed on purpose at the center of the mirror, where the mechanical induced stress should be negligible. In this way, considering the difference between the signal acquired from the strain gauges placed on the side and at the center of the mirror, it is possible to obtain the mechanical deformation avoiding the systematical errors and the contribution to the signal due to thermal strain of the glass.

$$\Delta\varepsilon' = (\varepsilon''_{Side} - \varepsilon_{T/O}) - (\varepsilon''_{Middle} - \varepsilon_{T/O})$$

7.2.3 Results

The measurements obtained by the strain gauges on the glass, are presented in the figures Figure 7.14 and Figure 7.15 and in figures Figure 7.16 and Figure 7.17 the difference between middle and side signal is analyzed.

Middle and Side strain gage : Longitudinal signal

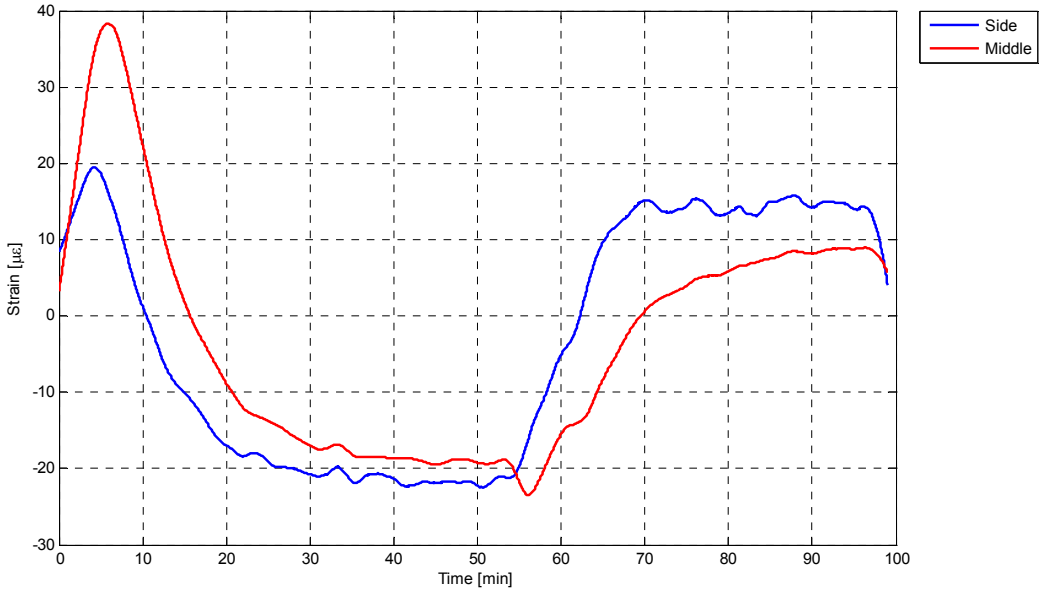

Figure 7.14 - Longitudinal measurement

Middle and Side strain gage : Longitudinal signal Difference

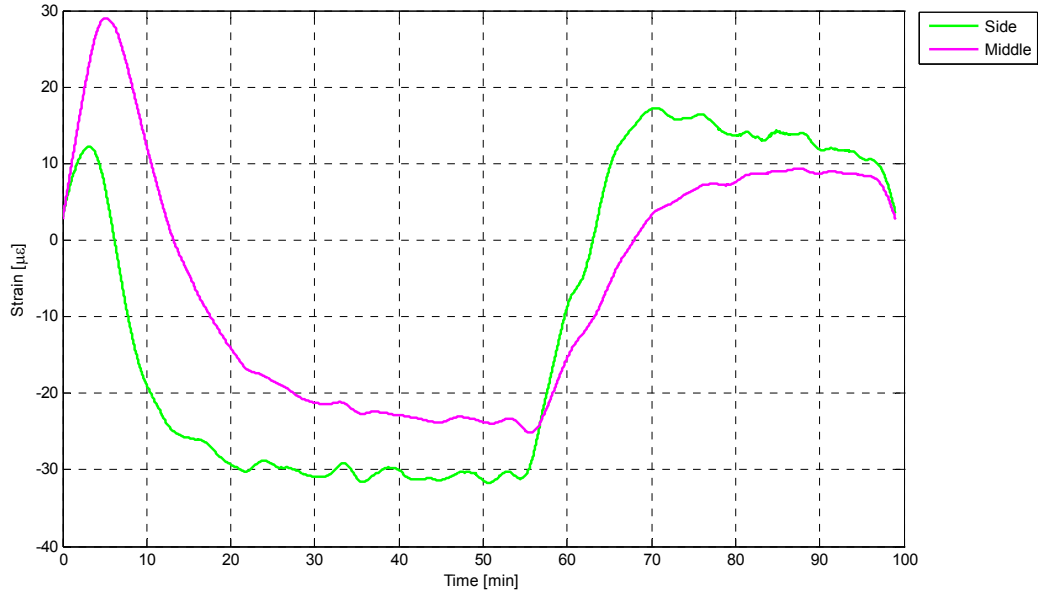

Figure 7.15 - Transverse measurement

Middle and Side strain gage : Longitudinal signal

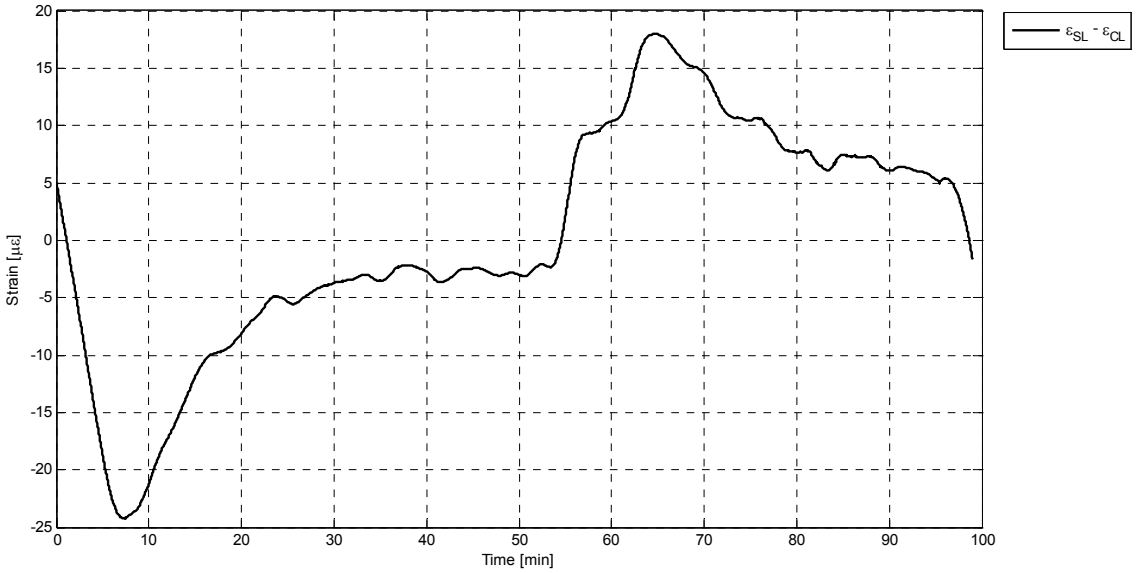

Figure 7.16 - Longitudinal difference signal

Middle and Side strain gage : Transverse signal Difference

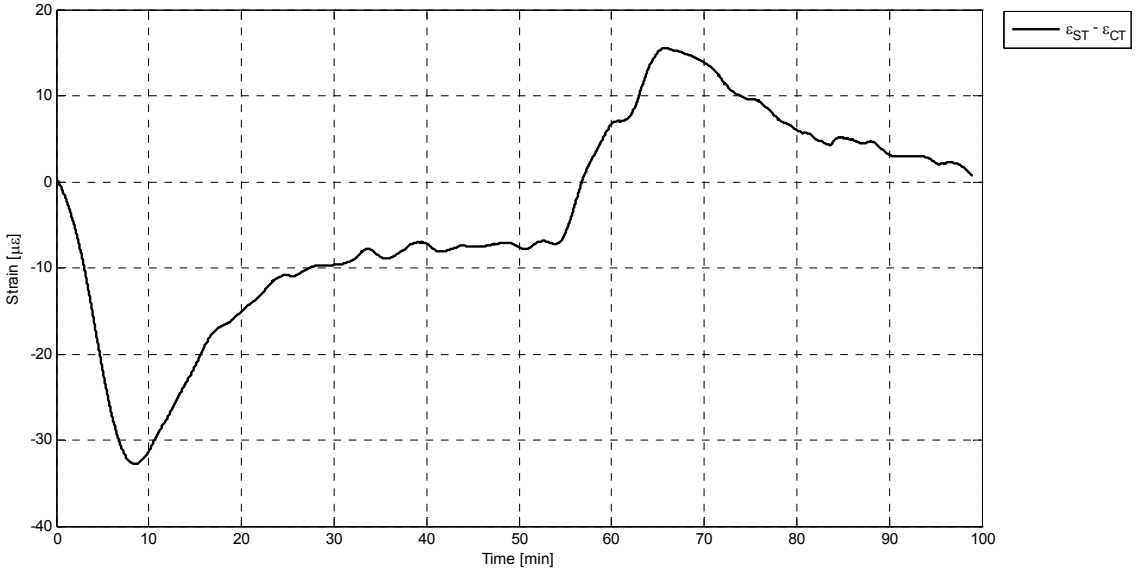

Figure 7.17 - Transverse difference signal

Numerical data can be extrapolated and compared to the measurements. The nodes observed are one in the center of mirror and two near the bolding. Their identification number is ID 1848 for center node and ID 1776 and ID 1773 for the side nodes. The node ID 1776 is the nearest to bonding. In following figure they are indicated with a red point.

Longitudinal Strain

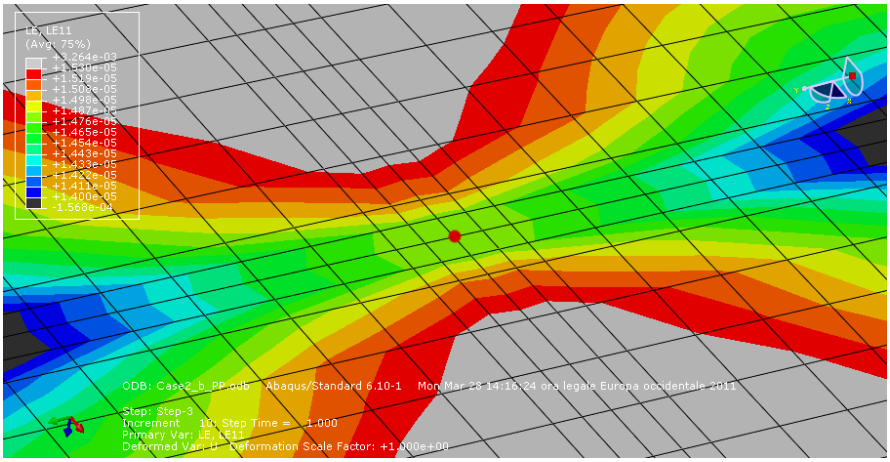

Figure 7.18 - Middle Node, Longitudinal Strain (ID 1848)

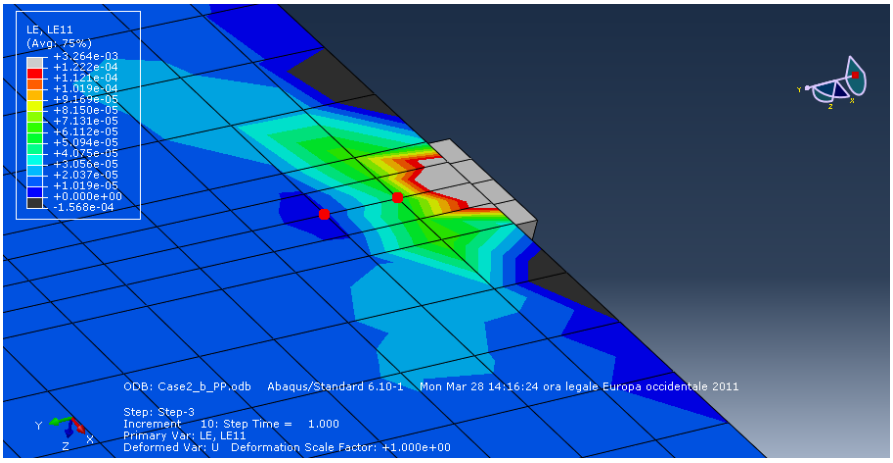

Figure 7.19 - Side Nodes, Longitudinal Strain (IDs 1776 & 1773)

NODE ID	value [με]
1848	14.83
1776	50.48
1773	7.14

Transverse Strain

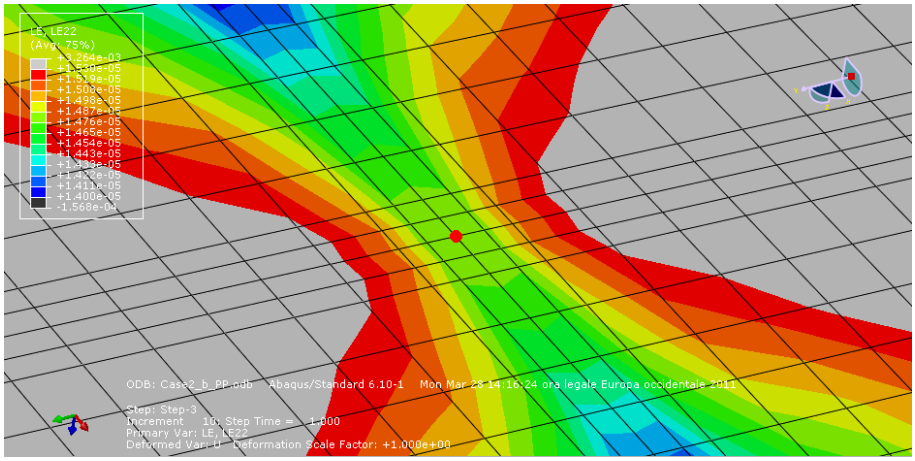

Figure 7.20 - Middle Node, Transverse Strain (ID 1848)

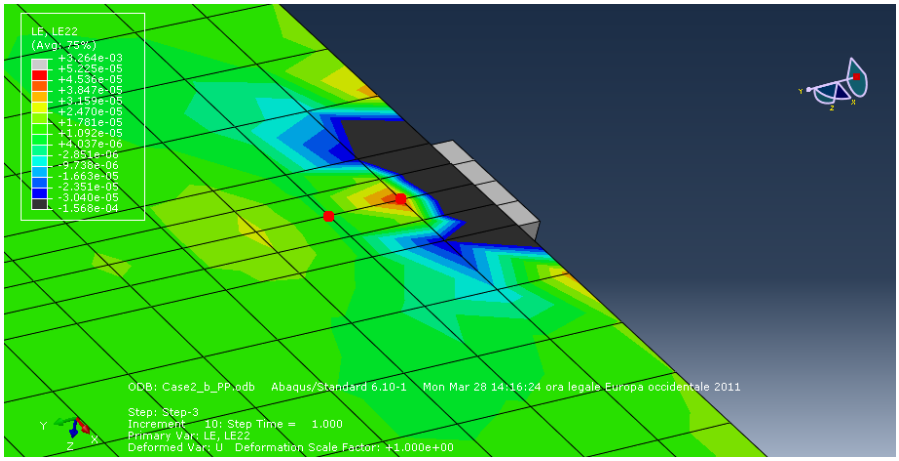

Figure 7.21 - Side Nodes, Transverse Strain (IDs 1776 & 1773)

NODE ID	value [με]
1848	14.83
1776	46.89
1773	9.3

7.2.4 Discussion

The nodes chosen to analyze are located, as much as possible, in the position of physical strain gage application, to compare experimental and numerical data. The critical measurements for optomechanic are the strains and the stresses on optical components, caused by the presence of the supports. The data reported have been treated as described in the previous section.

The values obtained by numerical simulation are resumed in the Table 7.2 and Table 7.3, and are compared with the experimental data presented at the beginning of this section.

Longitudinal Data	
Numerical Difference	[Δμε]
ID1848−ID1776	35.65
ID1848−ID1773	7.69
Experimental Difference	~3

Table 7.2 - Longitudinal strain values: mechanical

Transverse Data	
Numerical Data	[Δμε]
ID1848−ID1776	32.06
ID1848−ID1773	5.53
Experimental difference	~7.9

Table 7.3 - Transverse strain values: mechanical

The numerical data collected show that the delta values of strain strongly depend on the node considered for the analysis: as a consequence experimental may match with the values predicted with inconstant precision, because of the technical difficulties in placing the sensors exactly at a specific node of the sample. E.g. it can be noticed that the experimental data are more similar to the ones obtained for ID 1773, placed at a greater distance than ID 1776 from the bonding. This result is coherent with the experimental setting, i.e. the positioning of the strain gage near the junction (~2 mm from the side) and the dimensions of the sensor itself (~5 mm). The sensitivity of the measurement is affected by the same mounting problems and, in addition, by assembly inaccuracies and the proper characteristics of materials employed, often deviating from datasheet. Despite all these remarks, comparing numerical and experimental results, the delta strain values are in the same order of magnitude, confirming the capability of this FEM to evaluate the behavior of NiTi supports in optomechanical applications.

8 Conclusions and Future Developments

In this thesis for the first time was studied the employment of Shape Memory Alloys in an optical mounting system, following two different development plans: g*round-based* and *space-based*. The main interest was to evaluate the effects on the considered system of the peculiar properties of this class of metals, both in terms of elasticity and of vibrations damping. Due to the novelty of the idea to apply SMAs to the realization of optical mounting systems, this work aims to be a startup for further improvements both for materials optimizations and development of new mounting solutions.

In order to give a preliminary result on the effectiveness of this choice of materials and approach to the optical mounting systems, a small scale device has been produced and characterized.

In order to have a first actual feedback of the path of project, selection and processing of the NiTi supports and to verify the performance of the system, a first demonstrator on a small scale has been realized.

The structure of the demonstrator consisted of mount a quite rudimentary: a rectangular glass attached to a base and supported by four NiTi sheets, glued to the center of each side. The choice to implement it on a small scale was imposed by the need to test it with the tools available. Actually, the real applicative challenge is the installation on large structures and therefore the configuration is designed to simulate the criticality of the same on a large scale.

The reference material for the application in question is steel, then the performance was verified by reference to it, both in terms of stress / deformations that in terms of damping, particularly at low frequencies.

As an aspect preparatory and complementary to the demonstrator, it has been developed a campaign for the characterization of NiTi systems and their numerical validation. It 's been verified how it is possible to reproduce the behavior of SMAs with a certain accuracy, through specific numerical models. It was also emphasized, however, that this representation is related to the experimental characterization of these materials and can not ignore the knowledge and practical experience in approaching these metallic systems.

Indeed resulted that not always a physical datum obtained for a specific material NiTi, makes possible a numerical modeling consistent with the behavior of the material itself. Sometimes, in order to obtain a better adaptation of the numerical with the experimental, it has been necessary use parameters "equivalent". So, it is possible to design a NiTi alloy starting from specific requirements of an application, but it is still necessary that the experimental and numerical study are accompanied.

The point of arrival has been so a check, via numerical modeling and its experimental validation, that the supports NiTi can reach deformations beyond the capabilities of the steel, with the advantage that the stresses imposed on glass due to the assembly are

lower. This thanks to the fact take advantage of the superelasticity of the SMAs, i.e. the capacity through the phase transformation to maintain a constant loads with increasing deformation.

On the basis of these findings there are several imaginable future developments, going in the direction of conceiving and designing opto-mechanical assemblies that exploit more thoroughly the special properties of shape memory alloys.

With regard to the segment Ground-based, it is certainly possible to move to a design of assembly more sophisticated of that one made for this thesis, but at the same time simple and reliable. One possible solution that has been conceived, which is applicable to circular optics, is that of a gripper, with wrap-around supports that clamp the optical without the need for bonding, while providing a uniform pre-load given by the effect of shape memory.

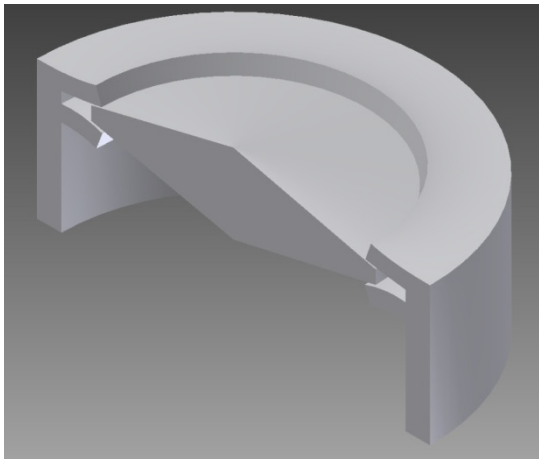

For the Space-based application has been examined the ability of SMAs to absorb vibrations, particularly in the martensitic phase and rhombohedral, and to modulate the microstructure of the material to achieve better damping performance compared to traditional metals. To expand this study might be envisaged to start a more broad and detailed campaign to characterize the response in terms of measuring the coefficient of internal friction and vibration, with the design of alloys that meet the temperature conditions necessary for application in space and with associated validation tests with tests on a shaker.

Bibliography

[1] C.M. Wayman, T.W. Duerig - *An Introduction to Martensite and Shape Memory* In: T. Duerig, K. Melton, D. Stokel, C. Wayman - Engineering Aspects of Shape Memory, Alloys Butterworth-Heinemann ed., UK, 1990, pp. 3-20.

[2] K. Otsuka, T. Kakeshita - *Science and Technology of Shape-Memory Alloys: New Developments,* MRS Bulletin, February 2002.

[3] S. Miyazaki, K. Otsuka - *Development of Shape Memory Alloys*, ISU International, Vol. 29, 1989

[4] J. Uchil - *Shape memory alloys – characterization techniques*, Pramana - journal of physics, Vol. 58, May & June 2002

[5] V.A. Chernenko, B. Rajini Kanth, P.K. Mukhopadhyay, S.N. Kaul, E. Villa, A. Gambardella, S. Besseghini - *Stress-induced and thermoelastic properties of Ni–Fe–Al melt-spun ribbon,* Applied Physics Letters, October 2008

[6] H.C. Lin, S.K. Wu, M.T. Yeh - *Damping Characteristics of TiNi SMAs,* Metallurgical Transactions, Vol. 24, October 1993

[7] W.W. Kin - *Dynamic Characteristics of Shape Memory Alloys (SMA),* Dissertation for Bachelor of Engineering (HONS) in Materials Engineering, March 2005

[8] D.C. Lagoudas - *Shape Memory Alloys,* Springer ed., USA, 2008

[9] A. Ahmad - Handbook of Optomechanical Engineering CRC Press ed., USA, 1997

[10] P.R. Yoder Jr. - *Mounting Optics in Optical Instruments,* SPIE Press Monograph Vol. PM181, 2011

[11] R. Foy and F.C. Foy - *Optics in Astrophysics,* ed. Springer, 2005

[12] Mel Schwartz - *Encyclopedia of smart materials: vol I and II*, Wiley-Interscience Publication, 2002

[13] Chopra - *Review of state of art of smart structures and integrated systems*, AIAA Journal, 40(11):2145–2187, 2002

[14] A. Bekker and L.C. Brinson - *Phase diagram based description of the hysteresis behavior of shape memory alloys,* Acta metallurgica, 46:3649–3665, 1998

[15] D. Lagoudas and Z. Bo - *Thermomechanical modeling of polycrystalline smas under cyclic loading*, International Journal of Engineering Science, 14(1-4):1089–1204, 1999

[16] S. Zhu and Y. Zhang - *A thermomechanical constitutive model for superelastic sma wire with strain-rate dependence*, Smart Materials and Structures, 16:1696–1707, 2007

[17] H. Prahlad and I. Chopra - *Development of a strain-rate dependent model for uniaxial loading of SMA wires*, Journal of Intelligent Material Systems and Structures, 14:429–442, 2003.

[18] C. Preti - *Microattuatori in leghe a memoria di forma: sperimentazione, implementazione di leggi leggi costitutive e validazione numerico-sperimentale*, Tesi di laurea, Politecnico di Milano - Dipartimento di Ingegneria Aerospaziale, 2006.

[19] M. Riva - *Smart structures in instrumentation for astronomy*, Tesi di dottorato, Politecnico di Milano - Dipartimento di Ingegneria Aerospaziale.